Enabling Electroceuticals

Gregory E. Moore

A dissertation
submitted in partial fulfillment of the
requirements for the degree of

Doctor of Philosophy

University of Washington

2023

Reading Committee:

Joshua R. Smith, Chair

Matt Reynolds

Chet Moritz

Program Authorized to Offer Degree:
Electrical and Computer Engineering

University of Washington

Abstract

Enabling Electroceuticals

Gregory E. Moore

Chair of the Supervisory Committee:
Joshua R. Smith
Department of Electrical and Computer Engineering
Department of Computer Science and Engineering

Disorders affecting the health of millions have traditionally been treated using combinations of invasive surgery and then pharmacological interventions. While successful to a degree, surgery is both expensive and risky due to infection and malpractice. Additionally, developing new drugs for improving treatment is becoming increasingly difficult (less than 1 in 100 new drugs are approved/effective), and costs are spiraling toward $1-10 billion per new drug. Bioelectronic interventions (so called electroceuticals) are already demonstrating significant impact in addressing impediments resulting from non-normative operation of the health of individuals. Treatments available currently via pharmaceuticals are necessarily systemic, flooding the patient's system in hopes of affecting the area exhibiting difficulty. However, if a more granular discovery of affected tissues and equally focused application of treatment were possible, then therapies could be hyper-targeted towards treating the condition, let alone avoiding unwelcome side-effects from the pharmaceutical inundation. Electroceuticals, on the other hand, help monitor biological systems, providing real-time information for clinicians to diagnose obstacles that impede patients. Where appropriate the implanted medical device can then precisely modulate the biological systems via electrical, chemical, sonic, or heat effectors in order to enable the patient's best life.

The field has made rapid progress towards authentically achieving these goals in recent

years. For all electroceuticals, three guidelines must confine general implant development: minimal invasiveness, safe continual operation, and sufficiency at the task of treating the condition. As the treatment efficacy and treated condition breadth has expanded though, the opposing pillars have begun to show strain.

The next generation of electroceuticals will require a holistic approach to systems design that incorporates efficient, minimally invasive, wireless implants, and a singular focus on providing enabling, long-term functionality. The confluence of recent wireless technology developments and biomedical treatment needs has presented a unique opportunity to improve the lives of countless living beings. By untethering sensors and effectors from sources and improving signal fidelity, system efficiency, and cost accessibility. I believe that the modern conjunction of wireless power delivery, ultra-low power communication, and sub-mm component design will address the needs of bringing electroceutical based therapy to the masses. As such, this dissertation presents the culmination of efforts to produce a battery-free, wirelessly powered, wireless transceiver electroceutical for use in biomedical research and clinical settings.

TABLE OF CONTENTS

Page

List of Figures iii

List of Tables ix

Chapter 1: Introduction 1
1.1 Implantable, Injectable, and Ingestible Electroceuticals 1
1.2 Enabling Electroceuticals via Wireless Power Transfer and Low-power Backscatter Communication 4
1.3 Contributions and Thesis Organization 8

Chapter 2: Classifying WLAN Packets from the RF Envelope: Towards More Efficient Wireless Network Performance 11
2.1 Introduction 11
2.2 Related Work 13
2.3 WLAN Primer 14
2.4 WLAN Dataset Development 16
2.5 Neural Network Architecture 19
2.6 Results 21
2.7 Applications 23
2.8 Conclusion and Discussion 24

Chapter 3: Wireless power and communication for implanted electronics 26
3.1 Introduction 26
3.2 Neural Prosthetic Technologies 31

Chapter 4: A Low-Cost, Open-Sourced Platform for High-Fidelity Characterization of Large WPT Coils 46
4.1 Introduction 46

4.2 Materials and Methods 48
4.3 Results 51
4.4 Discussion 56

Chapter 5: Analysis and Design of an Asymmetric Resonant Wireless Power Transfer System: Optimal Intermediate Coil Size and Location 57
5.1 System Analysis 59
5.2 System Setup 66
5.3 Experimental and Quantitative Simulation Results 68
5.4 Conclusion 71

Chapter 6: Commercial Off-the-shelf Wireless Injectable Electroceuticals for Translational Research 73
6.1 Commercial off the Shelf Injectable Electroceutical Introduction 73
6.2 COTS Injectable Electroceutical Example - Application Specific - The Smart Breast Clip Overview 74
6.3 COTS Injectable Electroceutical Example - General Platform - ElectRX Overview 82
6.4 Smart Breast Clip v02 - Sense Board 83
6.5 Smart Breast Clip v03 - Power Board 90
6.6 Smart Breast Clip v10 - Mouse Board 113
6.7 Commercial off the Shelf Injectable Electroceutical Platform - ElectRX . . . 117
6.8 Conclusion 120

Chapter 7: Conclusion 129

Bibliography 131

LIST OF FIGURES

Figure Number Page

1.1 (a) Sensionics Eversense glucose 90-day monitor (b) 3 Bion microstimulator variants that have been tested in clinical studies 4

1.2 (a) Tissue penetration of an EM field for various tissues demonstrating an exponential decrease due to frequency [1] (b) SAR and E_i regulatory curves demonstrating how frequency selection must be made to satisfy both. [2] . . 6

1.3 (a) Cochlear implant and spinal cord stimulator examples of applied NF-MRC system [3] (b) Equivalent circuit model for a generic NF-MRC system [4] . . 7

1.4 (a) A receiver based Load Shift Keying circuit model [5] (b) Using Load Shift Keying with a variation on Manchester Encoding, the TX impedance is modulated [6] 8

2.1 Wi-Fi Module Receive Packet Discrimination Power Comparison. Commercially available Wi-Fi Modules consume significantly more power than low-power microprocessors such as the Ambiq Apollo3 Blue. 11

2.2 WLAN Packet Structure. The high-level packet structure for IEEE 802.11b/g/n protocols. 14

2.3 Generating an RF WLAN Dataset: (a) Our data collection setup. We use two Ettus SDRs, an envelope detector, and PC. Data is collected in two formats: (1) complex baseband and (2) baseband envelope. (b) We implement the envelope detector circuit operating at 2.4GHz using passive hardware components. 15

2.4 WLAN Data Preprocessing. An example of WLAN data packet before and after generating the envelope signal. 18

2.5 Two Layer CNN: The CNN contains two pruned convolution + max pooling layers that are used for packet classification. 20

2.6 UMAP Representation of WLAN Enveloped Signals: A structurally similar representation of the high dimensional mapped to 2D demonstrating the difficult separability between classifications [7]. 21

2.7 Confusion Matrix: The overall error rate for the 2-Layer Sparse CNN was 11.9%. False-negatives (columns), cluster with the false-positives (rows) around the Beacon, QoS Data, and Data packet types. 21

3.1 Overview of Neural Recording Applications 27
3.2 Generalized architecture for brain-computer interfaces 28
3.3 Overview of backscatter communication. 31
3.4 Comparison of state-of-the-art wireless neural recorders 39
3.5 (a) WPT System Block Diagram showing Wibotic WRELv2 Transmitter, which provides both power at 13.56MHz and bi-directional telemetry at 2.4GHz, and the AIMWPT-RX, which adaptively matches the input impedance and conditions the input power to produce a low noise 3.3V power supply for the dependent noise sensitive devices. (b) At high charging rates, the inclusion of powerpath management decreases the conductive interference on the power plane by 35.4%. 41
3.6 Field Characterization within NHP Cage 42
3.7 (a) A 35hr run of the system demonstrating the possibility of perpetual charging and low noise operation via time-multiplexing between the charging and recording periods. (b) Zooming in on the first 4hrs of operation to demonstrate the ping-pong charging provided by the powerpath manager. The charging states 1-4 (represented by the height of the magenta trace) correspond Precharge, Constant Current, Constant Voltage, and Standby states, respectively. States 0 and 5 correspond to error conditions, which weren't met during this run. 43
4.1 MPFCS with attached B-Field end effector characterizing complex relay resonator. 47
4.2 (a) Tilt/Pan Head with Mounted LED Laser Calibration Mount. (b) Universal Coil Mount with a coil mounted consisting of a 50mm spiral offset by 15mm from a 38.5mm loop. (c) B-field Characterization Mount with Beehive 100B mounted 48
4.3 Software Operation 51
4.4 The concentric calibration circles in the XZ, YZ, and XY planes demonstrating the precision in the reaching the 36 programmed points and the return to origin location 52
4.5 The S_{21} characterization of a volume where a biased repeater RX coil (inset top-right, but inverted from its sweep orientation) is swept at 2.5mm steps through the field resulting from a twin biased repeater TX coil. 53
4.6 The S_{21} characterization of a volume where a biased repeater RX coil (inset bottom-right, but inverted from its sweep orientation) is swept at 2mm steps through the complex field resulting from a 2-D planar WPT array 54

4.7 (a) Measured B-Field by the Beehive 100B from a 38.5mm Non-resonant Loop (b) The simulated B-Field from a digital twin of the 38.5mm Non-resonant Loop. 56

5.1 An Aerial view of the axially aligned five-coil system. In the examined symmetric system, the outer diameter (OD) of TX and RX are identical. In the examined asymmetric system, the OD of the TX is 3x the OD of the RX. The location of the IC, as well as the OD of the IC, are swept to determine the optimal location and size for maximum transferred power. 58

5.2 (a) shows the geometry of a loop coil that has a OD of OD_{loop}. (b) is the geometry of a multi-turn single layer spiral coil that has N turns, separation of p between each turn, and the radius of each turn $r_{i^{th}}$. w is the wire diameter for both coils. 59

5.3 The equivalent circuit model of the conventional MRC WPT system with an included IC. 63

5.4 The tested ICs range from OD = 30mm to 200mm, in 10mm increments. . 66

5.5 A rotated view of the experimental setup showing (from foreground to background) a given instance of the TX, IC, and RX variations. 67

5.6 In the symmetric system (TXC OD = RXC OD = 50mm), a S_{21} heatmap resulting from sweeping ICs of different sizes(OD = 30mm to 200mm) through the separation between the TX and RX. 69

5.7 In the asymmetric system (TXC OD = 90mm, RXC OD = 30mm), a S_{21} heatmap resulting from sweeping ICs of different sizes (OD = 30 mm to 200mm) through the separation between the TX and RX. 70

5.8 In the asymmetric system (TXC OD = 90mm, RXC OD = 30mm), Equal-coupling location (Simulation) (mm) vs. Maximum S_{21} Location (Simulation) (mm) vs. Maximum S_{21} Location (Measurement) have been compared through the separation between the TX and RX. 72

6.1 (a)(top)Standard breast radiological markers [8] (b) Early conceptualization of the Smart Breast Clip [9] 75

6.2 (a)Targeted chromophores with tuneable laser bandwidth overlaid in grey (b) Prior work towards a Tuneable microchip laser [10] 77

6.3 An 3D sketch of the proposed unencapsulated SBC with a helical coil along the long-axis within the confines of a 12G needle approximation (grey cylinder) showing the placement of the 680 and 850nm VCSELs as well as near and far GaAs PIN Photodiodes 79

6.4 A block diagram representation of the TX and RX subsystems of the SBC. . 82

6.5 (a) A block diagram demonstrating the form-factor sensor specific operation that can be tested (b) The fabricated and populated v02 - SBC Sense Board 84

6.6 Tissue detector response (data points) compared to a reference photodiode for a varying source power. Solid line is a linear fit to the data ($R^2 = 0.999$). 85

6.7 (a) Illustrating the difference between the cylindrical helix RXC (left) and the square helix RXC (right). (b) S21 comparison between the cylindrical helix RXC and a square helix RXC demonstrating a 4 dB improvement in S21 by using the square helix coil 87

6.8 (a) The TXC-RXC separation sweep experimental setup at 5cm separation (b) After sweep the RXC away from the TXC in 1cm steps, the resulting S11 and S22 (Top Left), S21 (Top Right), Z11 (Bottom Left), and Z11 Percent Change (Bottom Right) 88

6.9 v02 - SBC Sense Board with optically clear epoxy encapsulation. 89

6.10 The full system overview for the non-form-factor operation of the Smart Breast Clip v03 - Power RX 90

6.11 SBC v03 - Power Board block diagram. 91

6.12 SBC v03 - Power system Top (a), Bottom (b), and Side (c) views, with injectable delineated by red dashed line. 91

6.13 (a) The initial TX coil design with a loop of inner diameter 37 mm and and a spiral of of outer diameter 48 mm (b) Heating resulting from high power applied to the TXC. 94

6.14 The TX Coil with a 30x20 mm spiral resonator and 20x15 mm loop Top (a) and bottom (b). 95

6.15 (a) The Ansys HFSS model used for determining SAR Heating, including the TXC, RXC, and phantoms for skin, fat, and blood (b) The results of SAR Heating analysis after applying 1.75W of driving power to the TXC, showing a maximum value of 0.99W/kg. 96

6.16 The form-factor RX Coil fitting within a 12g Needle 96

6.17 The RX Coils associated with the (a) SBC v03 Power and (b) SBC v10 Mouse boards, measuring 30x2.3x1 mm and 16x2.3x1 mm, respectively 97

6.18 (a) The power consumed by the SBC v03 - Power board during full operation and then during sleep, demonstrating a 28.75% reduction in power consumption while sleeping. (b) An example of the start-up voltage sequence and showing the required current on the right hand axis for the SBC v03 - Power board 98

6.19 An example of the rectified voltage being regulated towards the target voltage of 4V. 99
6.20 (a) Blood oxygenation phantom used to test the how the prototype sensor responds to changing blood oxygenation (b) SBC v03 - Power data while monitoring whole blood phantom during reoxygenation during wired operation 101
6.21 The SBC v03 - Power data during fully wireless operation while measuring controlled intralipid solutions with varying optical absorption. The blue and red shaded regions represent the expected optical absorption for 680nm and 850nm, respectively, that will be encountered in tumors in vivo. 102
6.22 The system procedure for closed-loop automated operation. 121
6.23 The RX automated state machine. 122
6.24 (a)Demonstration of uplink data transmission from the v03 form-factor system. (b) Decoding of the received uplink data transmission 122
6.25 (a)Demonstration of downlink communication using the envelope detector. (b) Demonstration of downlink communication using direct sampling of VREC 123
6.26 (a) The simplified circuit for analysing Load Shift Keying (b) An alternate detection method using a secondary antenna coil for detecting LSK changes in the primary coil 123
6.27 An image showing the result of an attempt to laser cut the injectable PCB portion away from the carrier on the SBC v03 - Power board 124
6.28 An image showing the result of paring away unnecessary components from the SBC v03 - Power board in preparation for the design of the SBC v10 - Mouse 124
6.29 A block diagram showing the full system design used for the Smart Breast Clip v10 - Mouse board. 125
6.30 A block diagram demonstrating the form-factor RX system, v10 - SBC Mouse Board, that will be tested in a murine model. 125
6.31 (a) The SBC v10 - Mouse Top (b) The SBC v10 - Mouse within an 11g Needle 125
6.32 The power consumed by the SBC v10 - Mouse board during full operation and then during sleep, demonstrating a 21.27% reduction in power consumption while sleeping. 126
6.33 System Design for accommodating translational research on biological sensor and effector designs. 126
6.34 The ElectRX v02 board in detail. 127
6.35 (a) ElectRX v02 Top (b) ElectRX within an 11g Needle 127
6.36 The 2-turn RX Coil is embedded within the Internal Layers 1 (a) and 2 (b) with planar dimensions of 9.606 x 1.62 mm. 128

6.37 The 2-turn RX Coil is was found to have an (a) inductance of 44 nH and, (b) after tuning, achieved an S11 of -6.932 dB at 6.78 MHz. 128

LIST OF TABLES

Table Number Page

2.1 WLAN Packet Parameters. 16

3.1 Comparison of state-of-the-art wireless neural recorders 38

ACKNOWLEDGMENTS

This dissertation highlights the academic peaks achieved throughout my time at the University of Washington. Hidden beneath these clouds of text though is the arduous self-growth required to even scramble into the foothills. When I returned to academia after a long absence, I experienced the steepest learning curve that I can remember. Without the kind, empathetic, wise and concerted efforts of those around me, I do not believe I would have been able scale these heights. My sincerest gratitude is extended to every person, and organization, who trekked beside me on this journey.

More specifically though, I want to start by thanking Dr. Joshua Smith for taking a chance on a student without recent history in academia. The opportunity to work within your Sensor Systems group, and under your wise guidance, on exciting and ground breaking technologies has completely reoriented my life towards a path where I believe I can most productively support and encourage the world around me to flourish.

Within my time in the Sensor Systems group, I worked with many talented and impressive individuals. Your tutelage, guidance, empathy, and humor have helped me get through tough phases and made coming into the lab a joy. I wanted to specifically thank my close collaborators with whom we've been able to push the envelope of knowledge forward: Kedi Yan, Alicia Wei, Dr. Thomas O'Sullivan, Dr. James Rosenthal, Dr. Matt Reynolds, Dr. Lefteris Kampianakis, Dr. Apoorva Sharma, Dr. Richy Yun, Dr. Zerina Kapetanovic, Shanti Garman, Brody Mahoney, Dr. Vaishinavi Ranganathan, and Dr. Benjamin Waters.

My thanks also goes out to the school of Electrical and Computer Engineering

at the University of Washington and the many professors who have nurtured my growth. Beyond the confines of ECE of I would like to express my gratitude for the organizational and financial support provided by The Center for Neurotechnology. Without the opportunities the center brought forth, I don't know that I would have been able to redirect my towards my overarching goal of developing tools for the benefit of the neuroengineering ecosystem. In addition to funding from the Center for Neurotechnology, I also want to acknowledge the National Science Foundation (CNS-1823148, EEC-1028725), U.S. Department of Defense (W81XWH-20-1-0010), NSF Grant EEC-1028725, whose financial support allowed me to pursue academic goals and produce academic results that will hopefully one day benefit the whole of humanity.

Finally I want to thank those in my personal life who have uplifted me and aided me throughout this experience. My wife Nicole Jendro has provided immeasurable love and support, while also serving as a brilliant example of the type of person I aspire to be. My parents, aunt and uncle, and brothers have provided the kind of home life and fertile ground for growth that I wish all of humanity had access to. They believed in me and encouraged me to live my best life, no matter what forks in the road I may have followed.

Again, my sincerest thanks to you all!

Chapter 1
INTRODUCTION

1.1 Implantable, Injectable, and Ingestible Electroceuticals

Implantable, injectable, and ingestible electroceuticals (I3E) are revolutionizing medical care. A patient's medical team can now safely monitor and implement medical condition treatments in real-time without requiring the patient to be tethered to a medical treatment station and the associated attendant medical practitioner. This freedom is accomplished by designing low-power, bio-compatible, heat-limited electronic systems that can operate for extended periods away from a power source, via battery or power harvesting, and communicate with the external world wirelessly, via non-radiative electromagnetics or light. As I3E gain further adoption by the general public, the untethered direct monitoring of human physiology will allow for better controls in the aid of early recognition of pathological conditions. By comparison, medical devices for internal body conditions that require puncturing the protective dermis and other insulating tissue, will always provide an open vector for infection and monetary costs of specialized care to administer the monitoring and treatment increase far beyond the cost of the stand-alone medical device. Alternatively, wellness tracking wearables have provided relatively inexpensive health monitoring by inference. That being said, the time dependent primary biological signals of interest can be buried the correlated analytes that can be readily measured.

I3E exist between the tethered implanted and wearable electronic medical devices. They require a single medically safe insertion, but then can operate continuously until their eventual excision. With meticulous operation and installation, the sensor can then monitor the analyte or biological signal directly and influence the tissue as designed. 8 to 10% of the population in America and 5 to 6% in industrialized countries have experienced benefits from implantable biomedical devices [11].

1.1.1 Implantable Electroceuticals

Implantable electroceuticals exist as the most invasive of the three systems. These systems lack form-factor restrictions beyond conforming to highly curved anatomical structures and avoiding tissue damage or chronic inflammation, which may lead to carcinogenesis [12]. However, they require much greater care during insertion as the surgical site can act as a vector for infection. Some of the most common commercially available implantables are shown in the table below:

Implantable	Implants per Year	Source
Pacemaker	181250	[13]
Cochlear Implant	219888	[14]
Left Ventricular Assist Devices	4048	[15]

Within the experimental realm, an wide array of electrical wireless physiological sensors, effectors, and control systems are being investigated [16], with an exciting subset of these involved in neurological closed-looped systems that have been developed for neural recording and stimulation [17], [18], [19]. In general, due to the invasive nature implantation and excision, the implant should run at low enough power to either subsist on the co-implanted battery for the lifetime of the implant or receive wireless power to run or recharge the implant via electromagnetic, ultrasonic, or bio-fuel modalities. The wireless communication of data is then predominantly accomplished at 402MHz and 6GHz (UWB), where the higher frequencies are preferred for high data rate communication reaching into 100s Mbps [20].

1.1.2 Ingestible Electroceuticals

Ingestible electroceuticals have a moderate aspect ratio that enables the systems to move within the GI tract. The approximately 11mm x 26mm size of commercially available systems is constrained by the average diameter of an adult upper esophagus. These devices have allowed medical practitioners to monitor temperature, pH, pressure, and oxygen level [21], in addition to primarily serving as wireless endoscope by transmitting high-frame rate video

to external systems [22]. Beyond just monitoring physiology, the Medimetrics IntelliCap system can deliver drugs to specific locations along the GI tract [23] and Abilify MyCite have an ingestible sensor that can help track patient dosing frequency adherence [24]. These systems commonly use internationally reserved industrial, scientific and medical frequency bands, which exist between 402MHz and 2.4GHz for data transmission. They generally rely on battery power, since they will only be within the body temporarily, as the device passes through the tract of the patient.

1.1.3 Injectable Electroceuticals

Injectables exist as a low invasive high-aspect ratio form-factor defined alternative to implantables [25]. By fitting within the confines of a hypodermic needle, injectables can be implanted quickly and safely using only outpatient services. The lack of an incision means there are no stitches required and the likelihood of infection is lowered due to the lower exposure of internal tissue to the external world. The most common example of a injectable would be microchipping that is used to identify pets, and some bio-hackers [26], however the recently FDA approved Eversense glucose 90-day monitor, Fig. 1.1a, by Sensionics [27] is demonstrating how the field could possibly expand. This 3.5mm x 18.3mm injectable electroceutical uses a patented fluorescent glucose-indicating polymer technology to measure glucose in the interstitial fluid (a thin layer of fluid that surrounds the body's cells). The battery-free sensor then load modulates the carrier from a smart transmitter to transmit the data. Both the measurement and calculation of glucose values are done automatically every 5 minutes [28]. For the purposes of pain control, the FDA has also approved the StimRouter, a 150mm x 1.5mm conductor for routing a stimulating field towards a targeted peripheral nerve [29]. In the research realm, via the BION injectable (Fig. 1.1b), injectables both RF or battery powered are being evaluated for assisting in rehabilitation, neurostimulation, and treatment for ulcers, hemicranias, and urinary incontinence [30].

(a) (b)

Figure 1.1: (a) Sensionics Eversense glucose 90-day monitor (b) 3 Bion microstimulator variants that have been tested in clinical studies

1.2 Enabling Electroceuticals via Wireless Power Transfer and Low-power Backscatter Communication

1.2.1 Operating Frequency Selection

No matter the sensed signal, common to all of these electroceuticals is the need to provide safe power, controls, and telemetry to circuitry within a lossy, organic medium. To address the environment first, the lossy medium absorbs EM energy. This absorption increases with frequency and with depth into tissue due to its high dielectric permittivity [31]. In Fig. 1.2a, the penetration depth of a EM source is shown to decrease exponentially with frequency increase [1]. As efficiency is lost the power transmitted must increase to accommodate deeply inserted or power hungry devices. While the loss in end-to-end efficiency significantly impairs wireless connectivity, further undermining the use of UHF frequencies typically used in far-field communication systems is the substantial heating of tissues between the transmitter and receiver [32]. This Specific Absorption Ratio (SAR) heating is constrained by governmental health regulating bodies (IEEE, ICNIRP, FCC) for the general public to be 0.08 W/kg for the whole body average and 2-4 W/kg for localized SAR in the head/trunk and limbs,

respectively [33]. On the other end of the spectrum, the Induced Electric Field (E_i), and in turn Induced Current, increases as frequency decreases. The possible damage to biological tissue resulting high E_i is again regulated by the same bodies as above.

As shown in Fig. 1.2b a minimum regulatory limit between SAR and E_i can be found around 1.5MHz, however the lowest common global frequency allowed for medical devices (ISM) is 6.78MHz (BW = 15kHz) and so this becomes the natural target for efficient wireless transfer. As an example of the prospects of choosing this ISM band, recently a commercial 30W product charging mat by Witricity passed SAR certification testing (E_i being negligible at this frequency) [34] allowing even as system with high power output to be distributed to the general public. As an additional benefit of using this frequency, metal object heating caused by magnetic fields at 6.78 MHz is negligible compared to lower frequency wireless transmission, because eddy current losses induced in nearby metal objects are reduced with the square root of the frequency increase [35]. This becomes important as there is less restriction on encapsulation materials for the inserted medical devices. Also, if the encapsulation material is able to be heat conductive, then some of the heat can be transferred away via interstitial fluid throughout biological tissue.

1.2.2 Power: Near Field Magnetic Resonant Coupling

Pairing the optimum 6.78MHz frequency of wireless transmission, as discussed above, with Near field Magnetic Resonant Coupling (NF-MRC) provides the capability of delivering high power transfer efficiency (PTE) to medical devices that are embedded in biological tissue. A simplified diagram of a typical NF-MRC system is shown in Fig. 1.3b. An external high-power consuming system system (TX) consisting of a power amplifier, usually Class-E to take advantage of high operating efficiency up to a few tens of MHz [4], drives a transmitting coil/resonator (TXC) tuned to the chosen resonant frequency using an impedance matching network (TXIM) or via Self-resonant Tuning. A weakly-coupled coupled receiving coil/resonator (RXC), $k = \frac{M}{\sqrt{L_{TX}L_{RX}}}$ where M is the Mutual Inductance, tuned in a similar manner to the resonant frequency, then drives a AC-DC converter, usually a Zener Diode or

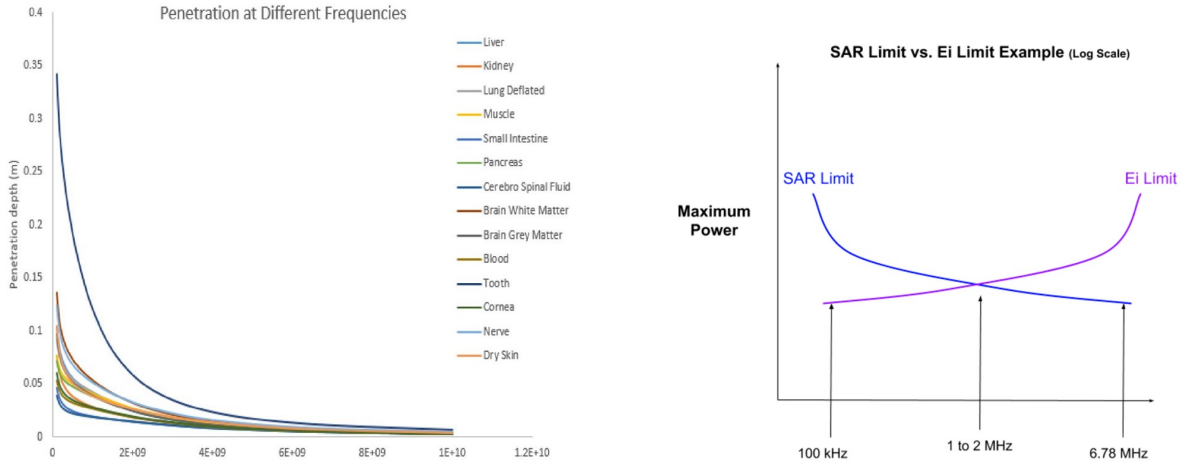

(a) (b)

Figure 1.2: (a) Tissue penetration of an EM field for various tissues demonstrating an exponential decrease due to frequency [1] (b) SAR and E_i regulatory curves demonstrating how frequency selection must be made to satisfy both. [2]

MOSFET based Full-Wave Bridge rectifier. This rectified voltage is then regulated, via up or down-converters, to the required system voltage. Energy is stored in a capacitor array (C_Tank) or on co-impanted batteries. This energy is then available to drive the required load, be it a sensor, stimulator, or control system.

By designing for the magnetic field to transmit power, rather than the electric field, the wireless channel experiences lower SAR heating and negligible channel variations due to inhomogeneous tissues, since most biological materials have a permeability of approximately 1 [36]. As opposed to pure inductive power transfer, by tuning the combined TX to RX system to a single resonant frequency, high Q-factor transmission can be achieved. This makes the coils less sensitive to misalignment and increases the PTE, as less transmitted power can achieve the same received power at the load, which in turn decreases coil heating [35].

1.2.3 Communication: Simultaneous Wireless Power and Transfer

Excluding the implantable neural recording interfaces and the high frame-rate video relay ingestibles, the electroceuticals all share a need for only low data rate transmission. Most

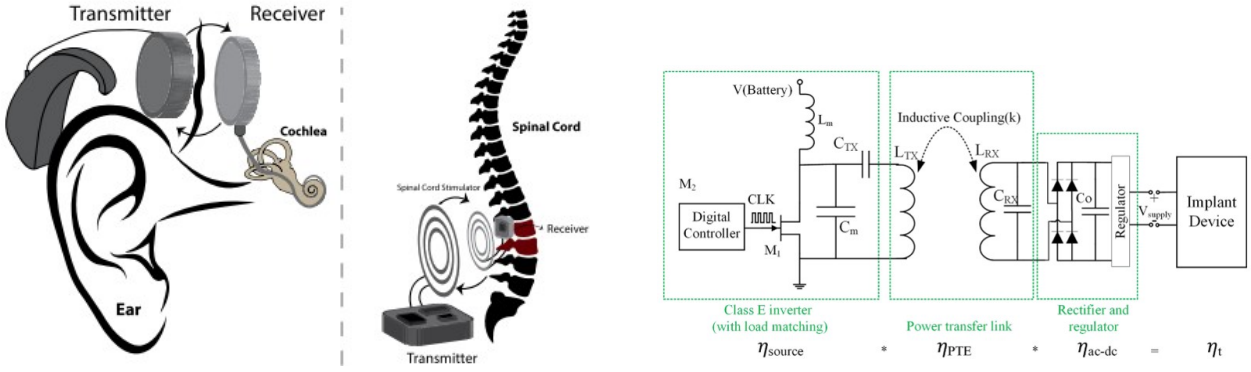

(a) (b)

Figure 1.3: (a) Cochlear implant and spinal cord stimulator examples of applied NF-MRC system [3] (b) Equivalent circuit model for a generic NF-MRC system [4]

of human physiology metrics change at the rate of seconds or even hours, allowing for a beneficial tradeoff of circuit complexity and high power consumption for size. This fortunate feature allows for higher-Q coils to be implemented, which increases PTE, since BW is inversely proportional to Q-factor.

Targeting low data rate sub-sector of I3E allows the medical device to have reduced telemetry complexity, which in turn allows for significant power, space, and cost savings. Further simplification of the architecture can be achieved by limiting the system to a single RXC, time-multiplexed between power and data transfers. This Simultaneous Wireless Power and Transfer (SWIPT) can enable achieve substantially improved energy and spectrum efficiencies, as compared to separate WPT and wireless communication systems that operate independently [37]. SWIPT can be implemented via a variation on Amplitude Shift Keying (ASK) called Load Shift Keying, which identifies the reflected impedance in the TXC via a changing load impedance of the RXC. The load impedance change can be implemented as shown in Fig. 1.4a. When the receiver is to uplink data back to the external system the TX/RX Switch connects to the load modulating second switch which is connected to Z1 and Z2 loads. While the receiver is not uplinking, which is a majority of the time in low

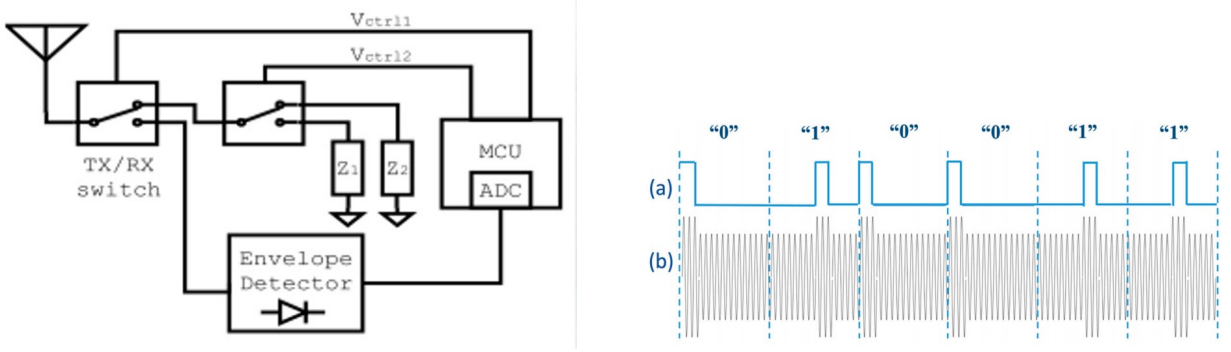

(a) (b)

Figure 1.4: (a) A receiver based Load Shift Keying circuit model [5] (b) Using Load Shift Keying with a variation on Manchester Encoding, the TX impedance is modulated [6]

data rate I3E, the TX/RX Switch is connected to the rectification circuit in parallel, which can also serve as the first stage of an Envelope Detector. Using a variation on Manchester Encoding, the TXC modulation, approximated graphically in Fig. 1.4b, is recovered using the output of a directional coupler inline with the TXC. Care must be taken to keep the coupling coefficient k above 0.1 or the Bit Error Rate dramatically increases, and below 0.05 the load modulation can not be detected [38]. The positive side of this limited range though is that medical telemetry will be limited to the secure area directly around the tissue being interrogated and if multiple I3E are used, the systems can reuse the same frequency without significant interference [39].

1.3 Contributions and Thesis Organization

1.3.1 Original Contributions

1. Kapetanovic, Z., Moore, G.E., Garman, S., & Smith, J.R. (2020). Classifying WLAN Packets from the RF Envelope: Towards More Efficient Wireless Network Performance. Proceedings of the 4th International Workshop on Embedded and Mobile Deep Learning.

    - The development of Packet Assay, a power efficient method to classify each protocol and packet type without requiring any prior demodulation, and a RF

dataset for IEEE 802.11b/g/n protocols containing over 600K labeled (modulation scheme, protocol, packet type, data rate, and address) packets.

2. Rosenthal, James D., Moore, Gregory E., Smith, Joshua R., & Reynolds, Matthew S. (2021) Wireless power and communication for implanted electronics. In Review.

    - A description of recent advances in HF and UHF wireless power transfer and communication for implanted devices. We present an HF-powered neural recording and stimulation platform for implanted biomedical devices that communicates by UHF backscatter communication, achieving data rates of up to 25 Mbps using DQPSK. The HF WPT system enables periodic recharging of the device's battery, facilitated by a dynamically-configured HF coil array that enables improved spatial freedom as research animals move across a large surface area

3. Moore, G.E., Khan, U.M., Yang, T., Yan, K., Nguyen, T., Kuang, S.M., Whyte, C., Ranganathan, V., & Smith, J.R. (2021). A Low-Cost, Open-Sourced Platform for High-Fidelity Characterization of Large WPT Coils. 2021 IEEE Wireless Power Transfer Conference (WPTC), 1-4.

    - A description of the Mostly Printed Field Characterization System (MPFCS). An accurate, inexpensive, and open-source platform for high-fidelity, rapid, large volume WPT coil field characterizations that provides a significant reduction in scan duration in comparison to similar simulations.

4. Yan, Kedi, Moore G.E., & Smith J.R. (2022) "Analysis and Design of a Multi-hop Resonant Wireless Power Transfer System: Optimal Intermediate Coil Size and Location." 2022 Wireless Power Week (WPW) (2022): 454-459.

    - Methodologies and formulas for choosing the optimal size and location of an IC that provides a required transferred power to the load in a standard four-coil

systems. Increasing the size of the IC will result in diminishing returns, so the optimal size depends on the target power ratio. The optimal location depends on the size of the IC and the separation of transmitting and receiving coils.

5. Wei, A.Y., Moore, G.E., Yan, K., Mahoney, B.J., Smith, J.R., & O'Sullivan, T.D. (2022). Smart breast clip: A wireless implant for continuous molecular sensing of breast masses. Label-free Biomedical Imaging and Sensing (LBIS) 2022.

    - A minimally invasive, needle-injectable, wirelessly-powered diffuse optical spectroscopy sensor implant that fits within a 12G breast biopsy needle. The sensor uses red and near-infrared lasers to measure tumor hemoglobin concentration changes. This ultralow power sensor is wirelessly powered using near-field resonant inductive coupling and communicates via backscattered load shift keying. Characterization in liquid tissue mimicking phantoms showed a response to absorption concentrations consistent with estimated tumor hemoglobin concentrations.

1.3.2 Thesis Organization

The remainder of this Thesis is organized as follows: Chapters 2 to 5 elaborate on the published works listed in Sec. 1.3.1. Each work provided foundation towards the development of Commercial Off-the-shelf Injectable Electroceuticals in Chapter 6. The thesis concludes in Chapter 7.

Chapter 2

CLASSIFYING WLAN PACKETS FROM THE RF ENVELOPE: TOWARDS MORE EFFICIENT WIRELESS NETWORK PERFORMANCE

2.1 Introduction

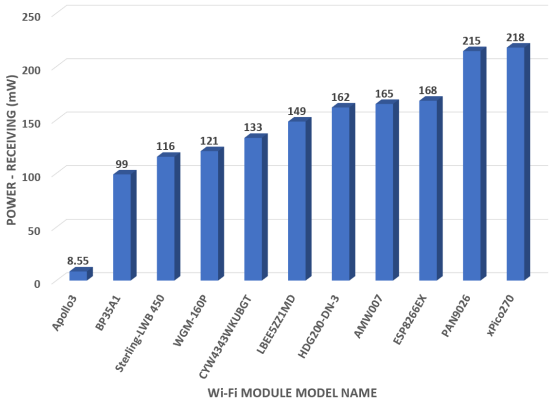

Figure 2.1: Wi-Fi Module Receive Packet Discrimination Power Comparison. Commercially available Wi-Fi Modules consume significantly more power than low-power microprocessors such as the Ambiq Apollo3 Blue.

Next generation wireless devices are expected to have great performance enhancements, from supporting higher data rates and large-scale networks, to enabling a variety of new low-power applications. Achieving these advancements requires a new paradigm for wireless technology. Recently machine learning (ML) techniques have helped to significantly advance numerous fields and those advancements can be extended to the wireless domain as well. For instance, as highlighted in [40], ML can be used to tackle several technical problems related to wireless networks such as channel estimation, spectrum sensing, anomaly and fault detection, or energy modeling for energy harvesting applications. In this paper we focus on how ML can be leveraged to improve WLAN power consumption performance from both a hardware

and software standpoint without demodulating the radio frequency (RF) signal.

To attain the performance boost from ML methods we must first develop a high quality training dataset of RF signals resulting from WLAN exchanges. A majority of WLAN datasets available today are network traces that provide information such as network traffic, packet characteristics (e.g. protocol, data rate, packet type), or channel quality information (e.g. RSSI). Using such datasets, several works have shown how ML can be used to improve WLANs. For example, predicting WLAN traffic using SVM-based models [41]. Generating such datasets is time consuming as it requires using specialized equipment like software-defined radios (SDR) to receive RF signals and then properly labeling each packet with its associated characteristics. We envision that instantiated ML from this dataset can lead to significantly lower power operation via optimized hardware systems design.

One of the most power consuming components of wireless devices is the WM. As shown in Fig. 2.1, a typical demodulating receiver dissipates energy at a rate several orders of magnitude greater than any associated processing unit and memory, such as an Ambiq Apollo3 Blue. By offloading a portion of the packet discrimination responsibilities from a modulated RF source to a sparse ML model deployed on an ultra-low power processor we can achieve significant power savings by minimizing the active time of a WM, favoring inactive or sleep states.

To realize this vision, we present Packet Assay (PASS), a new technique to extract discriminating information from the envelope of WLAN packets' RF signals by using a sparse NN. Using a simple rectifier, the envelope of WLAN signals can be retrieved and by leveraging the evolving capability of low-power microcontrollers (MCUs) to deploy sparse, accurate NNs, PASS can operate at the low-power demanded by IoT devices. The information gained through classification will then allow for efficiency gains along multiple performance dimensions.

To demonstrate the feasibility of PASS, we develop a dataset of enveloped WLAN RF signals from which we identify key characteristics of WLAN packets, such as protocol or packet type without necessitating power consuming demodulation. With insight into these

packet properties PASS can enable intelligent decisions about how devices should integrate WLAN received information.

In this paper we present the following key contributions,

- A new RF dataset for IEEE 802.11b/g/n protocols containing over 600K labeled (modulation scheme, protocol, packet type, data rate, and address) packets.
- Packet Assay, a power efficient method to classify each protocol and packet type without requiring any prior demodulation, is demonstrated.
- Packet Assay paradigm opportunities are further explored.

2.2 Related Work

There are several areas of research related to our work, including dataset development and using ML for signal classification. We highlight each of these areas below.

WLAN Dataset Development: A handful of large established datasets are commonly used for benchmarking ML algorithms, including MNIST, a database of handwritten digits [42] and CIFAR10, a dataset of everyday object images [43]. To our knowledge, there does not currently exist an equivalent dataset of WLAN RF signals. Rather, the majority of available WLAN packet data exists in the form of captured or "sniffed" packets collected on a PC using network protocol analyzer software such as Wireshark.

CRAWDAD [44] has several examples of wireless signal datasets in the form of packet traces, including Wi-Fi, Zigbee, 4G/5G LTE, and GPS. However, when it comes to WLAN RF signals, most available datasets consist of narrow, application-specific WLAN signal attributes (e.g. signal strength or location coordinates), which were generated to support specific research efforts such as Wi-Fi coverage mapping efforts [45] and user proximity detection [46]. Furthermore, we identify a lack of WLAN data captured in its complex in-phase (I) and quadrature (Q) form within its RF band.

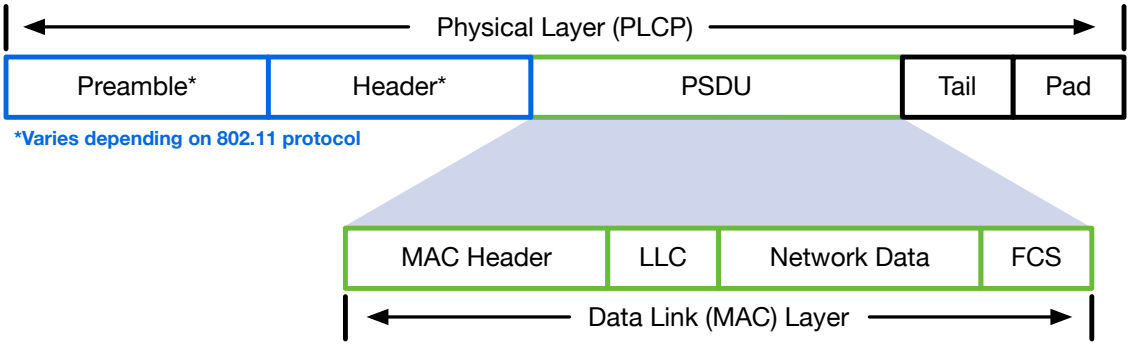

Figure 2.2: WLAN Packet Structure. The high-level packet structure for IEEE 802.11b/g/n protocols.

Machine Learning for Signal Classification: ML has been leveraged to perform protocol classification, radio fingerprinting, and much more in regards to wireless communication and networking. Most use cases involve using convolutional neural networks (CNN) and Deep Neural Networks to perform classification. For example, CNNs have been used for wireless interference identification across several WLAN standards using the IQ data of complex baseband signals [47]. Similarly, IQ data of IEEE 802.11ac packets has been used to train CNNs for radio identification, reaching experimental accuracy of 90-99% [48]. Research in radio modulation recognition has also found CNNs to provide high accuracy classification of low SNR signals [49]. Additionally, DeepPacket uses a CNN architecture to perform both application identification and traffic characterization, where the dataset consists of packet information at the data link layer [50]. However, the power consumption of such implementations have not been fully considered, which is a key parameter when working towards practical implementations in IoT. Moreover, to gather the commonly used input data (e.g. IQ, physical/MAC layer data) would require more power consuming hardware.

2.3 WLAN Primer

WLAN is a wireless network that links devices using various wireless communication protocols to create a local area network (LAN) and in turn, provide Internet access. Most WLANs are based on the IEEE 802.11 standard, which are used to enable Wi-Fi. The vari-

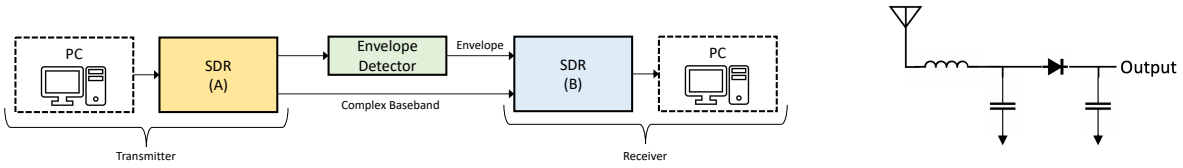

(a) (b)

Figure 2.3: Generating an RF WLAN Dataset: (a) Our data collection setup. We use two Ettus SDRs, an envelope detector, and PC. Data is collected in two formats: (1) complex baseband and (2) baseband envelope. (b) We implement the envelope detector circuit operating at 2.4GHz using passive hardware components.

ation between protocols includes the media access control (MAC) and physical layer (PHY), as well as frequency range of operation. While there are many different 802.11 protocols, we will focus on those in the 2.4GHz range and provide a primer on IEEE 802.11b/g/n, which are widely used in today's Wi-Fi networks:

- 802.11b: The 802.11b protocol operates across all 14 channels in the 2.4GHz ISM band with a channel bandwidth of 20MHz. It uses direct-sequence spread spectrum (DSSS) modulation and achieves data rates up to 11Mbps.

- 802.11g: The 802.11g protocol operates at 2.4GHz and supports orthogonal frequency division multiplexing (OFDM) modulation. This allows 11g to reach higher data rates, up to 54Mbps. 802.11g operates across all 14 channels, each with 20MHz bandwidth.

- 802.11n: The 802.11n protocol improves upon previous standards by introducing multiple-input multiple-output (MIMO). 802.11n can operate in both 2.4 and 5GHz bands. As relevant to this work, in the 2.4GHz band 11n can operate with a channel bandwidth of either 20 or 40MHz using OFDM modulation. Depending on the channel bandwidth, modulation and coding scheme (MCS), and number of spatial streams used, the data rate will vary but can achieve up to 150Mbps.

A WLAN packet's structure, as shown in Fig. 2.2, can be broken down into two key

Table 2.1: WLAN Packet Parameters.

Protocol	Packet Type	MCS	Data Rate (Mbps)
802.11b	Beacon, Data QoS Data, QoS Null Block ACK, ACK RTS, CTS, Null	DSSS+DBPSK DSSS+DQPSK CCK5.5M+DQPSK CCK11M+DQPSK	1, 2, 5.5, 11
802.11g		BPSK 1/2, 3/4 QPSK 1/2, 3/4 16QAM 1/2, 3/4 64QAM 2/3, 3/4	6, 9, 12, 18, 24, 36, 48, 54
802.11n		BPSK 1/2 QPSK 1/2, 3/4 16QAM 1/2, 3/4 64QAM 2/3, 3/4, 5/6	6.5, 13, 19.5, 26, 39, 52, 58.5, 65

components: a preamble and data field. Every preamble will include a short training, long training, and signal fields that carry packet information (e.g. rate, length). The data field includes PLCP service data unit (PSDU), tail, and pad bits. The PSDU is a view of the MAC protocol data unit (MPDU) from the physical layer and the MPDU contains MAC frame information such as frame type, addresses, and various other packet configuration properties. There are also a variety of packet types that each protocol supports for Wi-Fi. This includes control packets such as beacons or acknowledgments and also data packets. Table 2.1 shows an overview for each protocol.

2.4 WLAN Dataset Development

To generate Wi-Fi packets we use the MATLAB WLAN Toolbox to create custom physical layer frames for IEEE 802.11b/g/n protocols [51]. For each protocol we vary the modulation and coding scheme, data rate, packet type, and payload if applicable. 11b has four distinct combinations of spreading, coding scheme, and modulation. These include either a barker code plus DBPSK or DQPSK, or complementary code keying (CCK) with DQPSK. Since both 11g and 11n protocols use OFDM, the MCS can take on eight different modulation and coding scheme settings. This includes BPSK, QPSK, 16-QAM, and 64-QAM at

varying coding rates. These settings will also define what data rate is used. While 11n does support MIMO, we only generate packets with a single spatial stream when creating our dataset, and 20MHz channels are used with 800ns guard intervals. Moreover, the payload for data packets is randomly generated for each packet and similarly the service set identifier (SSID) for every beacon is randomly generated as well.

We generate two types of datasets, one with complex baseband signals and the other with the envelope of each signal. Since we want to explore using ML for low-power applications, a dataset with the envelope of each signal is more suitable. The reasoning is that envelope detectors operate at very low-power, in fact, they can be completely passive. For low-power applications, we want to minimize the power consumption as much as possible and demonstrate that we can still achieve high accuracy with our design. While we are limiting our scope to low-power applications, there are still many applications that are not power-constrained for which a dataset of complex baseband signals can aid research efforts. We plan to open source both datasets for other researchers.

To extract the envelope of an RF signal, we need to perform additional processing. Mathematically, the most accurate approximation of a signal envelope is simply the absolute value of the in-phase and quadrature components of a complex baseband signal,

$$s_{env} = |I(s) + Q(s)| \tag{2.1}$$

where s is the complex baseband signal. Given this, we can extract the envelope of the signal by simply applying Eq. 2.1 in software. However, a challenge arises with this approach, primarily impacting 802.11b packets. Since 802.11b uses DPSK, the signal has values of either +1 or -1. When we take the absolute value of this we get a constant +1, which is not realistic and would provide no meaningful insights. To have a more realistic dataset for training purposes we choose to transmit all signals at 2.4GHz and receive using an envelope detector circuit as the RF front-end. Moreover, this approach also demonstrates the feasibility of using low-power hardware while still achieving high classification accuracy.

To collect data we use two SDRs, an envelope detector, and a PC. Each SDR uses a sampling rate of 20Msps. Fig. 2.3a shows our setup. SDR-A is connected to the PC which transmits the WLAN packets and SDR-B receives the transmissions. We collected data in two settings. First, passing the received signal through the envelope detector and the other directly to SDR-B to get the complex baseband signal. The envelope detector is implemented as shown in Fig. 2.3b as an impedance matched half-wave rectifier and low-pass filter. This design has zero power overhead since all components are passive.

We collect 360,000 enveloped packets and 240,000 complex baseband packets evenly split between the 3 protocols and 9 packet types of 802.11b/g/n, where each packet is labeled based on protocol, packet type, and MCS. Fig. 2.4b shows an example of a recorded 802.llg packet in the form of a baseband envelope signal.

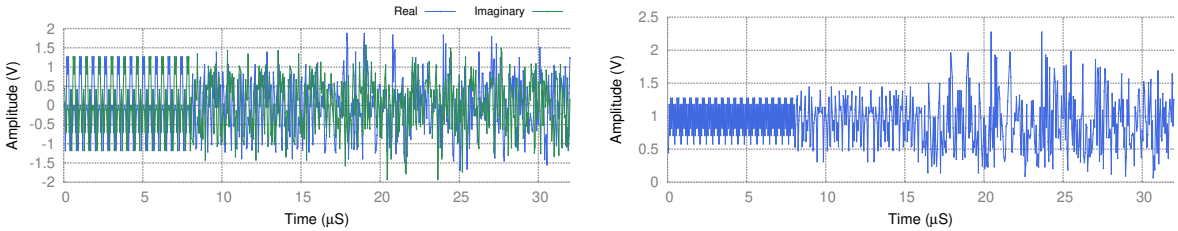

(a) Complex Baseband Signal. The complex baseband signal of an 802.11g beacon frame.

(b) Envelope Signal. The computed envelope of an 802.11g beacon frame.

Figure 2.4: WLAN Data Preprocessing. An example of WLAN data packet before and after generating the envelope signal.

To verify the packets generated by the MATLAB toolkit are standard compliant we use a SDR to transmit packets over the air and receive them with legacy receivers. Specifically, we used a PC running Wireshark to verify packet reception. We found that each packet generated using Matlab's WLAN Toolkit was successfully received and demodulated.

The resulting enveloped WLAN packet dataset has many properties unique to WLAN packets. Firstly, within a given protocol type the data rate differs while the classification must remain the same. This data rate difference results in a recorded sequence length difference, which is downsampled according to the ADC sample rate. Specifically, we are targeting the

ADC sampling rate of low-power MCUs, which typically sample at a few Msps. Secondly, there is sequential similarity between 802.11 packets, due to the protocol dictates. Finally, as can be intuited from the UMAP representation (nearest neighbors = 15) of a representative sample of the data set (N=180K packets, M=256 samples) shown in Fig. 2.6, there aren't obvious non-complex manifolds that segment the data, though there are many packets types that tightly cluster.

2.5 Neural Network Architecture

In order to implement PASS for efficient low-power operation on enveloped WLAN data, we need a sparse, shallow, and accurate classification network that can learn complex decision boundaries. Increasing sparsity reduces the trainable parameters employed in a network and thus compresses the required memory space. A shallow network reduces the number of weighted layers between the input and the eventual classification, thereby providing faster inference times. With non-optimized classification models there will be a trade-off between accuracy, compression, and speed.

To perform WLAN packet identification we implement a sparse, shallow CNN and classify two characteristics: protocol and packet type. CNNs have the flexibility to segment the WLAN dataset (Fig. 2.6) with a high degree of accuracy. Additionally, via Neural Architecture Search (NAS) and pruning, they can be sparse and shallow enough to fit within the limited memory capacity of a MCU's flash memory while storing intermediate data within the static RAM [52].

As shown in Fig. 2.5, the CNN employed to accomplish PASS has two layers. In the first layer the RF signal input($input\_sequence = 256\, samples$) initially goes through a 1D convolution filter ($filters = 1, kernel\_size = 20$) that extracts features by convolving a 1D kernel, a spatial filter, across the input data. The output of the convolution is then fed through a ReLu activation ($ReLu(x) = max\{0, x\}$) that provides a piecewise-linear transformation of the convolved output. Completing the first layer, a max pooling layer ($pool\_size = 5, stride\_size = 2$) is applied to the data, thereby downsampling with averaging the ReLu output to a lower set of dimensions. This is finally followed by a dropout layer, a

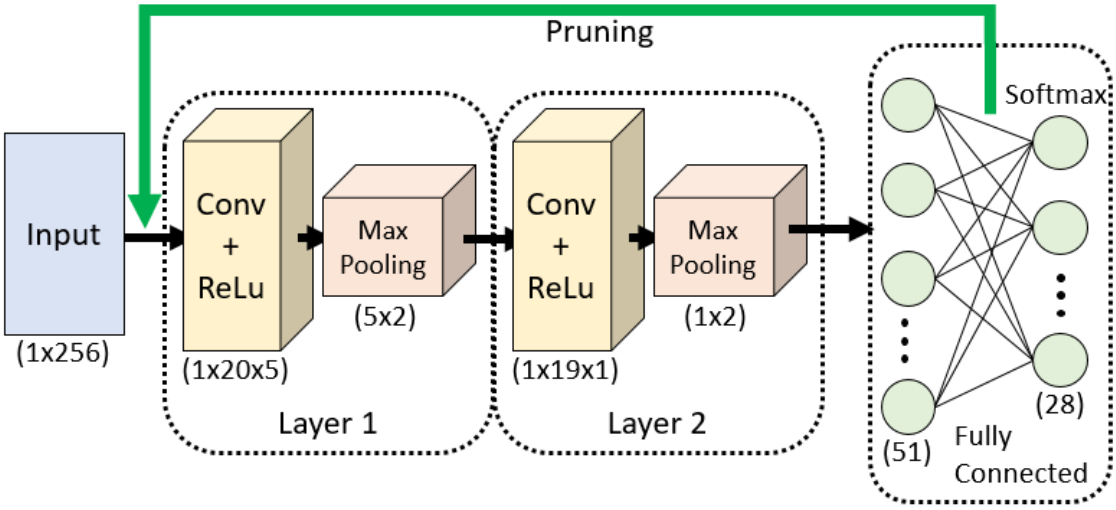

Figure 2.5: Two Layer CNN: The CNN contains two pruned convolution + max pooling layers that are used for packet classification.

regularization method that drops-out nodes randomly thereby emulating multiple network architectures within a single training run. The output of the first layer is input to the replica architectured second layer, but with $filters = 1, kernel\_size = 19$, and $pool\_size = 1$. This is followed by a fully connected layer to a softmax output activation that provides the classification probabilities for each of the 28 outputs.

To encourage sparsity within the trained network, and thereby increase compression of the network, after training with 2000 batches, a pruning schedule is implemented at a frequency of once every 100 batches. The pruning gradually zeroes out model weights during the training process where possible [53].

Additionally, to encourage a sparse, fast, and accurate network architecture, the hyper-parameters are chosen by a simple NAS to provide the minimum loss with respect to a given evaluated model size (MS), measured in bytes after compression and quantization via TFLite [53]. This MS weighted loss ($\mathcal{L}$) variation on the Bayesian hyperparameter search is an extension on the standard implementation of the *Hyperopt* package [54]. The optimum

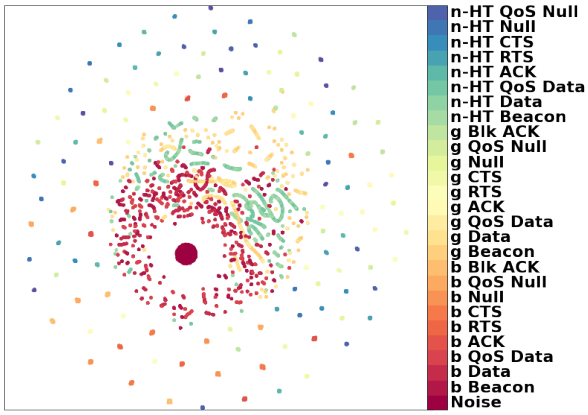

Figure 2.6: UMAP Representation of WLAN Enveloped Signals: A structurally similar representation of the high dimensional mapped to 2D demonstrating the difficult separability between classifications [7].

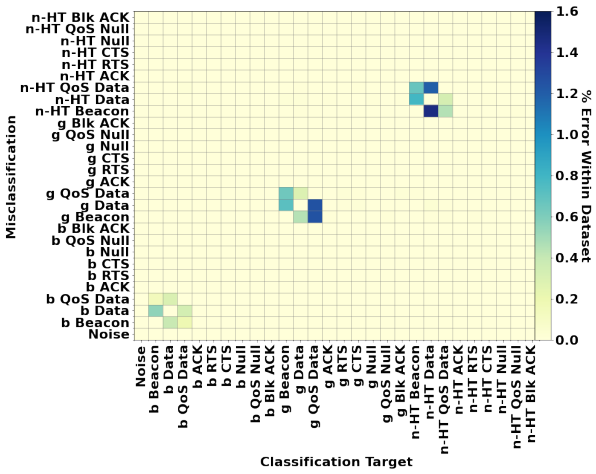

Figure 2.7: Confusion Matrix: The overall error rate for the 2-Layer Sparse CNN was 11.9%. False-negatives (columns), cluster with the false-positives (rows) around the Beacon, QoS Data, and Data packet types.

hyperparameter set, $\overset{*}{\lambda}$, was determined to be,

$$\overset{*}{\boldsymbol{\lambda}} = \arg\min_{\boldsymbol{\lambda}\in\boldsymbol{\Lambda}} \frac{\mathcal{L}_{\boldsymbol{\lambda}} * MS_{\lambda}}{MS_{target}} \tag{2.2}$$

where $\boldsymbol{\Lambda} = \boldsymbol{\Lambda_0} \times \boldsymbol{\Lambda_1} \times \ldots \times \boldsymbol{\Lambda_N}$ is the overall hyperparameter configuration space, λ is a vector of hyperparameters, and MS_{target} is the targeted memory space size, serving as a normalization parameter. For the purpose of implementing PASS on a modern low-power MCU with limited flash memory $MS_{target} = 20KB$ was chosen.

2.6 Results

In the following we present the experimental setup and empirical evaluation of PASS using a 2-layer CNN.

2.6.1 Experimental Setup

In order to evaluate PASS, an analog enveloped WLAN dataset of 180K packets evenly split between each of the 27 802.11b/g/n + 1 Noise ($\mathcal{N}(0.0, 0.05)$ scaled (2.0x) relative to dataset magnitudes) classifications was developed according to the procedure described in Section 2.4 for both training and testing our CNN. As we are targeting implementation of PASS on low-power devices, and consequently for low-power ADCs, the enveloped WLAN packets captured via the setup shown in Fig. 2.3a were downsampled by 4x to 5Msps. The dataset is then split into training, validation, and testing with a total of 129600, 14400, and 36000 packets, respectively.

We implement the CNN architecture described in the Section 2.5 in Python using *Tensorflow Keras* in combination with the *tensorflow_model_optimization* package for pruning towards network sparsity [53] and *Hyperopt* for network architecture optimization. The training was completed using the Adam Optimizer ($lr = 375 * 10^{-6}, \beta_1 = 0.9, \beta_2 = 0.999$, and $\epsilon = 10^{-7}$) [55] and the sparse categorical cross-entropy loss function. The performance of the network is evaluated via the sparse categorical accuracy of classification.

2.6.2 Accuracy Evaluation

After 500 epochs, the loss stabilizes and the network evaluated on the test dataset returns 88.1% sparse categorical accuracy with a stripped pruned set of 1497 parameters. The resulting model memory footprint is then 26.7KB, and then after compression and quantization via *TFLite* [53] the deployable model is 4.9KB.

As would be expected from the UMAP representation of the data in Fig. 2.6, the CNN misclassifications, as shown in the confusion matrix in Fig. 2.7, are not uniform across all packets. For example, when segmenting between b/g/n protocols, the accuracy is nearly perfect. However, the majority of the misclassifications exist within relatively few packet types and more specifically the false-positives are qualitatively mirrored as false-negatives. These cross-misclassifications center around the Beacon, QoS Data, and Data packet types (in descending order of misclassification magnitude) of the b, g, and n protocols, though no

set of misclassifications exceeds 2% of the dataset.

Additional efforts were made to train the models using RNN and CNN-RNN models, however the RNN alone achieved accuracies of less than 30% and the CNN-RNN's accuracy improvement over the CNN alone were negligible, while the size of both, even after application of the NAS (Eq. 2.2), exceeded the 20KB space restrictions.

2.7 Applications

In Section 2.6 we demonstrated that by using PASS we can accurately classify several key characteristics of WLAN packets, such as protocol and packet type, by only using received RF signal envelope. This opens up a wide range of low-power applications that can help improve the performance of WLANs. We present two particular examples, an intelligent low-power wake-up receiver and a new approach for managing IoT devices in Wi-Fi networking scenarios.

- Low-Power Augmented Wake-up Receiver: One of the most power hungry elements within wireless devices is the WM. Several approaches have been developed to address reducing the power consumption of WMs, ranging from power centered hardware design to optimizing communication protocols [56]. Within these broad directions of effort, one of the simplest and most effective schemes to reduce the power consumption is to favor inactive or sleep states as much as possible, thus decreasing the activity level of the devices within a network. This is critical for many applications, in particular when it comes to IoT devices.

  One of the primary methods of reducing the activity level in WLAN devices is to integrate a wake-up radio (WuR) with the power hungry WM. However, this approach is susceptible to many false wake-ups. To improve asynchronous node operation and avoid false wake-ups, PASS can be incorporated to create an augmented WuR module that not only discriminates incoming signals by RF energy content, but also identifies key characteristics of wireless data transmission at very low-power. For example, managing

WM responsibilities by identifying the modulation scheme, protocol, or packet type, without requiring any demodulation.

- Low-Power WLAN IoT Networking: We see an additional opportunity to reduce power consumption for wireless networks of IoT devices through the development of a PASS-enabled state machine based IoT device. Consider the scenario where a WLAN network is deployed in a home to connect multiple binary tasked IoT devices (e.g. turn lights on or off, open or close the garage). For such devices, instead of demodulating the incoming packets to determine the executed task, a PASS-enabled state machine can be used to identify and trigger the IoT devices at lower power. Additionally, with appropriately trained ML algorithms, PASS can provide optimized transceiver parameter configurations and efficient data transfers by restructuring a protocol to take advantage of the information embedded within the enveloped signal.

2.8 Conclusion and Discussion

In this paper we presented Packet Assay, a new technique to extract discriminating information from the envelope of WLAN packets' RF signals. Using a sparse NN we demonstrated that key features, such as packet type or protocol, can be classified with above 88% accuracy. With PASS we have taken the first step in applying ML techniques to create new opportunities in improving the power consumption and performance of WLANs, particularly targeting IoT systems. Nevertheless we highlight several future research directions for PASS,

- Improving Model Performance: While the CNN deployed here was both sparse and accurate, evaluating the applicability of tree based [57] and k-nearest neighbor [58] models on the dataset could provide improvements in sparsity and size. Additionally, targeting cross-misclassifications centered around the Beacon, QoS Data, and Data packet type clusters by employing boosting methods should improve accuracy further.

- In-Depth Packet Characterization: We have demonstrated that with PASS we can successfully classify 802.11b/g/n protocols and nine different packet types. If the model

can classify more in-depth packet characteristics such as device address ranges, then it's possible that the WLAN module would not need to be powered for certain scenarios at all. For instance, if the device is expecting to receive an ACK and PASS can accurately classify protocol, packet, and device address, then all necessary information has already been retrieved.

- End-to-End System Deployment: While not demonstrated in this paper, implementing PASS in hardware and integrating with WLAN chipsets is a promising research area to explore. This would demonstrate the feasibility of using NNs on chip and identify what key constraints exist in enabling PASS. For instance, microprocessor memory and ADC resolution would have a direct impact on the CNN classifier accuracy. Another challenge would involve maintaining the receiver sensitivity within a low-power device network.

Chapter 3

WIRELESS POWER AND COMMUNICATION FOR IMPLANTED ELECTRONICS

3.1 Introduction

The U.S. National Academy of Engineering (NAE) and the American Institute for Biological and Medical Engineering have identified the development of personalized, networked healthcare as a critical goal for improving equity in the United States [59]. Of the many types of disorders that could benefit from personalized medicine, neurological disorders are of particular interest given the essential role of the nervous system in movement and cognition. With many unknowns remaining about both healthy and pathological states in the nervous system, the NAE emphasized *reverse engineering the brain* as a key step towards achieving this goal. Developing translational medical therapies for neural disorders could have a profound impact on improving economic and social opportunity for all people, but doing so will require the seamless integration of devices with the brain.

Emerging bioelectronic medical devices, such as the brain-computer interfaces (BCIs) shown conceptually in Fig. 3.1a, provide new treatment options for sensorimotor and cognitive disorders. By measuring neural signals in the brain and/or spinal cord, these systems can analyze patterns in the dynamics of neuronal activity and generate control signals for therapeutic or assistive devices that can improve quality of life (Fig. 3.2). For example, early clinical trials on spinal cord stimulation have partly restored motor function after spinal cord injury [62, 63], and deep brain stimulators have helped alleviate symptoms from obsessive compulsive disorder [64]. Despite these successes, the electrophysiological mechanisms behind the treatments remain poorly understood. Current bioelectronic devices remain invasive and unwieldy, creating a barrier to real-time, closed-loop monitoring of the electrophysiological markers involved in the stabilization and regeneration of neural pathways. This gap

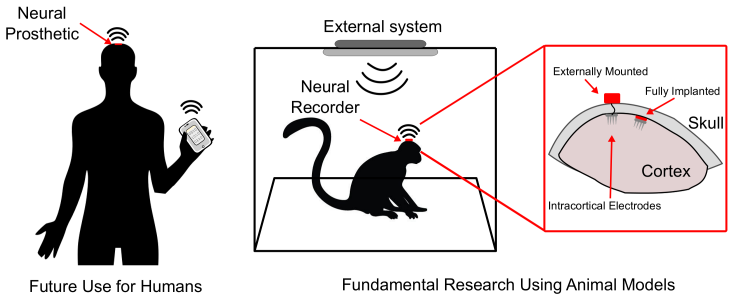

(a)

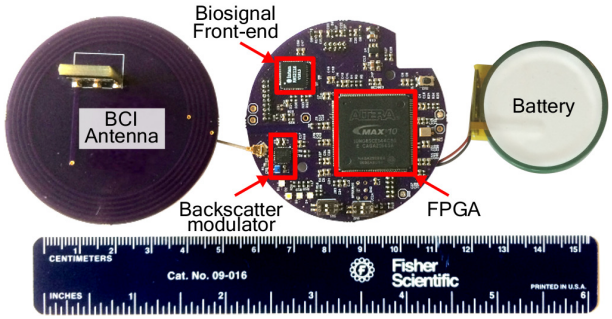

(b)

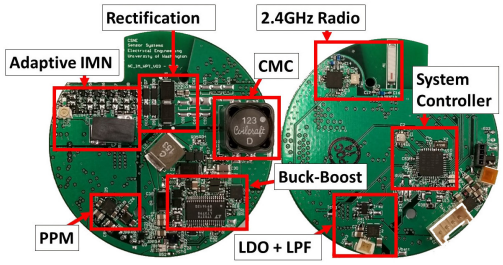

(c)

Figure 3.1: (a) Depiction of wireless neural recording applications for healthcare in humans (left) and fundamental neuroscience research in animal models (right). (b) *NeuroDisc* - a wireless neural recorder for use with non-human primates. The system was designed as an externally mounted neural recorder, though the results from this research are applicable to future implantable, battery-free wireless neural recorders. (c) *Adaptive Impedance Matching WPT Receiver (AIMWPT-RX)* - adaptively matches the BCI Antenna load, rectifies the HF input, and regulates the supply power for running noise sensitive electronic devices.

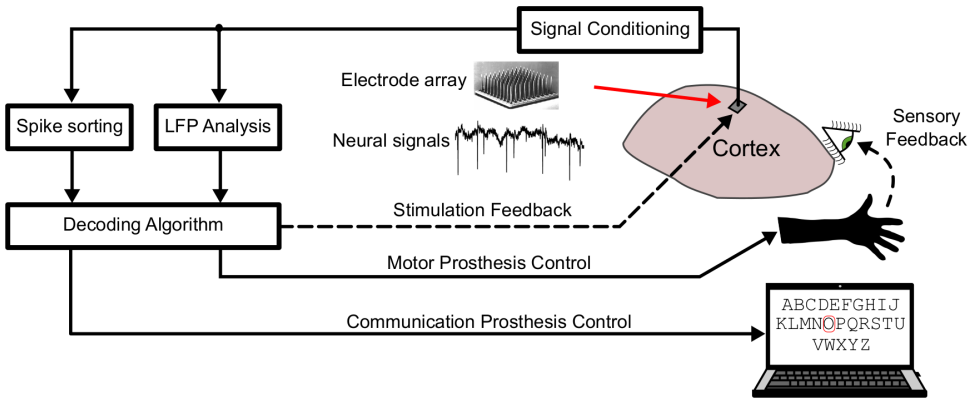

(a)

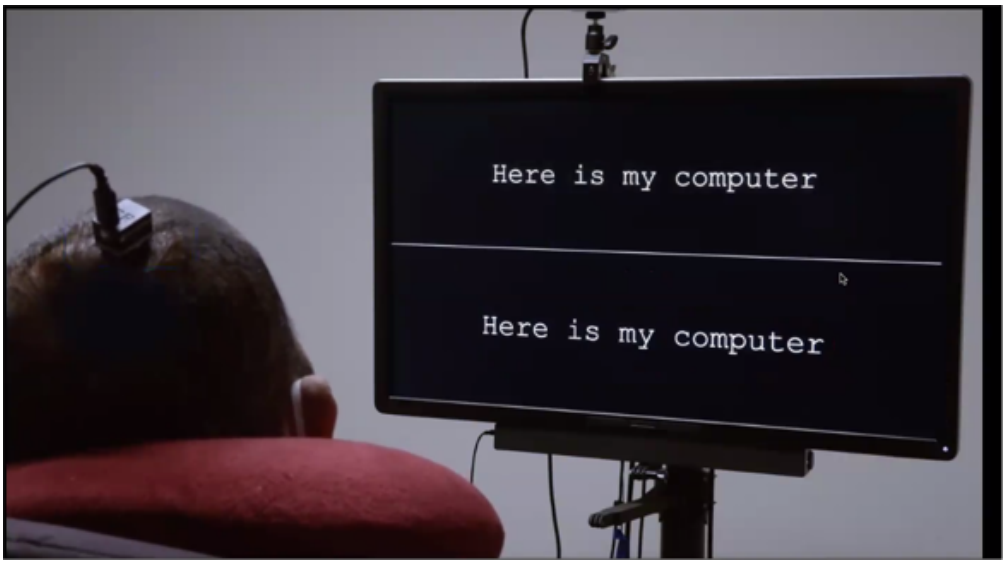

(b)

Figure 3.2: Brain-computer interfaces (BCIs) measure and process neural signals: (a) Generalized architecture for neural prosthetics (adapted from [60]). (b) BCI enabling a patient with locked-in syndrome to write sentences based on neural activity [61].

has led to global efforts by the European Commission [65] and the U.S. Defense Advanced Research Projects Agency (DARPA) [66] calling for new devices that can aid in seamlessly diagnosing and monitoring brain function.

For neurotechnology to be integrated with the brain, the size, weight, and power (SWaP) of the electronics must be minimized while controlling for safe *in vivo* operation. Neural recording systems are currently limited by their biocompatibility with surrounding tissue and their severely constrained power budgets, which must deliver complex electronic functionality with a milliwatt-scale power budget to avoid damaging tissue [67, 68]. As a result of these challenges, current real-time neural prosthetics typically operate with tethered instrumentation in constrained environments [61, 69] (Fig. 3.2). These tethered interfaces facilitate the transfer of power and data to external systems that can decode the neural signals to study brain dynamics, actuate external prostheses, and/or deliver neural stimulation. However, tethers also reduce mobility, increase the risk of infection, and can produce misleading correlations in the recorded data [70]. Coupled resonator Wireless Power Transfer and wireless data uplinks eliminate the need for tethers, but the high power consumption of conventional wireless devices (e.g. Wi-Fi) or microcontroller based preprocessing renders them incompatible with the SWaP constraints of implanted devices. As a result, state-of-the-art systems have heretofore been limited by shorter operational durations, reduced uplink throughput [71], or elimination of a real-time wireless uplink [70].

Implementing long duration operation of with either high rate wireless communication or complex onboard preprocessing within the constraints of a neural prosthetic remains challenging. Most proficient consumer wireless devices, like smartphones and laptops, are designed under drastically different size, weight, and power (SWaP) constraints. Smartphones, for example, are required to transmit cellular data, connect to WiFi, and perform complex processing for 8-10 hours before they are recharged and set aside for the night. To carry out these functions, phones can be on the order of 100 cm^3 while carrying a nearly 7 Watt-hour battery that occupies nearly two-thirds of the phone's volume, which then need to be recharged by cumbersome directly connected or surface adjacent power transmitters. In

contrast, an implanted neural prosthetic providing stimulation for induced plasticity would need to be on the order of 1 cm^3 and stream comparable amounts of data non-stop, day and night, ideally for multiple days or weeks. The size and weight of the implant must be minimized and fully encapsulated to reduce a patient's foreign body response, and the power consumption must be kept to <10 mW/cm^2 to reduce the risk of damaging nearby tissues [72, 73]. Even in the multi-billion dollar industry of cellphones, where SWaP is critical, the integrated circuits (chipsets) for Wi-Fi and LTE radios are still on the order of 1 cm^2 in area and each may consume nearly 1 W of peak power –drastically exceeding the safe SWaP and thermal envelope. Additionally, even when recharging these devices wirelessly at the rates necessitated to fill 7 Watt-hour batteries in short periods of time (5-15W), the receiving coil is limited to a static position within 5 mm of the wireless charging transmitting coil [74].

Backscatter communication provides an alternative to the high power consumption and large size of conventional wireless uplinks. Backscatter radios offer megabit per second (Mbps) data rates while consuming microwatts of power, yielding per-bit energy efficiencies on the order of pJ/bit, a 50-1000X improvement versus conventional radios [75]. Backscatter communication achieves significant energy savings by reflecting an externally generated radio frequency (RF) carrier wave carrier wave to transmit data rather than generating the RF carrier wave locally. The power-hungry RF carrier wave generator and RF amplifier can thus be removed from the energy constrained device, as shown in Fig. 3.3, and instead allocated to an external system with a less constrained power budget. By changing the impedance presented to its antenna, for example using an RF switch, a backscatter-based device can deliberately reflect electromagnetic waves while modulating the amplitude and phase of the waves. These reflected waves can then be received and decoded using conventional radio technology. The energy savings of backscatter communication have enabled novel wireless sensing modalities. For example, backscatter communication has been used to telemeter neural data from dragonflies in flight using a battery-free neural recorder [76] and to enable a battery-free wireless camera [77].

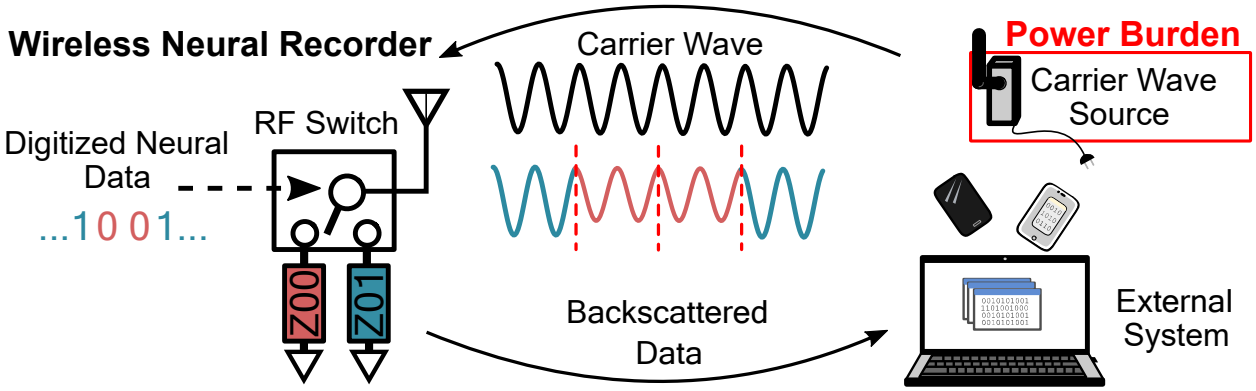

Figure 3.3: Overview of backscatter communication. The power burden of carrier wave generation and amplification is removed from the energy-constrained neural recording device.

By then pairing these power savings with adaptive coupled resonator WPT, the neural prosthetic can perpetually cycle through short charging and long operational phases without significant interruption. At a given received power, coupled resonator WPT allows for a 10-100x improvement in efficiency compared to far-field or non-resonant modalities with less dependence on receiver orientation with respect to the transmitter [4]. This power transfer efficiency can then be traded off for expanding the separation between the transmitter and receiver and coil alignment while still keeping the transmitted power low. Additionally, by relying on the magnetic field to transfer power near or within biological tissue, which has low permeability [31], magnetic resonant WPT induces less SAR heating than methods relying on the electric field to deliver the same amount of power [78].

These benefits make the combination of backscatter communication and coupled resonator WPT an appealing choice for research and clinical applications.

3.2 Neural Prosthetic Technologies

Neural prosthetics are emerging thanks to decades of advancements in methods for *in vitro* and *in vivo* neural recording. Examples of neural measurement techniques include electrophysiological recording to measure electrical signals generated by neurons [79], two-photon microscopy to measure cellular structures labelled with fluorescent proteins [80], and functional magnetic resonance imaging (f-MRI) to measure blood flow throughout the brain

[81]. Each measurement technique has trade-offs in spatial resolution, temporal resolution, invasiveness, and portability [82]. Electrophysiological recording is a promising method for neural prosthetics given its very high temporal and spatial resolution. Furthermore, thanks to existing industrial processes for manufacturing silicon devices, electrophysiological recording lends itself to miniaturization, high volume manufacturing, and low cost.

Within the modality of electrophysiological recording, several techniques exist. These techniques focus on measuring the electric fields generated by ionic channels in neurons during action potentials (APs) or "spikes." By placing a conductive probe within or near a neuron and measuring the potential relative to a reference electrode, high fidelity signals representing neural activity can be obtained. Alternatively, the electric field from groups of neurons, known as neural ensemble activity, is strong enough that it can also be measured by electrodes on the surface of the brain (electrocorticogrpahy or ECoG) or on the surface of the scalp (electroencephalography or EEG). Generally the spatial resolution is commensurate to the invasiveness of the technique, with intracortical and ECoG electrodes providing high resolution but requiring craniotomies and EEG providing lower resolution without the need for surgical implantation.

By measuring the temporal and spectral electrical activity of neurons, electrophysiological recordings have improved our understanding of neuronal dynamics [79]. Neural firing rate can be decoded to the intended limb movement parameters [61, 69, 70, 83–85], enabling the development brain-computer interfaces (BCIs) that operate prostheses based on neuronal firing rates and neural ensemble activity, as shown in Fig. 3.2. These BCIs can provide assistance to people with sensorimotor disorders like paralysis [86, 87], Parkinson's [88], ALS [61], as well as cognitive disorders like obsessive compulsive disorder (OCD) [64]. Improving the performance of such devices has thus become an active area of research in academia and industry [89].

In order to measure neural dynamics with high temporal and spatial resolution, neural interfaces need to transmit large volumes of data. A complete action potential typically lasts 1 msec, and in order to measure the complete depolarization and repolarization dynamics,

sample rates $\geq$ 20 kHz per neural channel are needed. When measured outside of a neuron, the AP amplitudes can be on the order of 10's of μVolts, typically requiring analog-to-digital converter (ADC) resolutions $\geq$10 bits, e.g. [90]. While theoretically the firing rate of a single neuron could be used to control a one-dimensional BCI, decoded signals from multiple neurons are required to control higher complexity systems, like robotic arms. Recording from multiple sites in the brain is also advantageous for fundamental neuroscience to analyze how different areas of the brain exchange information.

If we consider collecting 32 channels of neural data with 16-bit voltage resolution and a sampling rate of 20 kSamples/sec (kSps) per channel, the total biological data volume is more than 10 Mbits/sec (Mbps), which can easily grow to more than 20 Mbps with the addition of data packet structure, error correction coding, and housekeeping information such as timestamps. Data compression techniques can be used to reduce the required data rate, however, the required algorithms pose additional constraints in computational time and a trade off between operational time and charging time, due to the additional power consumption encumbrance.

Since it is difficult to achieve wireless data rates >2 Mbps using commercial off-the-shelf electronics while remaining within the necessary SWaP envelope, electrophysiology experiments often rely on controlled, cabled test environments where a subject's movements are constrained. Systematic control of the test environment reduces noise in neural recordings, enables precise measurement of the behavioral tasks, and prevents injury to the person or animal and damage to the wired equipment. There are several drawbacks to cabled setups, however. First, cables are a vector for infection of surrounding tissue. The cable must pass through the skin and the protective dura mater of the brain, leaving the subject vulnerable to bacterial infections. Secondly, a cable requires mechanical stabilization to avoid injuring the subject and damaging the measurement equipment. Mechanical stabilization is often achieved by restricting the subject's movement, which causes stress and discomfort for the subject. Under these conditions, a subject can only be expected to perform tasks for a limited amount of time before physical and mental fatigue degrade their performance. Ad-

ditionally, restricting motor function has been found to affect the quality of the measured neural data. Unnatural correlations between motor parameters and neural signals, referred to as stereotypes, have been observed during constrained experiments [70], making it difficult to generalize findings. Ultimately, humans and animals live and thrive in a natural and freely moving state. In order to develop an unbiased understanding of how neural activity gives rise to high-level functionality over long durations, neural recording must be performed wirelessly.

To reduce the effects of tethers, dozens of wireless BCIs have been developed for wireless neural recording in free-moving animals, e.g. [91–94] as recent examples of the state-of-the-art. Researchers at the University of Washington in [91] developed a wireless BCI called the NeuroChip-2 for recording and stimulation in NHPs. While this device can be used for neural recording experiments of nearly 48 hours duration, the potential for recording neural data for >48 hours is limited because data must be saved locally to an SD card; there is no high-rate wireless uplink to offload data, so once the memory is full, the experiment must be terminated. Further, SD cards require more than 600 mW of power during write and read operations [95], which can easily dominate the power budget of the BCI, and their size and user interface restrict prohibit their use in fully implantable devices. Other wireless BCIs use Wi-Fi [96], BLE [94], or custom wireless protocols on integrated circuits [92] to uplink data, but the power budget of these BCIs is still dominated by the communication system. These conventional radios have undesirably high power consumption, which leads to poor battery life and the potential for tissue heating due to the combination of DC power dissipation and high specific absorption rates (SAR) [97, 98].

To provide for long duration operation of these wireless neural recording devices in free-moving animals multiple cage based WPT systems have been developed. For low-power neural recording devices mounted to small animals significant effort has been put into developing WPT capable cages using overlapping arrays [99–103] or cavity resonator based charging [104]. These systems are predominantly designed towards rodent homecage dimensions (20×23×45cm) and intend to provide ¡100mW power at <60% power transfer

efficiency. More recently, Animal Body Communication has been used to provide <50mW through conductive contact with the cage floor [105]. However, these systems will not provide the power required to recharge the batteries that would be needed for larger, non-stationary animals, such as NHP. Standard NHP cages built of stainless steel for mechanical security and longevity form a reverberant cavity for UHF bands, resulting in dense multipath within the cage and deep nulls occurring only a few cm apart [106]. To address this group, custom non-conductive cages [107,108] have been developed to allow unimpeded recharge of wireless devices. This custom solution though would be difficult to integrate with current NHP lab hardware.

3.2.1 Backscatter Communication for High Rate, Energy Efficient Telemetry

Energy efficient, high data rate wireless backscatter communication could solve the complex SWaP tradeoffs of neural recorders. These uplinks could provide the data to an external, non-power-constrained computing device to analyze the recorded neural activity, as shown in Fig. 3.1a. For the case of bi-directional BCIs that provide neural recording and neural stimulation, such an external device could also determine a stimulation response using signal processing techniques that are infeasible on a size- and power-constrained neural recording device [73].

Backscatter communication achieves high energy efficiency by redistributing power-hungry elements in a wireless link to a power-rich external system. Unlike conventional radios, backscatter-based uplinks do not require RF amplifiers and oscillators to generate a communication carrier wave. The carrier wave is instead provided by an external transceiver having access to e.g. mains power or a large external battery. As shown in Fig 3.3, a backscatter-based device can communicate data by applying a time-varying impedance to its antenna, which modulates the amplitude and phase of the incident carrier wave. In this case, the backscatter-based device only needs to provide enough power to actuate an RF switch or transistor, which is typically consumes microwatts rather than milliwatts. The modulated signal is then scattered by the device's antenna and received by an external system that

could be a custom receiver or a commodity device, depending on the frequencies used, the modulation scheme, and the protocol. This modality allows for small-form factor systems with high data rates (>96 Mbps) [109] at orders of magnitude lower power consumption compared to BLE and WiFi (IEEE 802.11n) [110]. Technology such as ultra-wide band (UWB) radio [111] is a potential alternative to backscatter communication, but backscatter communication is an attractive choice for BCIs due to its simplicity and lower overall power consumption compared with UWB and other alternatives. Furthermore, backscatter has the potential for compatibility with existing protocols like WiFi and Bluetooth, reducing the overall cost and complexity of the system.

The improved energy efficiency of backscatter communication comes at the cost of a less favorable link budget compared to conventional radios. Because the externally-generated carrier wave travels a round trip from the external system to the backscatter radio and back, the RF path loss changes as $1/r^4$ for a backscatter system, rather than the usual $1/r^2$ for conventional radios, where r is the free-space distance between the external system and the BCI antenna [112, 113]. Given the round-trip nature of the backscatter link budget, multipath interference can significantly reduce the reliability of backscatter radios. For experiments conducted inside the cage of a freely moving animal, the multipath environment could result in dropped data. Careful attention to the communication channel and the link budget design are therefore required to ensure reliable communication.

3.2.2 The NeuroDisc Wireless Neural Recorder

An example of a wirelessly-charged, backscatter-based brain-computer interface device is the *NeuroDisc*, which leverages a backscatter communication uplink to attain high data rates while expending orders of magnitude lower power consumption relative to commercial wireless standards. The NeuroDisc is a wireless neural recording tool for researchers that uniquely synthesizes previous advancements in low-power backscatter communication and biological sensing to reduce the power burden of wireless uplinks on neural recorders.

What differentiates the NeuroDisc from other wireless neural recorders is an FGPA-based

reconfigurable backscatter uplink that enables the use of several different ultra-low-power communication modes from a single hardware platform: a 25 Mbps differential quadrature phase-shift keying (DQPSK) uplink using a custom protocol [75] can transmit large volumes of data, as needed for broadband neural recording; a single-sideband (SSB) BLE compatible frequency-shift keying (FSK) uplink [114, 115] that facilitates integration of the NeuroDisc with existing wireless infrastructure; and an orthogonal frequency division multiplex (OFDM) backscatter uplink [116] that enables greater resilience to multipath fading observed in animal cage environments. To measure neural signals, the NeuroDisc uses a low-power Intan RHS2116 electrophysiology interface that can sample 16 channels at 20 kSps with 16-bit resolution, allowing recording and uplink of low frequency local field potentials and high frequency neural spikes [117]. The RHS2116 also provides stimulation capability, enabling the NeuroDisc to eventually be used for both neural recording and stimulation experiments. A comparison of state-of-the-art neural recorders including the NeuroDisc is shown in Table 3.1 and a comparison of wireless uplink efficiencies between backscatter and conventional wireless devices in Fig. 3.4.

3.2.3 Coupled Resonator Wireless Power Transfer for Safe, High Power, Long-range Recharging

High power, long-range, high efficiency coupled resonator WPT [122] can allow for perpetual, safe operation of neural recorders up to the battery's cycle count limit. Mobile systems employing coupled resonator WPT provide for safer operation by not only by removing cables that provide a vector for infection to biological tissue, but they also avoid sparking hazards between cable interconnects and allow for full encapsulation, thereby sealing off threats to biological tissue. Additionally, from a long-term reliability perspective the connectors and headers associated with tethered operation are the most failure prone source for many electronics systems.

WPT to low power mobile electronic devices (<1W) within constrained application spaces can achieve end-to-end efficiencies approaching 80% [123]. This high power transfer efficiency

Table 3.1: Comparison of state-of-the-art wireless neural recorders

	Yin et al., 2014 [92]	***Schwarz et al., 2014 [118]***	***Muller et al., 2015 [93]***	***Ando et al., 2016 [119]***	***Teng et al., 2017 [120]***	***Xu et al., 2018 [121]***	***This work, NeuroDisc [75, 115, 116]***
Test Subject	NHP	NHP	Rat	Humans	-[a]	Rat	**NHP**
Custom ASIC	✓	✗	✓	✓	✓	✓	✗
BCI Size (mm)	52 x 44 x 30	-[a]	6.4 x 6.4 x 0.7 (IC)	53 x 31 x 47 (Transmitter)	1 x 1 (IC)	2.5 x 5.3 (IC)	**63 x 63 x 30**
ADC (bits)	12	12	15	12	-[a]	12	**16**
No. of Channels	100	512	64	4096	8	12	**Up to 16**
Sampling (kSps)	20	31	1	1	-[a]	40	**Up to 20**
Stimulation Capability	No	No	No	No	No	No	**Yes**
RF Comms Type	Active RF	Active RF	ASK Backscatter	Active RF	Active RF	Active RF	**DQPSK, SSB FSK, or OFDM Backscatter**
RF Comms Band	3.5 GHz	2.4 GHz	300 MHz	9 GHz	403 MHz	2.4 GHz	**915 MHz & 2.4 GHz**
Wireless Data Rate (Mbps)	48	1.33	1	128	8	10	**Up to 25**
Uplink Distance (m)	5	10	0.013	5	-[a]	-[a]	**Up to 6**[c]
Analog Comms Power (mW)	>30[a]	33.9[b]	0.0024	561	5.6	396	**≤0.309**[d]
Analog Comms Energy Efficiency (pJ/bit)	>180 (high-rate mode) - 750 (low rate mode)[a]	25,488	2.4	4383	700	39,600	**12.4-198**[e]

[a]Exact value not reported. [b]TX power consumption of the nRF24L01+ at 0 dBm transmit power.
[c]SSB FSK modulation at 1 Mbps data rate in the 2.4 GHz ISM band.
[d] Measured static+dynamic power of the backscatter modulator for DQPSK modulation at 25 Mbps.
[e]12.4 pJ/bit for DQPSK modulation at 2 Mbps. 160 pJ/bit for SSB OFDM modulation at 1.25 Mbps. 198 pJ/bit for SSB FSK modulation at 1.0 Mbps.

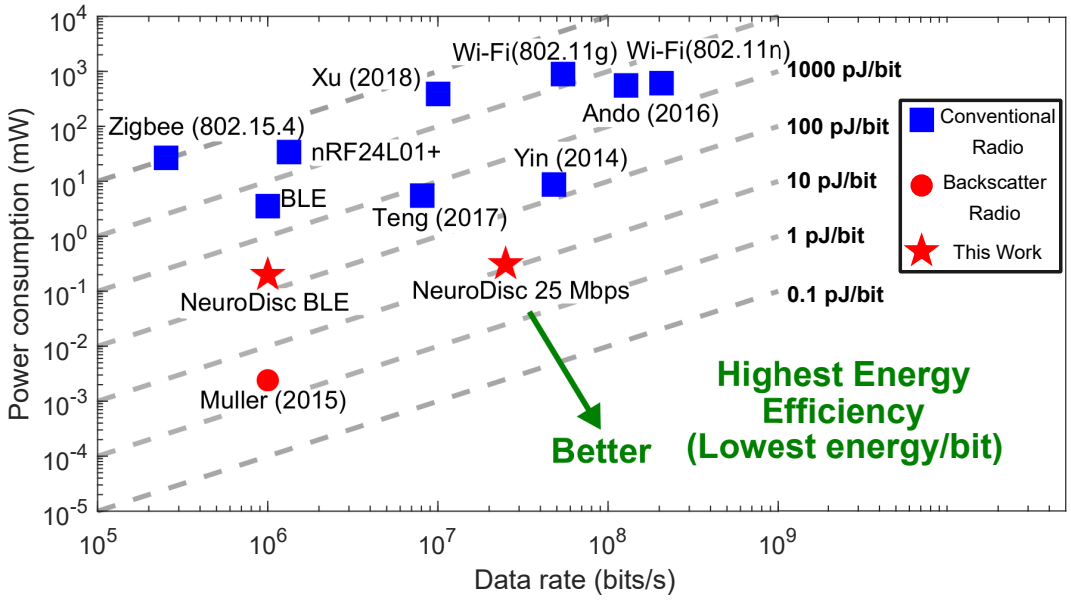

Figure 3.4: Comparison of the wireless uplink efficiency of state-of-the-art wireless neural recorders and common wireless standards.

(PTE) is traditionally obtained through an impedance matching network (IMN) tuned at the resonant frequency to match the chosen base station (TXBS) switching amplifier (Class D or E are common) output impedance to the transmitting resonator (TX) and then a second IMN matching the receiving resonator (RX) to the mobile device load (RXML). The mutual coupling between the TX and RX then require concurrent IMN tuning in order to achieve optimum PTE.

Expanding the application space by increasing separation, orientation, or alignment of the resonators; changing the switching amplifier's output impedance; or varying the device load can reduce the PTE for a previously optimal set of IMNs. Up to EMI and SAR limitations on field strength [124] and within the stable operation of the switching amplifier, with closed-loop control between the TXBS and RXML the output power can be scaled to compensate for the PTE loss. Alternatively, to maintain high PTE in this expanded application space either the operating frequency to maximize PTE can be tuned [122, 125] or the IMNs can be adaptively controlled [126, 127]. Tuning the operating frequency may exceed operational

bandwidths dictated by wireless communication standards in a given country, especially within medical environments, so Adaptive Impedance Matched WPT (AIMWPT) setups are preferable.

While efficient end-to-end power transmission is readily achievable by AIMWPT systems, applying this modality to neural recording devices presents unique difficulties. Firstly, the American Association of Medical Instrumentation limits chronic temperature increases in the tissue to less than 2°C [128]. In high power transfer scenarios, inefficient power regulation or system operation in the RXML can lead to high heat conduction and radiation temperature increases in the surrounding tissue that exceed this limit. Secondly, in the same high power transfer scenarios, in addition to the EMI resulting from the inductive field itself, the rectification of the HF input in the RXML can lead to significant noise on the DC power plane. While many consumer electronic devices have a PSRR that can dampen this noise to operable levels, neural recording devices can have their recordings corrupted due to the high sensitivity of the AFE. A closed-loop controller onboard the RXML and careful circuit design can best address these issues.

3.2.4 The Adaptive Impedance Resonant Wireless Power Transfer Receiver

To perpetually power and control the *NeuroDisc* or *NC3* and backscatter communication platform over long distances within caged environments allowing for freely moving large animals, specifically NHPs, the *Adaptive Impedance Resonant Wireless Power Transfer Receiver (AIMWPT-RX)* was developed, Fig. 3.1c. While AIMPT-RX was developed with these specific interfaces and form-factor in mind, the power supply can be utilized by many combinations of recording and communication devices where the ratio of low noise operation to charging time decreasing as the power requirements of the dependent devices increases.

The usage model for the AIMWPT-RX, Fig. 3.5a, is that a TX resonator is positioned in the non-human primate cage at a location above the NHP's perch, where the NHP rests. The TX resonator is driven by a Wibotic WRELv2 Transmitter [129]. While the NHP is in this position, the encapsulated system's battery is wirelessly recharged. The recharging via a

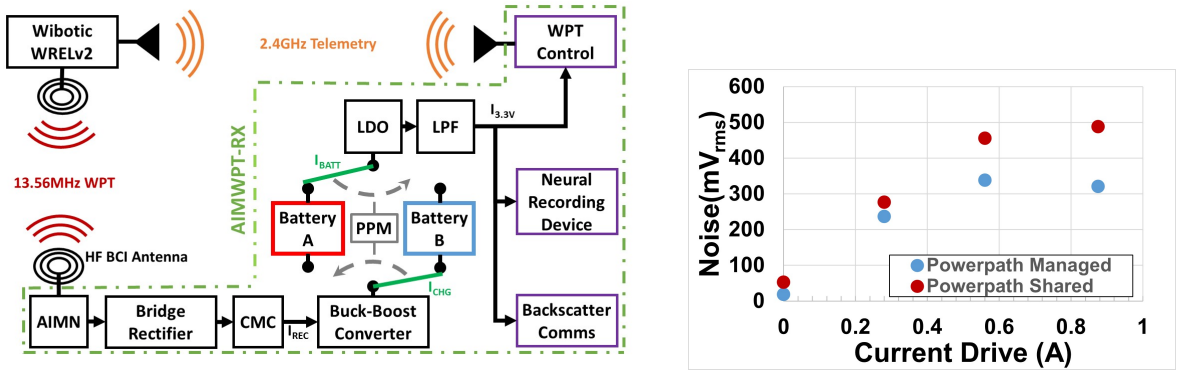

(a) (b)

Figure 3.5: (a) WPT System Block Diagram showing Wibotic WRELv2 Transmitter, which provides both power at 13.56MHz and bi-directional telemetry at 2.4GHz, and the AIMWPT-RX, which adaptively matches the input impedance and conditions the input power to produce a low noise 3.3V power supply for the dependent noise sensitive devices. (b) At high charging rates, the inclusion of powerpath management decreases the conductive interference on the power plane by 35.4%.

charging controller implemented on the MSP430 microcontroller should be completed in the minimum time possible so as to constrain the NHP's movement less. In order to maintain safe operating conditions during this time, if heat or humidity within the enclosure exceeds set limits, then the charging cycle adapts by lowering the charging current via a 2.4GHz radio connection with the WRELv2 or shutting the combined system down completely if there is an emergency.

To better understand the limitations of WPT within a cage environment, the field between a HF biased-repeater BCI antenna RX [130], with an outer diameter of 5.5cm, and a 6-turn biased repeater TX, with an outer diameter of 13.35cm and mounted to the back-left ceiling of the cage with a durable plexiglass sheet, was characterized within the 2 Compartment Primate Unit cage [131]. The walls of the cage are predominantly constructed with square metal mesh with a mean grid size of 2.5 cm, which is 88x smaller than the shortest wavelength of the HF band ($\lambda \approx 220cm$). While a poly-carbonate window 23.4 x 60.7cm is positioned

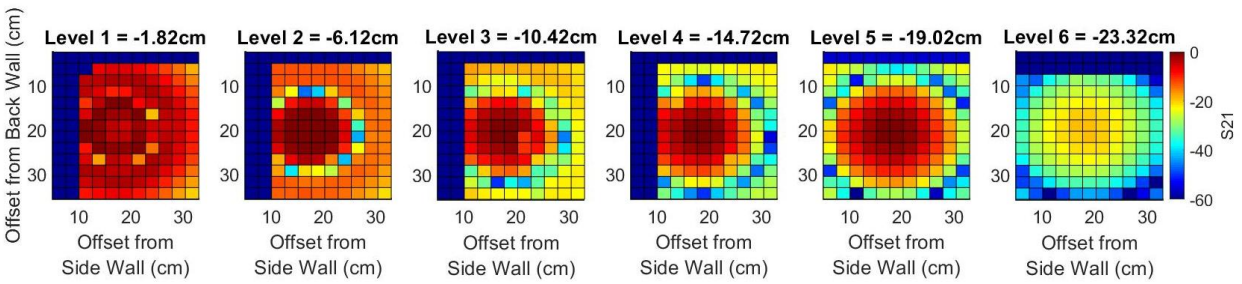

Figure 3.6: The HF S21 field characterization between a TX mounted to the back-left ceiling of the cage and a mobile HF BCI Antenna. The dark blue contiguous runs were locations where the antenna could not be positioned.

towards the front of the cage, the center of that window is positioned well beyond the point where there is still substantial field strength. As such, the walls of the cage act as an enclosed Faraday Cage. The BCI antenna was IMN tuned to 13.56MHz within freespace and the TX coil IMN was tuned to 13.56MHz with the TX 1cm offset from a metal sheet of equivalent size to the cage's ceiling. The S21 was measured using a Keysight P9375A VNA throughout the upper-left-back eighth of the cage, in the region where a NHP could be trained to rest for the long durations required for charging, Fig. 3.6. The WRELv2, is limited to 250W output, and the receiver requires approximately 5W to charge the 3.7V battery at a max rate of 1A. For maximum charging capacity then the HF receiver must be within the region where the S21 must be greater than -17dB. Thus, for reliable charging, the BCI antenna must be positioned within the 23.32cm of the ceiling of the cage and no more than 32cm from either wall. For the cages used in this work, when a NHP rests on its perch, that puts the BCI Antenna well within the field.

While the NC3 recordings and NeuroDisc operation are disturbed by the EMF produced by the TX and RX coils, the packages can be encapsulated within shielding such that the effect of the emitted fields is reduced to the point where 10uVpp signals can be readily recorded and transmitted. To confirm the benefit of shielding, experiments to characterize and mitigate the effects of wireless interference on the neural recording. With the NC3 within a Faraday Cage and no conductive path between the NC3 and the AIMWPT-RX,

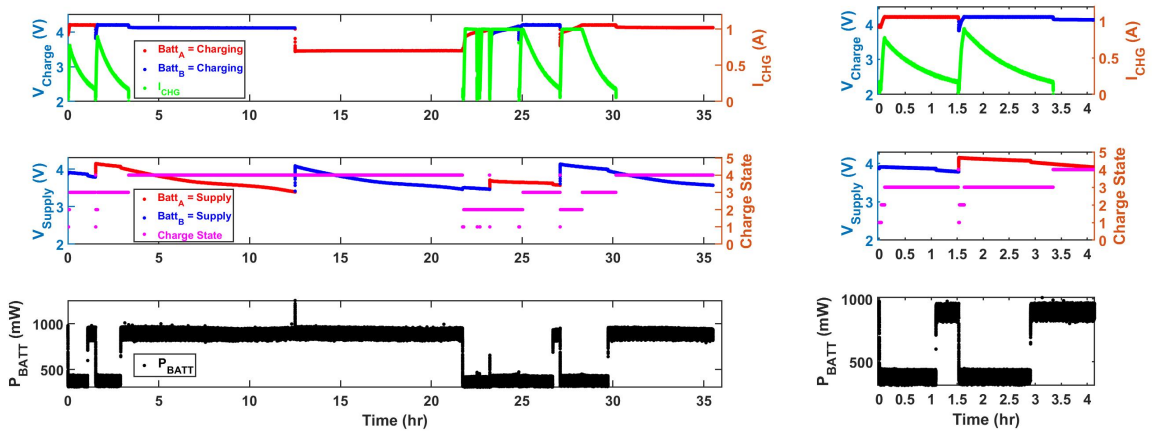

Figure 3.7: (a) A 35hr run of the system demonstrating the possibility of perpetual charging and low noise operation via time-multiplexing between the charging and recording periods. (b) Zooming in on the first 4hrs of operation to demonstrate the ping-pong charging provided by the powerpath manager. The charging states 1-4 (represented by the height of the magenta trace) correspond Precharge, Constant Current, Constant Voltage, and Standby states, respectively. States 0 and 5 correspond to error conditions, which weren't met during this run.

the SNR was unaffected by the WPT field. While promising, to enable perpetual charging the neural recorder still needs to be connected to the power supplied by the RX. Through that connection, at charging rates above 1W conducted interference completely corrupted the neural recording and backscatter communication PER approached 100%.

To reduce the conducted interference the AIMWPT-RX, Fig. 3.1c, was created with a Common-mode Choke on the rectified input and a Powerpath Manager (PPM) was instituted to allow one 3.7V Li-ion battery to be charged while the second battery, after being regulated by an LDO, provides a 3rd Order and Ferrite Low-pass filtered 3.3V to power the NC3 and backscatter communication device operation Fig. 3.5a. This ping-pong charging operation can be seen in more detail in Fig. 3.7b, a zoomed in version of the longer charging period shown in Fig. 3.7a. The AIMWPT-RX controller begins by checking each battery if it is

fully charged. In this example, the controller found both batteries needed to be topped up. The PPM connects Battery A to the LT3790 Buck-Boost regulator for charging and Battery B to the LDO which then supplies a filtered 3.3VDC to the WPT Control circuitry. If the system is operating in a low conductive interference state, i.e. a charging rate below 1W, then the communication and neural recording devices are powered, otherwise they remain off. The controller then steps Battery A through 4 charging states. Referring to the middle plot, Battery A starts in a Charge State 1 Precharge, where first the health of the battery is ascertained, then 100mA is driven into the battery and the Adaptive IMN (AIMN) checks for an impedance match that improves the PTE. Once completed, the controller enters Charge State 2 (Constant Current) and ramps up the charging current to the recommended battery charging rate (875mA) and dwells at this level until the voltage on Battery A reaches the max cell voltage (4.2V). In the top plot, the charging ramp is shown in green and took 6min. Once this limit is reached, Battery A is then switched into Charge State 3 - Constant Voltage and the current delivered to the battery is ramped down gradually while maintaining the max voltage on the cell. Again in the top plot the ramping down of the current took around 1hr 24min. Finally Battery A, being fully charged, enters Charge State 4 - Standby. Note that when the charging current dropped below 250mA, the system is operating in a low conductive interference state, so the controller powers up the neural recorder and backscatter communication systems. Next, as Battery B also requires topping-up, the PPM switches the charging and supply power paths. Battery B then proceeds through the same charge states until the battery is fully charged. Once both batteries are fully charged, the system remains in Standby until both batteries require charging again. This procedure allows for the charging of both batteries at fairly regular intervals, during which the NHP can be trained to rest within the WPT field. Lastly, around 22hrs into the recording, the system rapidly ping-pongs quicker than in the early stages, this is done to ensure that there is enough power available on the batteries to keep the WPT Controller running.

Even with the additional common and differential-mode filtering, at charging rates approaching 3.5W, the addition of the PPM alone reduced the noise on the power plane by

35.4%, Fig. 3.5b. This improvement enabled the backscatter communication with an average PER of 0.005% throughout the full range of charging rates, however noise on the power plane still severely degrades the SNR on the neural recorder at charging rates greater than 1W, approaching -30dB at the highest charging rate.

With the recording corruption in mind, in order to prioritize the transmission of high SNR data, the neural recording and backscatter communication are only powered during those times when the charging rate is less than 250mA (1W). This time-multiplexing confines the recording operation to the time period where at least one of the batteries has greater than 3.3V or while the system is operating in constant voltage mode and the charging current has declined below 250mA. This time multiplexing can be seen in the bottom-most plot of Fig. 3.7a, where the power is only delivered when the above conditions are met. With this time-multiplexed charging system operating, the WPT controller requiring 182mW, the backscatter communication requiring 228mW, and the NC3 requiring 548mW, the system can run 2.5hrs for every 1hr of charging, with a maximum continuous charge period of 19hrs, Fig. 3.7a.

Chapter 4

A LOW-COST, OPEN-SOURCED PLATFORM FOR HIGH-FIDELITY CHARACTERIZATION OF LARGE WPT COILS

4.1 Introduction

The use of efficient near-field wireless power transfer (WPT) using magnetic resonant coupling (MRC) is rapidly normalizing. This new charging paradigm provides immense benefits across a range of sectors, from low-power implanted medical devices, to mid-power wireless consumer electronics devoid of a single port, and extending to the high-power systems enabling wirelessly powered commuter busses. Each of these energy replenishment technologies are fundamentally dependent on the characteristics of the field created between the inductively coupled primary transmitting (TX) and secondary receiving (RX) coils. As such, characterizing the field that couples these coils is of paramount importance to real application of WPT advances.

WPT research has cleared initial validation and is aging into specialized applications. Measurements of field profiles required to pass maximum permissible exposure conservative checks have become standard operating procedure. This can lead to expensive prototype design testing at specialized facilities. Alternatively, abstracted and idealized models of power transmission have been supplemented by high-frequency simulations, such as those provided by ANSYS HFSS, for application to specific TX and RX setups. However, barring simplification to abstract away complex interactions between the environment and the interfacing coils, these simulations require immense computation time and eventually code validation for regulatory approval. Additionally, in applications where the coils are moving or arrayed within large 3D volumes with negligible permeable structures, let alone those volumes containing permeable or conductive structures, the computational complexity quickly exceeds

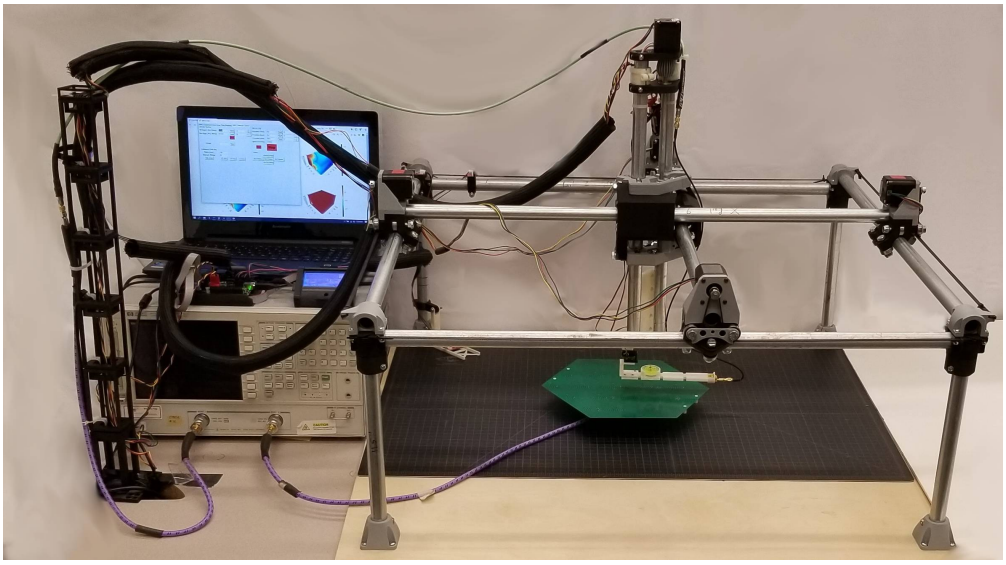

Figure 4.1: MPFCS with attached B-Field end effector characterizing complex relay resonator.

even high end servers.

To enable the rapid prototyping demanded by the next generation of WPT applications, we present the Mostly Printed Field Characterization System (MPFCS), Fig. 4.1: an inexpensive, open-sourced, easily assembled, high-fidelity with large-volume power transfer efficiency (S_{21}) and B-field characterization system built around the Mostly Printed Computer Numerical Control (MPCNC) platform from V1 Engineering [132] with end effector modifications to enable measurements from tilted and rotated RX. The system operation is demonstrated using two modes of operation: 2-port B-field volume characterization and a 2-port S-Parameter volume characterization. The tested system covers a volume of $(600 \times 600 \times 300)mm^3$ with a resolution less than 0.14mm, a tilt arc of 118° down to 1° resolution, and pan arc of 180° down to 1° of resolution. For movements of less than 10cm, the time per scan is less than 4.38s providing a significant improvement in field characterization rate by comparison to simulating the field at each point within a volume of interest.

Omitting the cost of the computer running the PC based controller and 2-port Vector Network Analyzer, the system as assembled and tested costs around 650USD, and with

a B-field probe addition approaches only 950USD. Costs are kept down from customized solutions [133] by using easily assembled off the shelf components wherever possible.

4.2 Materials and Methods

4.2.1 Mechanical Subsystem

The MPFCS can be broken down into three major mechanical subsystems: the MPCNC [132], the Z Tower Tilt/Pan Head (TPH) as the end effector, and a series of 3D Printed Mounts. The latest mechanical designs and implementation details can be found at https://www.thingiverse.com/thi

MPCNC

The MPCNC was developed as a low-cost, open-source CNC system with an expandable sweep volume. Alternatively, however, it can serve as a high-fidelity volume sweeping tool due to the precise three dimensional control over an end effector it provides. The Z Tower raises and lowers an attached TPH and end effector up to the implemented height, while the XY rails provide precision planar motion control of the suspended Z Tower. The constraining frame and mobile Z Tower are built from simple EMT Conduits, with the CAD files for the 3D printed joint piece provided for free online under a Creative Commons license.

The MPFCS has implemented the MPCNC with an EMT tubing frame that provides for a sweep volume of $(600 \times 600 \times 300) mm^3$ ([X, Y, Z]), which allows for coils centered within the volume with radii up to 212mm to have their realized field, up to their critical

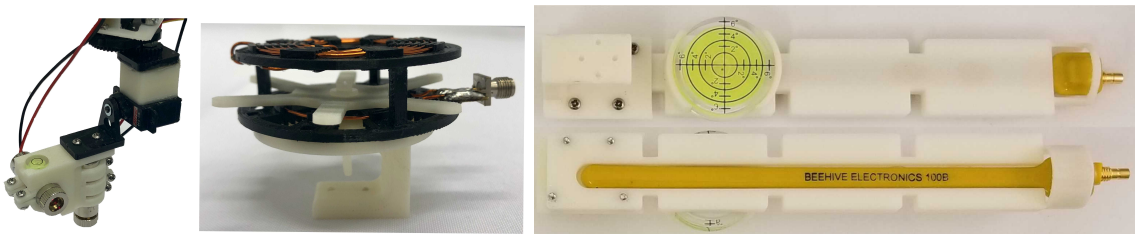

(a) (b) (c)

Figure 4.2: (a) Tilt/Pan Head with Mounted LED Laser Calibration Mount. (b) Universal Coil Mount with a coil mounted consisting of a 50mm spiral offset by 15mm from a 38.5mm loop. (c) B-field Characterization Mount with Beehive 100B mounted

coupling distance (CCD), characterized within the 300mm [134]. This space accommodates the characterization of even large, complex fields involving several arrayed coils and the use of large phantoms and substrate blocks to accommodate a variety of complex application environments.

Tilt/Pan Head

MPFCS substitutes the MPCNC's cutting head with a TPH and end effector, Fig. 4.2a. This provides the user the capability to tilt and pan (i.e. rotate about the Z Tower axis) the mobile coil under test (CUT), as demanded by the experiment. The TPH is operated by 2 servo motors (HITEC RCD USA, Inc.), which provide 118° tilt and 180° pan, with repeatable accuracy down ±0.5°.

Head Tool Mounts

Three probe and calibration end effectors are featured in this paper, each designed in Autodesk's Fusion 360 and subsequently 3D printed using ABS plastic.

LED Laser Calibration Mount This end effector, Fig. 4.2a, contains two lasers situated perpendicular to one-another for calibrating with respect to the X, Y, and Z axes movement, as well as the tilt and pan Fig. 4.2a. The two mounted, focusable, 5mW red dot LED lasers can be powered by batteries mounted to the Z Tower or by the RAMBo 1.4 directly. A bubble level mounted on the shelf holding the XY planar directed laser allows for zeroing out the tilt prior to calibrating the X, Y, and Z axes.

B-field Characterization Mount This end effector, Fig. 4.2c, is a cuboid with a hollowed out space for the Beehive 100B magnetic field probe [135]. When the 100B is mounted, the B-field of the CUT may be converted directly from the S_{21} measurements made by a connected vector network analyzer (VNA). The 100B probe offers high spatial resolution (loop diameter = 3.81mm) for converting S_{21} measurements to B-field measurements with calibrated accuracy up to 3.1GHz (4.1):

$$B = \frac{24547.1}{f_0} 10^{\frac{S_{21}}{20}} \tag{4.1}$$

where, f_0 is the test frequency and S_{21} is the power transferred to the Beehive 100B load from an immobile CUT at f_0.

Mobile Universal Coil Mount This head, Fig. 4.2b, provides secure attachment between the TPH and a mobile, suspended RX coil connected via cables routed along the Z Tower to one of two VNA ports. This allows for the characterization of the S_{21} within the volume swept by the mobile RX coil with respect to the immobile TX Coil.

4.2.2 Electronic Subsystem

The MPFCS uses the RepRap Arduino Mega-compatible Motherboard (RAMBo) 1.4 board as an integrated controller and driver solution for controlling the stepper motors directing the MPCNC XYZ movements, homing to XYZ endstops, controlling the TPH stepper motors, and interfacing with a computer via USB. For the implemented system, a HP 8753 two-port VNA provides calibrated measurements as requested by the PC based controller. The VNA is capable of measuring S and Z Parameters and transferring them to the PC based controller. The PC based controller directs the operation of both the RAMBo 1.4 board and VNA, records the results.

4.2.3 Software Subsystem

The software is divided into RAMBo 1.4 based MPCNC controller firmware and full system coordinating PC based controller with a TkInter GUI for ease of access. The RAMBo 1.4 runs on modified open-sourced Marlin firmware [136], which is optimized for the MPFCS.

The MPFCS GUI coordinates the timing and intention of movements sent to the MPCNC stepper motors and receives measurements requested from the VNA, Fig. 4.3. After acquiring a measurement from a given location, the MPFCS GUI collates the data recorded from the

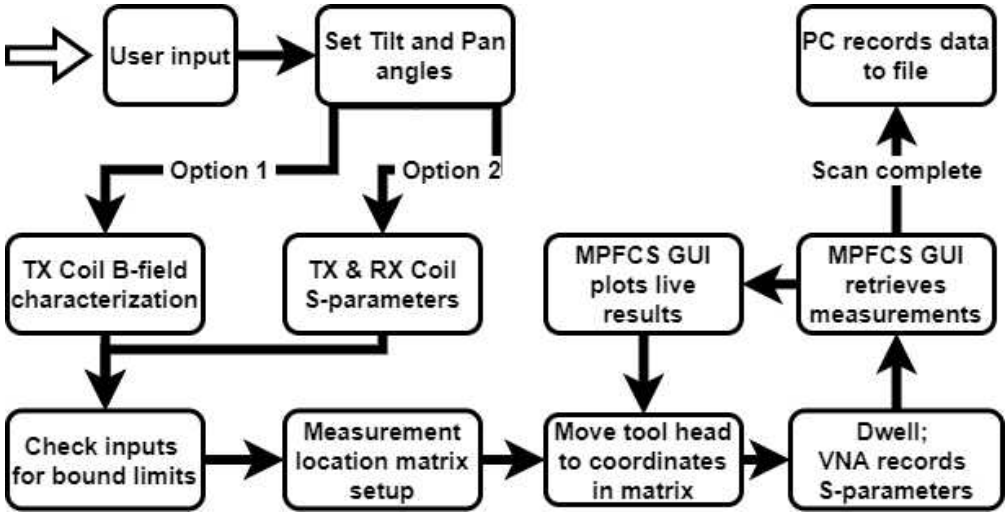

Figure 4.3: Software Operation

VNA with the RAMBo position information and plots results in real-time for the monitoring of scans. The latest RAMBo 1.4 firmware, MPFCS GUI, and instructions for the operation of the MPFCS can be found at https://github.com/usmank13/MPFCS.

4.3 Results

4.3.1 Calibration Measurements

MPFCS was evaluated for precision, reproducibility movement. To assess these qualities, the LED Laser Calibration Mount was first leveled with the horizontal surface on which the MPCNC is mounted using the incorporated bubble level. To measure the precision of the system, the MPFCS was directed to step through 36 equally spaced points around the trajectory of a circle with a 10mm diameter in the XY, XZ, and YZ planes as shown in Fig. 4.4. Marking these points with a fine pen, the planar error between the marked step endpoint and a circle of equal diameter centered at the same origin was averaged over all 36 points in each plane [133]. The average error was found to be 0.13mm, 0.135mm, and 0.068mm for the XY, XZ, and YZ planes respectively. Additionally, before proceeding to the endpoint of each step, the LED Laser Calibration Mount would return to the circle origin. By marking this location over 36 return to origin movements, the reproducibility is then

measured as the area encircled by the grouping divided by the number of returns to origin, resulting in a reproducibility error of ±0.025mm, ±0.029mm, ±0.028mm for the X, Y, and Z returns respectively. The TPH resolution was determined by stepping the respective motors by multiples of the manufacturer specified minimum step size until a repeatable noticeable change in the laser projection at the maximum separation dictated by the MPFCS volume was observed. The precision limit found to be ±0.5°, ±0.5° for the tilt and pan respectively.

4.3.2 Mode 1 - Complex Field Characterization

To demonstrate the time efficiency of 2-port S-parameter measurements in a volume on MPFCS in comparison to simulation, a pair of biased repeaters (BR) were swept through a volume 2x their CCD to measure $S_{21}[X, Y, Z]$.

BRs are commonly used in WPT setups, because in a series resonant circuit they allow for the doubling of the coupling coefficient [137]. Both the TX BR, affixed to the floor of the MPFCS, and the mobile RX BR, attached to the TPH, consisted of a loop coil, with an outer diameter (OD) of 38.5mm, offset by 15mm from a 50mm OD spiral and tuned to be resonant at 13.56MHz. With a step size of 2.5mm, the resulting NE quadrant of the swept volume is shown in Fig. 4.5. When the two coils are within their mutual near-field, the S_{21} reduces due to over-coupling. A second region of attenuation in S_{21} can be seen as a conical frustum sheet extending from the OD of the TX. On this plane, a portion of the flux through the RX cancels, thus reducing the measured S_{21}.

On a 32 core, 2.5GHz Intel Xeon CPU with 128GB of DDR4 2400 RAM, simulating

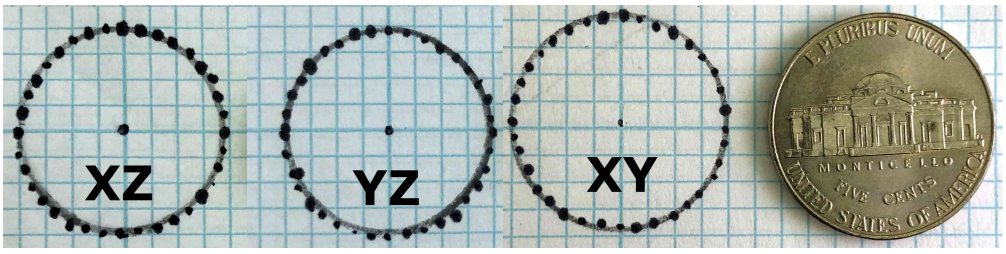

Figure 4.4: The concentric calibration circles in the XZ, YZ, and XY planes demonstrating the precision in the reaching the 36 programmed points and the return to origin location

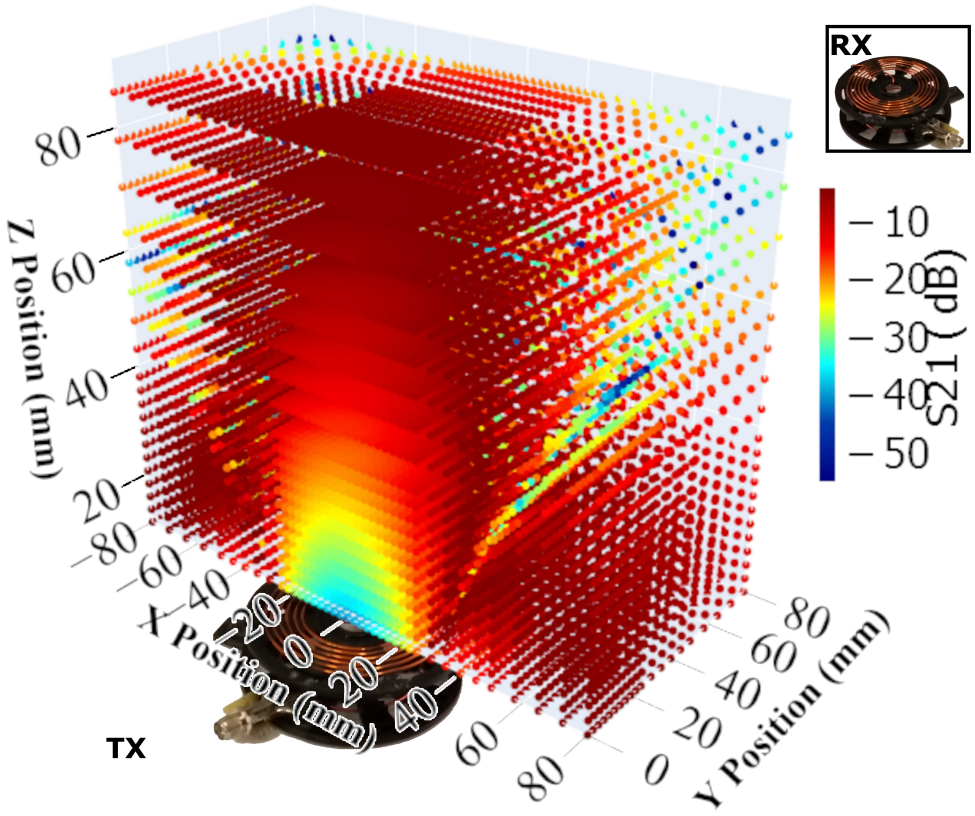

Figure 4.5: The S_{21} characterization of a volume where a biased repeater RX coil (inset top-right, but inverted from its sweep orientation) is swept at 2.5mm steps through the field resulting from a twin biased repeater TX coil.

S_{21} between a simplified digital twin of the pair of these biased repeater coils at 13.56MHz, with 201 points spanning 2MHz in a balanced ANSYS HFSS simulation, requires 23hrs 24min CPU Time (as reported by ANSYS HFSS) and 3hrs 11min per position interrogated. Moreover, this duration does not include the time intensive task impedance matching the coil for resonance at 13.56MHz. By comparison, with step sizes of up to 10mm, the MPFCS takes only 2.7s per movement and 0.21s per VNA measurement. If measuring the S-parameter outputs, this results in a 2600x reduction in measurement duration.

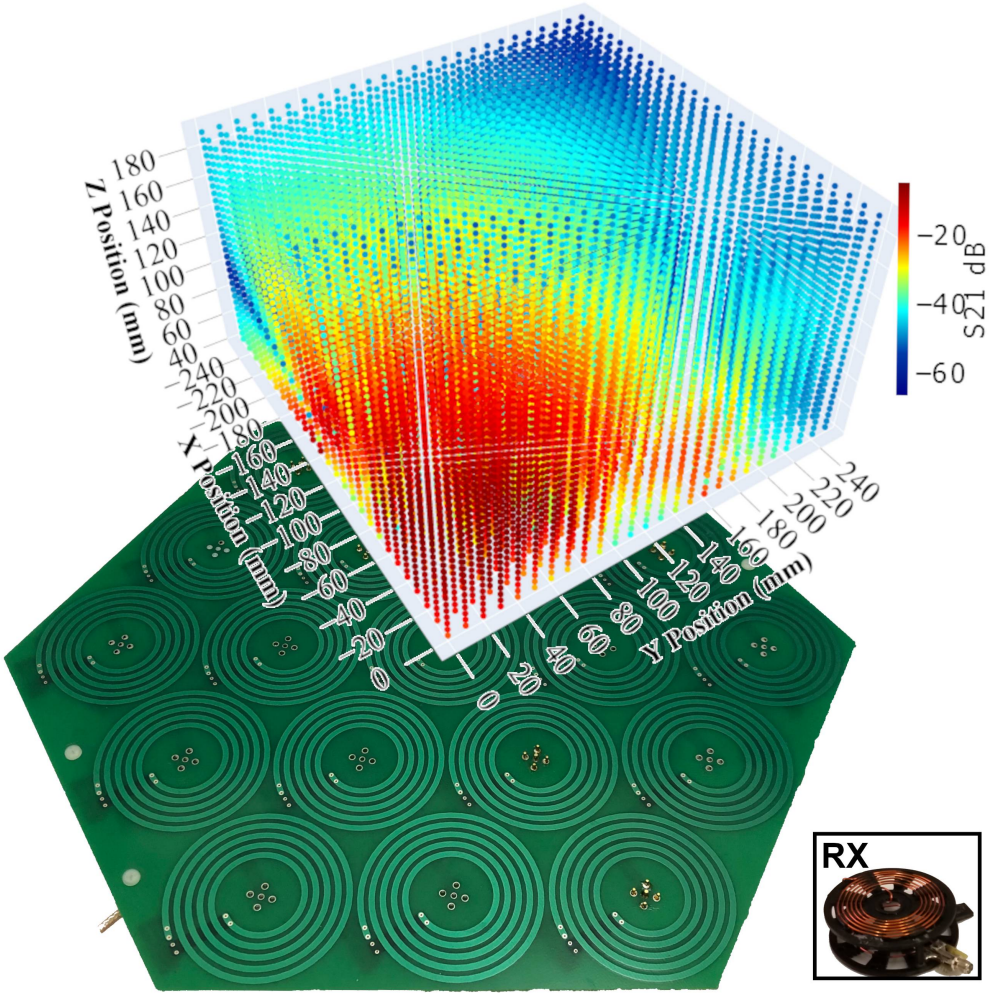

Figure 4.6: The S_{21} characterization of a volume where a biased repeater RX coil (inset bottom-right, but inverted from its sweep orientation) is swept at 2mm steps through the complex field resulting from a 2-D planar WPT array

Demonstrating where the MPFCS system truly excels, the same 50mm OD biased repeater is swept through the complex field resulting from a 2-D planar WPT array consisting of 19 planar spiral coils, each with an outer diameter of 60mm, and driven by a single centered coil [138], Fig. 4.6. While the MPFCS still requires a constant duration per measurement location, a simulation of even a single location for a 2-port S-parameter volume characterization would tax even capable of servers, and would likely require significant idealization in the design.

4.3.3 Mode 2 - Simple Loop B-Field Characterization

In contrast to characterizing 2-port S-parameter volume, measuring the B-field of a single TX coil demands only a single simulation run at the frequency of interest. To mimic the process completed by the MPFCS, a flux surface could then be swept through the locations of interest in post-processing and the average B-field through the surface could be calculated. For example, a simple 38.5 OD loop coil without impedance matching, Fig. 4.7b, requires 47min CPU Time and 22min Real Time, neglecting post-processing time. By comparison, sweeping the Beehive 100B at 2mm steps through a quarter volume with extents equal to 2x the CCD requires more than 9hrs. This being said, as additional high permeability and conductive structures, e.g. biological phantoms, are added to the simulation environment the time efficiency of simulation rapidly deteriorates.

To verify the ability of the MPFCS to effectively characterize the B-field resulting from a given coil, a physical twin of the simulated single loop coil above, which has been matched to the simulated S_{11} at 13.56MHz and 0dBm was chosen as a computationally uncomplicated reference for comparing the measured B-field from the MPFCS with a simulated replica. The 38.5mm CUT was centered at X, Y = (300mm, 300mm) and affixed to the floor of the MPFCS and the Beehive 100B probe was then swept in 2mm steps through the quarter volume up to the CCD. The resulting B-field at 13.56MHz, Eq. 4.1, is then shown in Fig. 4.7a.

Once the two S_{21} outputs were aligned, the system achieved 0.77dB Normalized RMSE over the full matrix of measurement locations, well within the 3dB quoted accuracy specified

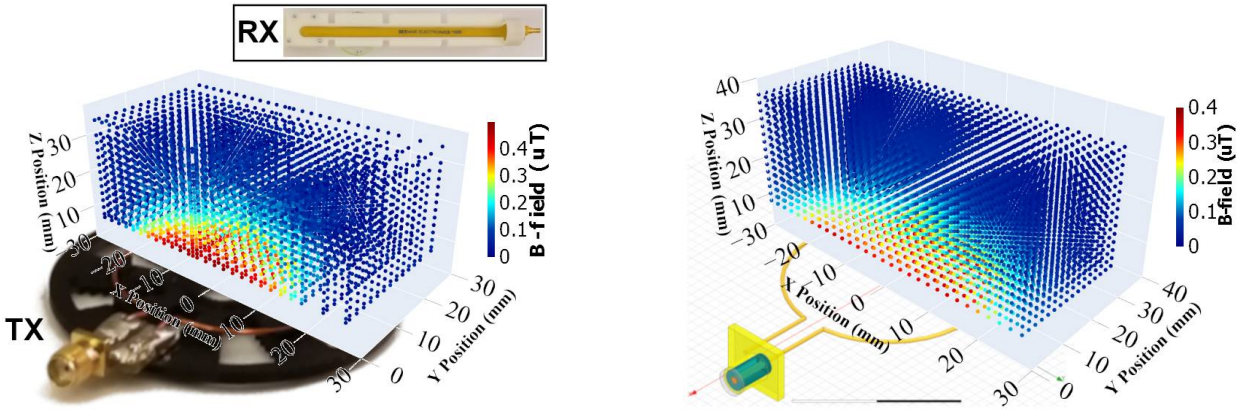

(a) (b)

Figure 4.7: (a) Measured B-Field by the Beehive 100B from a 38.5mm Non-resonant Loop (b) The simulated B-Field from a digital twin of the 38.5mm Non-resonant Loop.

for the Beehive 100B probes.

4.4 Discussion

Although the MPCNC was intended to be used as a CNC, by changing the end effector it becomes a versatile tool for repeatedly executing any task across a volume. While this work demonstrated high-precision volumetric characterization of fields, the system could be repurposed for other types of sensing (EMC Testing) and measurement (3D Scanning).

The high-fidelity measurements possible with the MPFCS will enable statistical model development (e.g. physics driven machine learning) for systems that are prohibitively complex or impractical to model analytically. This can feedback into the coil design and prototyping process as well as provide insights into edge cases for future WPT application.

Chapter 5

ANALYSIS AND DESIGN OF AN ASYMMETRIC RESONANT WIRELESS POWER TRANSFER SYSTEM: OPTIMAL INTERMEDIATE COIL SIZE AND LOCATION

In recent years, studies in WPT have been focused on its application in the near field, such as close-range WPT that adopts the magnetic inductive coupling [139–142] or mid-range WPT which utilizes Magnetic Resonant Coupling (MRC) [143–148]. Applications range from the supplying power to commuter busses [149] all the way down to human implantable devices [150] and across many formerly hostile environments such as ocean going [151] or extraterrestrial based operations [152].

In this paper, the MRC WPT is utilized, such that both transmitter (TX), consisting of a loop coil (TXL) and a spiral coil (TXC), and receiver (RX), consisting of a loop coil (RXL) and a spiral coil (RXC), are tuned to the same resonant frequency, 13.56MHz. High-power transmission of a MRC WPT system is generally realized within two coil diameters [153], as power transfer efficiency decreases with distance, which does not still satisfy the desires of the consumer market since the diameter of the coils are generally in mm-scale. The effects of Intermediate Coils (ICs) have been shown as a means to increase the transmission distance [154, 155], and alternative designs of such a system consisting of ICs has been proposed [156, 157]. While previous works have shown that the proper addition of one or more ICs could increase transmission distance, power transfer efficiency, and the transferred power to a conventional four-coil system, for the optimal location and size of an IC that ensure decent amount of power transfer are not covered.

In this paper, we will show the optimal location of an IC that gives the maximum transferred power and the size that gives the optimal transferred power in the MRC WPT system.

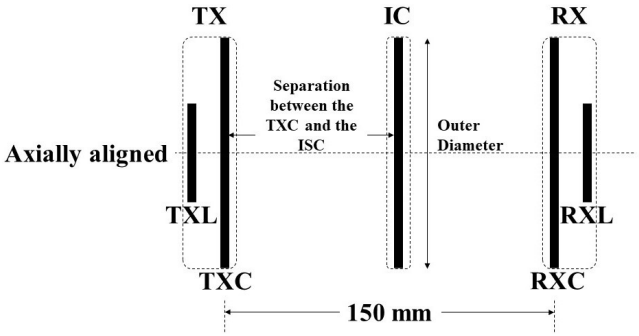

Figure 5.1: An Aerial view of the axially aligned five-coil system. In the examined symmetric system, the outer diameter (OD) of TX and RX are identical. In the examined asymmetric system, the OD of the TX is 3x the OD of the RX. The location of the IC, as well as the OD of the IC, are swept to determine the optimal location and size for maximum transferred power.

The five-coil system used here, i.e. TXL-TXC-IC-RXC-RXL (as shown in Fig. 5.1), is analyzed by using circuit theory in Section 5.1. To determine the parameters that maximize the power transferred to the load, the linear magnitude of scattering parameter S_{21} is quantitatively simulated and experimentally measured. Because multiple resonant frequencies will appear when coils are over coupled (so called frequency splitting in [145]), we chose to collect the S_{21} data at the designed resonant frequency, since such frequency will provide the maximum magnitude of S_{21} in the system of odd number of coils [155]. A symmetric and an asymmetric system have been designed, the former consists of identical TX and RX while the latter consists of a TX OD that is 3x larger than the RX OD. The system setups, including the experimental setup and quantitative simulation setup, are demonstrated in Section 5.2. Then, in Section 5.3, the optimal location of ICs of varying sizes in both systems are provided, and simulation and experimental results are compared.

This paper provides guidance for the optimal location and size of an IC in the five-coil MRC WPT system, whether symmetric or asymmetric.

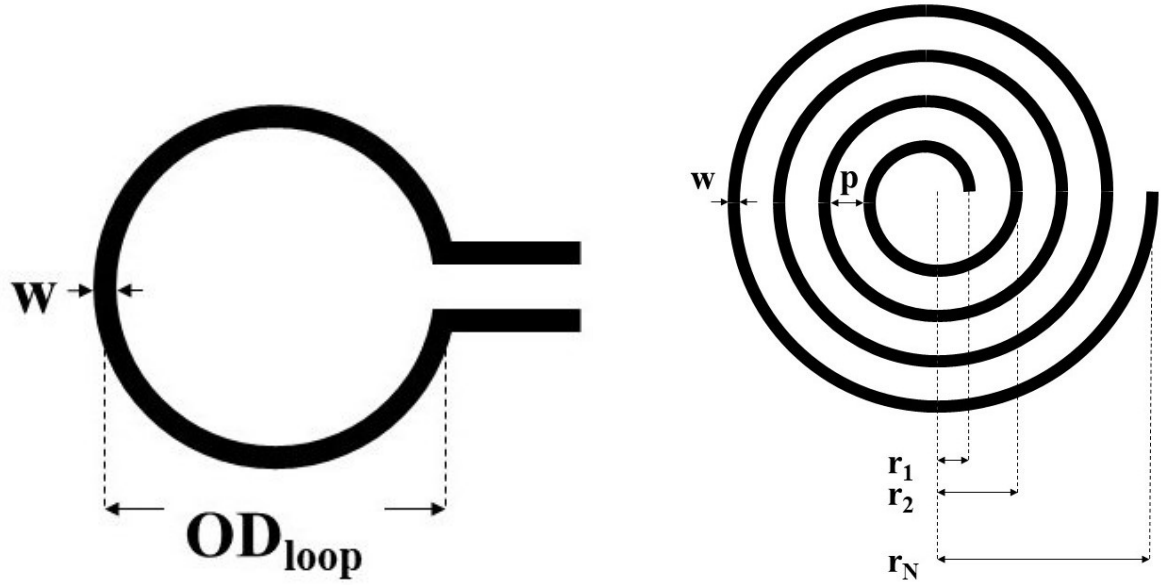

(a) (b)

Figure 5.2: (a) shows the geometry of a loop coil that has a OD of OD_{loop}. (b) is the geometry of a multi-turn single layer spiral coil that has N turns, separation of p between each turn, and the radius of each turn $r_{i^{th}}$. w is the wire diameter for both coils.

5.1 System Analysis

With the presence of an IC, the conventional four-coil system (loop-coil-coil-loop) becomes a five-coil system (loop-coil-intermediate-coil-loop). Then, the system is analyzed using the circuit theory so that the quantitative model can be compared with the experiment and determine the generalizability of the system. In Fig. 5.3, the system circuit model is shown and all parasitic or designed components are indicated by lumped elements R, L, and C. The TXL and RXL are loop coils consisting of a single turn (shown in Fig. 5.2a), the former connecting to a voltage source, V_{source}, with a source impedance, R_{source}, and the latter connecting to a load, R_{load}. L_1, L_4 and R_{p1}, R_{p4} designate self-inductance and parasitic resistances of the two loop coils respectively, and C_1, C_4 designate the tuned capacitance, which set the loop coils to resonate at the designed frequency. The TXC, IC, and RXC are multi-turn single layer spiral coils that have self-inductance of L_2, L_i, L_3 and parasitic

resistance of R_{p2}, R_{pi}, R_{p3}, respectively. Capacitors C_2, C_i, C_3 are added to tune the spiral coils to the resonant frequency. M_{12} and M_{34} are the mutual inductance (M) between TXL and TXC and between the RXL and RXC, respectively. M_{2i} and M_{3i} are the M between TXC and IC and between the RXC and IC. The M of nonadjacent elements are neglected, e.g. M_{14}, M_{13}, etc., as they are minuscule by comparison [145].

$$\begin{aligned} ID_{spiral} &= 2r_1 \\ OD_{spiral} &= 2r_N \end{aligned} \tag{5.1}$$

The generalized self-inductance L is defined by the geometry of a coil. As shown in Fig. 5.2, parameters of both loop coil and multi-turn single layer spiral coil are defined. In Fig. 5.2a, OD_{loop} and w indicate the OD of the loop coil and the wire diameter respectively. In Fig. 5.2b, w, N, p, and R_N indicate the wire diameter, the number of turns, distance between each turn, and the radius of N^{th} turn respectively. The inner diameter, ID_{spiral}, and the outer diameter, OD_{spiral}, of a spiral coil is defined in (5.1). All units of length are in meters.

The equation for the L_x of spiral coils (5.2a) is defined in [158], which is a modified form of Wheeler's formula. For loop coils (5.2b), it's a modified form of Kirchhoff's formula which can be found in [159]. In both, the inductance is measured in Henries.

$$L_{coil} = \frac{N^2(OD_{spiral} - N(w+p)^2)}{16OD_{spiral} + 28N(w+p)} \frac{39.37}{10^6} \tag{5.2a}$$

$$L_{loop} = 2\pi OD_{loop}(\log \frac{4OD_{loop}}{w} - 1.75)10^{-7} \tag{5.2b}$$

The generalized equation for M_{AB} from [158] is modified by summing all the mutual inductances of i^{th} turn of the primary coil A to j^{th} turn of the secondary coil B 5.3, and has

units of Henries. The radii r_{Ai} and r_{Bj}, N_A and N_B define the geometry of the two coils, d indicates the distance between them, and μ_0 is the free space permeability.

$$M_{AB} = \sum_{i=1}^{N_A} \sum_{j=1}^{N_B} \mu_0 r_{Ai} r_{Bj} \int_0^{\pi} \frac{\cos\theta}{\sqrt{r_{Ai}^2 + r_{Bj}^2 + d^2 - 2 r_{Ai} r_{Bj} \cos\theta}} d\theta \tag{5.3}$$

The coupling coefficient [145] is proportional to the mutual inductance between the primary and the secondary coils (5.4), normalized by the self-inductances.

$$k_{AB} = \frac{M_{AB}}{\sqrt{L_A L_B}} \tag{5.4}$$

The tuned capacitance (5.5) is defined by the equation of resonant frequency of RLC circuits and its value is assumed to be dominant as it is generally large enough that the self-capacitance of a coil is negligible [158] addition. The f_0 in the equation indicates the designed resonant frequency, and the unit of capacitance is in Farad.

$$C = \frac{1}{(2\pi f_0)^2 L} \tag{5.5}$$

The parasitic resistance of a coil, R_p (5.6a), consists of both a conductive as well as radiative loss [160]. The frequency dependent conduction loss at high frequencies is better described as the resistive skin effect, R_{skin} (5.6c), which modifies R_{DC} (5.6b) to account for shell distribution of current within in a wire at high frequencies. The radiative proximity effect loss, $R_{proximity}$, results from the electron crowding due to EM fields of nearby wires within a given coil (5.6d).

$$R_p = R_{skin} + R_{proximity} \tag{5.6a}$$

$$R_{DC} = \frac{l}{\sigma\pi(\frac{w}{2})^2},\ l = \frac{1}{2}N\pi(OD + ID) \tag{5.6b}$$

$$\begin{aligned} R_{skin} = R_{DC}\frac{\gamma}{2}\frac{ber(\gamma)bei^{'}(\gamma) - bei(\gamma)ber^{'}(\gamma)}{(ber^{'}(\gamma))^2 + (bei^{'}(\gamma))^2} \\ \gamma = \frac{w}{\delta\sqrt{2}},\ \delta = \frac{1}{\sqrt{\pi f\sigma\mu_0}} \end{aligned} \tag{5.6c}$$

$$R_{proximity} = R_{DC}\frac{-2\pi\gamma}{\sigma}\frac{ber_2(\gamma)ber^{'}(\gamma) + bei_2(\gamma)bei^{'}(\gamma)}{(ber(\gamma))^2 + (bei(\gamma))^2} \tag{5.6d}$$

Where σ is the copper's conductivity, δ denotes the skin depth.

By applying Kirchhoff's Voltage Law (KVL), the relationship between current and voltage in each coil is shown in (5.7).

$$\begin{vmatrix} I_1 \\ I_2 \\ I_i \\ I_3 \\ I_4 \end{vmatrix} \begin{vmatrix} Z_{11} & Z_{12} & 0 & 0 & 0 \\ Z_{21} & Z_{22} & Z_{2i} & 0 & 0 \\ 0 & Z_{i2} & Z_{ii} & Z_{i3} & 0 \\ 0 & 0 & Z_{3i} & Z_{33} & Z_{34} \\ 0 & 0 & 0 & Z_{43} & Z_{44} \end{vmatrix} = \begin{vmatrix} V_{source} \\ 0 \\ 0 \\ 0 \\ 0 \end{vmatrix} \tag{5.7}$$

Then the ratio of load to source voltage provides the voltage gain, as solved from (5.7), and yields (5.8).

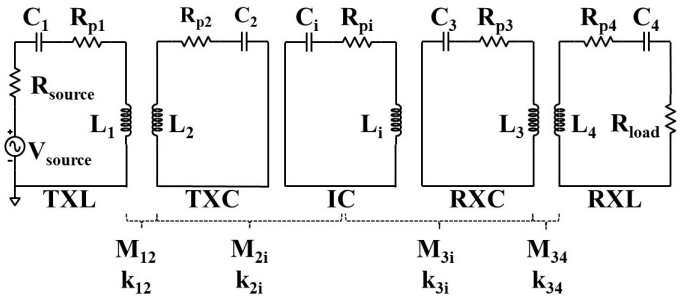

Figure 5.3: The equivalent circuit model of the conventional MRC WPT system with an included IC.

$$\frac{V_{load}}{V_{source}} = \frac{Z_{12}Z_{2i}Z_{3i}Z_{34}R_{load}}{(Z_{11}Z_{22}Z_{ii}Z_{33}Z_{44} + Z_{11}Z_{2i}^2Z_{34}^2 + Z_{ii}Z_{12}^2Z_{34}^2 + Z_{44}Z_{12}^2Z_{3i}^2 - Z_{12}^2Z_{ii}Z_{33}Z_{44} - Z_{2i}^2Z_{11}Z_{33}Z_{44} - Z_{3i}^2Z_{11}Z_{22}Z_{44} - Z_{34}^2Z_{11}Z_{22}Z_{ii})} \tag{5.8}$$

The impedances along the diagonal in (5.7), e.g. Z_{11} to Z_{44}, represent the self-impedance of each coil, which consist of both resistance and reactance as detailed in (5.9).

$$\begin{aligned}
Z_{11} &= R_{source} + R_{p1} + j\omega L_1 + \frac{1}{j\omega C_1} \\
Z_{22} &= R_{p2} + j\omega L_2 + \frac{1}{j\omega C_2} \\
Z_{ii} &= R_{pi} + j\omega L_i + \frac{1}{j\omega C_i} \\
Z_{33} &= R_{p3} + j\omega L_3 + \frac{1}{j\omega C_3} \\
Z_{44} &= R_{load} + R_{p4} + j\omega L_4 + \frac{1}{j\omega C_4}
\end{aligned} \tag{5.9}$$

By contrast the off-diagonal elements of (5.8), e.g. Z_{12} or Z_{2i}, are the mutual-impedance of two adjacent coils. They can be substituted for M_{AB} via (5.10) [161].

$$
\begin{aligned}
Z_{12} &= Z_{21} = j\omega M_{12} \\
Z_{2i} &= Z_{i2} = j\omega M_{2i} \\
Z_{3i} &= Z_{i3} = j\omega M_{3i} \\
Z_{34} &= Z_{43} = j\omega M_{34}
\end{aligned}
\tag{5.10}
$$

If we replace the $\frac{V_{load}}{V_{source}}$ in (5.8) with (5.4), (5.9), and (5.10), then (5.8) can be rewritten in the following format with respect to the coupling coefficient.

$$
\frac{V_{load}}{V_{source}} = \frac{\omega^4 k_{12} k_{2i} k_{3i} k_{34} L_2 L_i L_3 \sqrt{L_1 L_4} R_{load}}{(Z_{11} Z_{22} Z_{ii} Z_{33} Z_{44} + \omega^2 (k_{12}^2 L_1 L_2 Z_{ii} Z_{33} Z_{44} + k_{2i}^2 L_2 L_i Z_{11} Z_{33} Z_{44} + k_{3i}^2 L_i L_3 Z_{11} Z_{22} Z_{44} + k_{34}^2 L_3 L_4 Z_{11} Z_{22} Z_{ii}) + \omega^4 (k_{12}^2 k_{34}^2 L_1 L_2 L_3 L_4 Z_{ii} + k_{12}^2 k_{3i}^2 L_1 L_2 L_i L_3 Z_{44} + k_{2i}^2 k_{34}^2 L_2 L_i L_3 L_4 Z_{11}))}
\tag{5.11}
$$

We can assume Z_{11} and Z_{44} equal R_{load} and R_{source}. Then (5.11) can be simplified as shown in (5.12).

$$
\frac{V_{load}}{V_{source}} = \frac{k_{12} k_{2i} k_{3i} k_{34} L_i \sqrt{L_1 L_4}}{k_{2i}^2 k_{34}^2 L_i L_4 + \frac{Z_{ii}}{R_L} k_{12}^2 k_{34}^2 L_1 L_4 + K_{12}^2 K_{3i}^2 L_1 L_i}
\tag{5.12}
$$

Finally, the scattering parameter S_{21} (5.13) can be can be derived from (5.8) or (5.11) by using [145]. Note that the S_{21} generally refers to the power received by port 2 from port 1, which is the power received by load from source in our system, and is thus designated here in order to stick to accepted nomenclature.

$$
S_{21} = 2 \frac{V_{load}}{V_{source}} \sqrt{\frac{R_{source}}{R_{load}}}
\tag{5.13}
$$

5.1.1 Optimal Location

Since lots of parameters are co-related, (5.12) can be rewritten to (5.14) by assuming $\alpha = \frac{k_{12}}{k_{34}}$, $\beta = \frac{L_1}{L_4}$, $\gamma = \frac{L_i}{L_4}$, and $Z_{ii} = R_{pi}$ at the resonant frequency. If the size of TX and RX remains unchanged, α will depends on the separation of loops and coils, β will be a constant, and γ will proportional to the geometry of the IC.

$$\frac{V_{load}}{V_{source}} = \frac{\alpha\sqrt{\beta}k_{2i}k_{3i}}{k_{2i}^2 + \frac{\alpha^2\beta}{\gamma}k_{34}^2\frac{R_{pi}}{R_{load}} + \alpha^2\beta k_{3i}^2} \tag{5.14}$$

Assuming the system is lossless ($R_{pi} = 0$), $\frac{V_{load}}{V_{source}}$ will then merely depends on the coupling coefficients of the system. The maximum value of (5.14) is 0.5, and we can derive (5.15), which is the key to solve the optimal location of an IC.

$$\frac{k_{2i}}{k_{3i}} = \alpha\sqrt{\beta} \tag{5.15}$$

Symmetric System In the symmetric system, where the TX and RX are identical, α and β is 1. The maximum value of $\frac{V_{load}}{V_{source}}$ can be found when $k_{2i} = k_{3i}$, which indicates that the optimal location is where an IC locates at the center of TX and RX.

Asymmetric System In the asymmetric system, the optimal location of an IC depends on the size and separation of TXL and TXC as well as RXL and RXC.

5.1.2 Optimal Size

By placing the IC to the optimal location, the value of $\frac{V_{load}}{V_{source}}$ will depends on both the parasitic resistance of the IC and γ, which solely relates to the geometry of IC. We found out that for a certain range of size of IC, the value of $\frac{V_{load}}{V_{source}}$ will barely change. We define the size of IC that starts transferring static power as the optimal size.

5.2 System Setup

5.2.1 Experimental Setup

To minimize sources of variation, all of the coils have been designed to have exactly seven turns, using the same wire diameter of the same wire type of wire (Magnet wire, 20 AWG), and having the same distance between each turn. Therefore, the primary independent variable for each coil is their OD. Fig. 5.1 is an aerial view for both symmetric and asymmetric systems, and all loops and coils are axially aligned. The separation between TXL and TXC, as well as RXL and RXC, is held at the distance where S_{11} is minimized (symmetric separation = 15mm, whereas in the asymmetric system, the large coil's separation = 35mm and the small coil's separation = 2mm). Using the above biased TX and RX in a series resonant circuit allows for the doubling of the coupling coefficient [155], and therefore is advantageous when attempting to maximize transferred power over longer separations between TX and RX.

The distance between the face of TX and RX, and therefore also TXC and RXC, is a constant 150mm. We sweep the IC from one end to the other, and its location along the axis is denoted by the separation between the TX and the IC. All coils are 200 mm above the metal experimental platform so that it will not interfere the WPT system. As show in

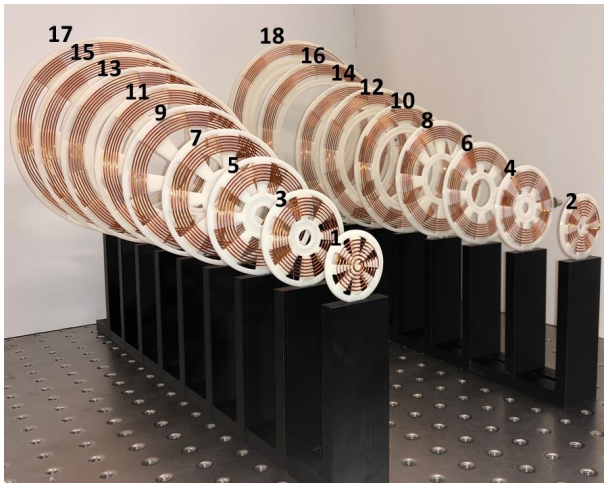

Figure 5.4: The tested ICs range from OD = 30mm to 200mm, in 10mm increments.

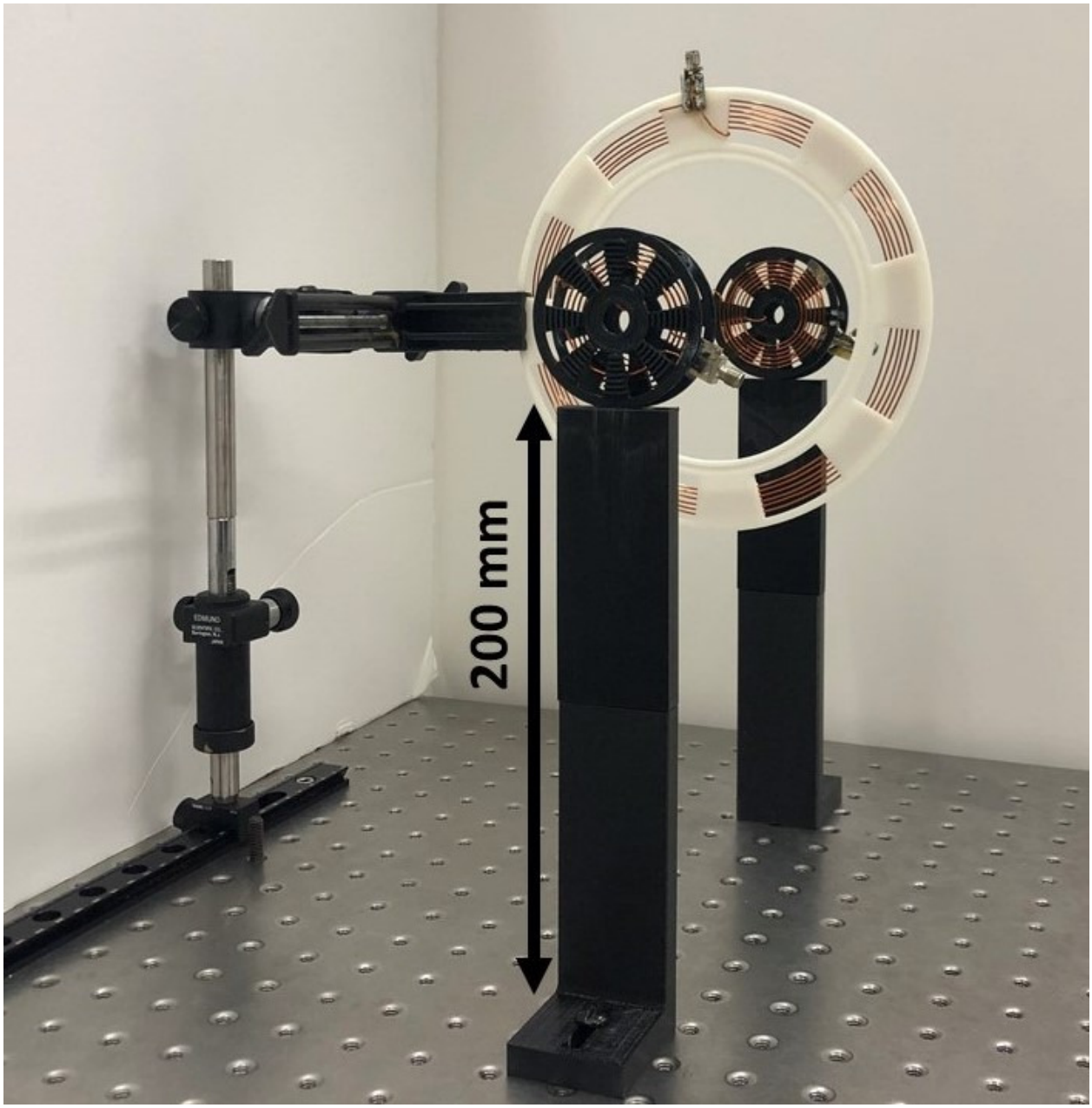

Figure 5.5: A rotated view of the experimental setup showing (from foreground to background) a given instance of the TX, IC, and RX variations.

Fig. 5.4, we had designed ICs with ODs from 30 to 200 mm at 10 mm interval. Fig. 5.5 shows the experimental set-up of the symmetric system where the TX and the RX are identical.

In this symmetric system, as a reference for this work, both the TXC and RXC are designed to be multi-turn single layer spiral coils that have a 50 mm outer diameter. Both TXL and RXL are loop coils that have a 38 mm OD. In the case of the asymmetric system, we have designed the OD of the TXC is 90 mm, that of the RXC is 30 mm, that of the TXL is 67.5 mm, and that of the RXL is 10.44 mm. The OD of the spiral coils to be tested was chosen to ensure the TX and RX are weakly coupled. Thus, the OD of TX was chosen to have a critical coupling distance of around 1/5 the TX to RX separation (150mm), where the critical coupling distance is $d_{TX-RX} = r_N/\sqrt{2}$ [153]. Then, the OD of RSC was chosen to be the minimum size possible while maintaining the same coil geometric associations (i.e. wire diameter, number of turns, and the separation between each turn). The scattering parameter S_{21} is measured by the HP8753E Vector Network Analyzer (VNA) at the designed resonant frequency.

5.2.2 Quantitative Simulation Setup

To provide additional insight towards optimal IC location and size selection, the chain of analysis followed in Section 5.1 was replicated in Matlab to mimic the experimental setup in 5.2.1. Key parameters, such as OD, number of turns, wire diameter, and separation between each turn, have the same values of those in the experimental setup. Within the simulation, the self-inductance (5.2a) (5.2b) and mutual inductance (5.3) are then calculated based on a given coils' geometry. In order to tune all coils to the designated resonant frequency, the value of tuning capacitance is derived from (5.5). Finally, from self-impedance (5.9) and mutual impedance (5.10) the magnitude of S_{21} (5.13) is derived and simulation results are reported alongside the experimental.

5.3 Experimental and Quantitative Simulation Results

5.3.1 Symmetric System

In the symmetric system, Fig. 5.6 results from sweeping the ICs of different sizes along the axis between the TX and RX. The horizontal axis shows the separation between the TX and the IC. The vertical axis shows the OD of the IC of different sizes. The intensity

of color represents the magnitude of S_{21}. The maximum magnitude of S_{21} within a given separation sweep is always located where the separation between the TX and the IC equals 75mm, which is the center of the TX and RX in the symmetric system, and the coupling coefficient of the TXC and the IC, $k_{TXC\text{-}IC}$, equals the coupling coefficient of the RX and the IC, $k_{RXC\text{-}IC}$. Our simulation shows the maximum magnitude of S_{21} and equal-coupling points are both located where the IC is centered between the TX and the RX.

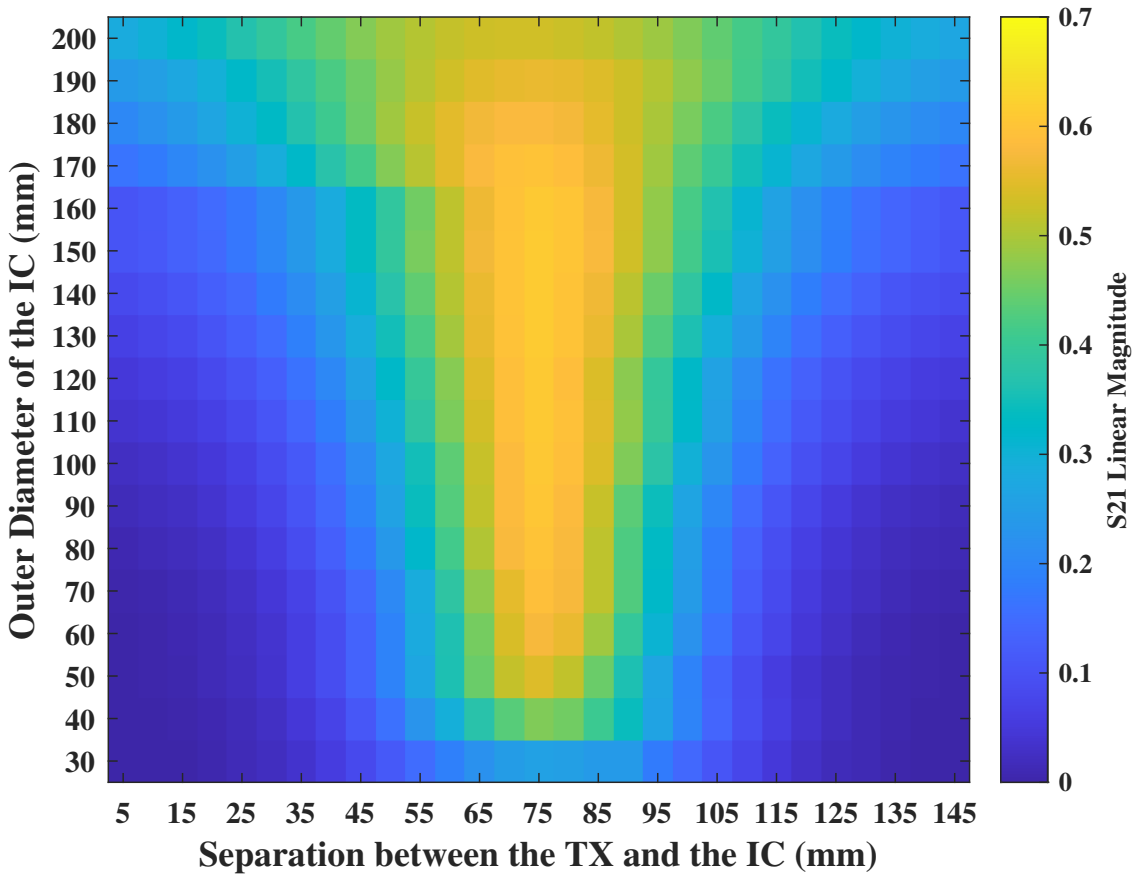

Figure 5.6: In the symmetric system (TXC OD = RXC OD = 50mm), a S_{21} heatmap resulting from sweeping ICs of different sizes(OD = 30mm to 200mm) through the separation between the TX and RX.

5.3.2 Asymmetric System

Similar to the symmetric system, Fig. 5.7 is the result of sweeping ICs of different sizes in the asymmetric system. The maximum magnitude of S_{21} is always closer to the RX, which is the smaller coil side. This phenomenon has also been analyzed and experimentally shown in [155]. In addition, the location of ICs where maximum S_{21} present in the asymmetric system gradually shifts closer to the RX as the OD of ICs gets larger. Note, this result is mirrored when RX replaces TX as the the transmitter (i.e. $S_{21} = S_{12}$).

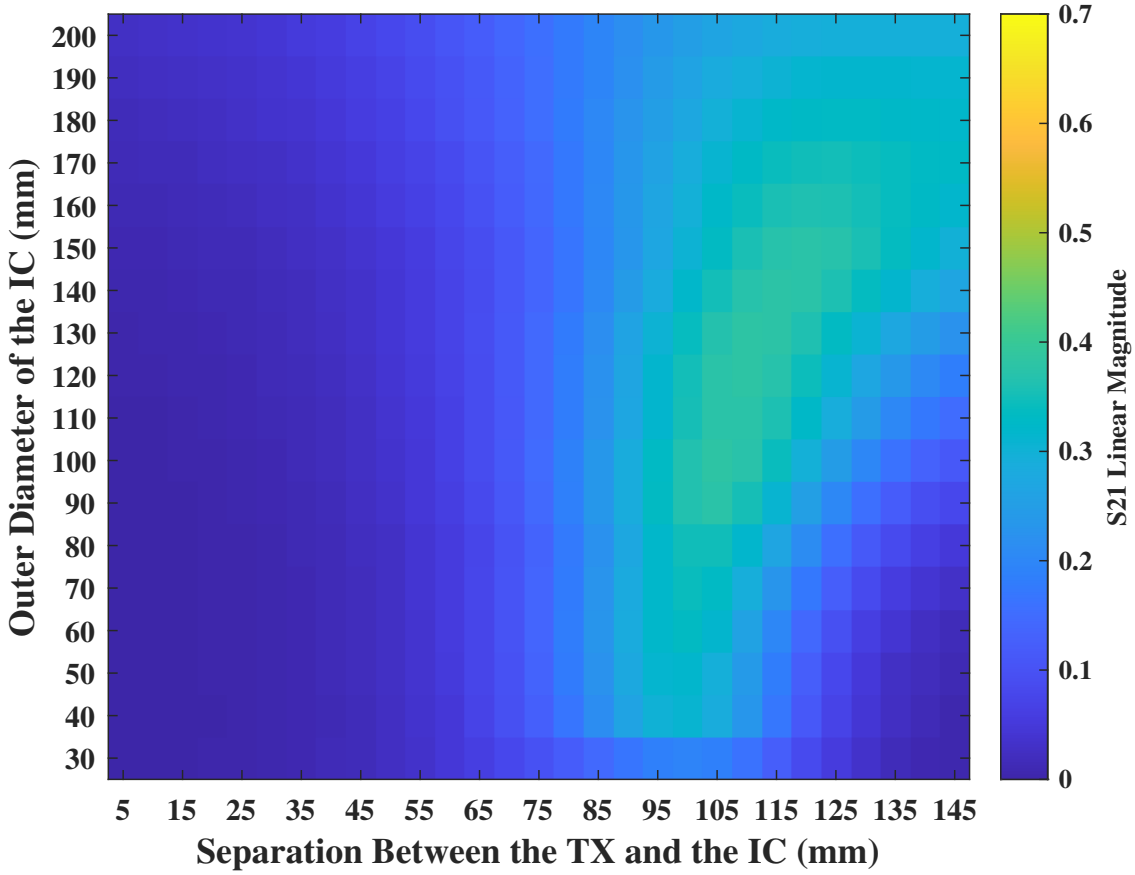

Figure 5.7: In the asymmetric system (TXC OD = 90mm, RXC OD = 30mm), a S_{21} heatmap resulting from sweeping ICs of different sizes (OD = 30 mm to 200mm) through the separation between the TX and RX.

As shown in Fig 5.8, we compare the location of the $k_{TXC\text{-}IC} = k_{RXC\text{-}IC}$ in simulation and the location of the IC where the maximum magnitude of S_{21} present in simulation and measurement. The simulated maximum of S_{21} location matches with the measured maximum of S_{21} location in general, and the simulated equal-coupling location is different from the measurement by 6.67% in most of the tested cases because we have neglected the inter-coupling coefficients ($k_{TXL\text{-}RXC}$, $k_{TXL\text{-}RXL}$, etc.).

5.3.3 Optimal IC Size

While it may seem that a larger IC may result in monotonically increasing magnitude of S_{21}, Fig. 5.6 and Fig. 5.7 show experimental results that suggest the optimal size of an IC in both symmetric and asymmetric systems. In Fig. 5.6 and Fig. 5.7, the magnitude of S_{21} will increase with increasing size of ICs up to a given OD, but then continuously decrease after it is larger than a certain size. With the given experimental setup, the optimal size of the IC is OD 150mm for the symmetric system, which is 3x larger than the OD 50mm TXC and RXC, and 140 mm for the asymmetric system, which is 1.6x larger than the OD 90mm TXC and 4.7x larger than the OD 30mm RXC.

5.4 Conclusion

After analyzing the circuit model of the five-coil system, and through the above experiments, quantitatively simulated and experimentally measured results have been compared. We have found that the optimal location of an IC in both symmetric and asymmetric systems is located where the TX and RX are equally coupled to the IC. Then, from the experimental results in the given setup, we have determined that there exists an optimal size of IC in both symmetric system and asymmetric system, and the size is larger than both TX and RX.

Future work includes deriving more explicit formulas for better predicting the optimal size in the above 5-coil setup, and incorporating an optimal separation of the loop and spiral coils for both the TX and RX.

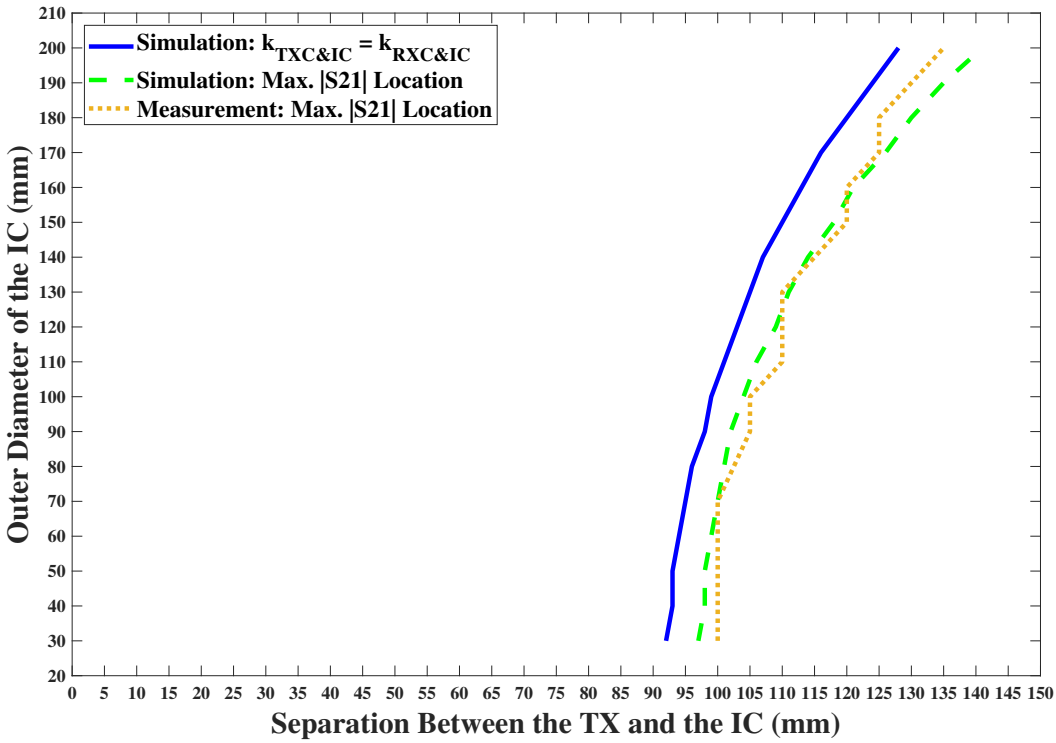

Figure 5.8: In the asymmetric system (TXC OD = 90mm, RXC OD = 30mm), Equal-coupling location (Simulation) (mm) vs. Maximum S_{21} Location (Simulation) (mm) vs. Maximum S_{21} Location (Measurement) have been compared through the separation between the TX and RX.

Chapter 6

COMMERCIAL OFF-THE-SHELF WIRELESS INJECTABLE ELECTROCEUTICALS FOR TRANSLATIONAL RESEARCH

6.1 Commercial off the Shelf Injectable Electroceutical Introduction

Custom designed technologies that provide internal body monitoring and control have significantly improved the quality of life for the population at large. From chemical, temperature, and identity monitoring systems to cochlear, pacemaker, and deep brain stimulation platforms, as of 2019, 8-10 % of the USA population have received FDA approved injectables or implantables. A further portion of the population has received more transient chemical and optical sensing ingestibles systems. The efficacy of these electroceuticals are providing demonstrated beneficial therapy to users. The key aspects of these electronic devices include the following:

- Miniaturized form-factor in order to reduce invasiveness
- Bio-compatibility in order to safely integrate with the body
- Safe management of heat within the tissue in order to reduce tissue damage during the device operation
- Low-power circuit design in order to operate over long periods of time (and again reduce heating)
- Untethered operation via any combination of wireless power, wireless data, and battery power supply in order to perform the specified function

The untethered operation of implantables have enabled users to live natural lives unencumbered by protruding wires and with reduced internal exposure to pathogens. Despite the

form-factor and biological limits that bind device designers, careful system design can allow for the safe delivery of 10s mW of power and 100s $kbps$ of telemetry. thereby providing the framework for effective sensing and stimulation for therapeutic benefits.

While implantables have demonstrated incredible functionality in this persistent therapeutic domain, the open surgery requiring incisions larger than the physical dimensions of the bulk device structure have led to post-surgical complications [162]. To provide greater therapeutic space coverage, and thus benefit to a greater portion of the population, electroceutical development should be oriented towards devices that can be implemented through outpatient services and reduce infection risk. This need is well addressed by high aspect ratio structures that can be delivered through injection by a small diameter needle.

In order to accelerate the development in this direction and provide a safe, stable paradigm for electroceutical based therapy development, we present an inexpensive 12 gauge needle form-factor wireless power, uplink, and downlink platform supporting the development of electroceutical based sensing and stimulation systems for translational research.

This document will be organized following the linear progress in the project, from functional testing to deployable systems. However, to start with the end in mind, two applications are discussed to provide focus for the work involved in the project.

6.2 COTS Injectable Electroceutical Example - Application Specific - The Smart Breast Clip Overview

The goal of this application and associated research is to demonstrate that wireless Smart Breast Clip injectable (SBC), which are similar in size to standard breast radiological markers, can provide continuous functional sensing within tumors. We envision that these devices can then be used to develop and implement new response-guided breast cancer treatment approaches. Smart breast clips are wireless optical-based sensors that continuously probe the local tumor microenvironment and report molecular information such as intratumoral hemoglobin oxygen saturation, water composition, and lipid composition. While similar optically-derived signals have been demonstrated to measure chemotherapy response, the proposed smart clip approach will improve optical sensing performance where it currently

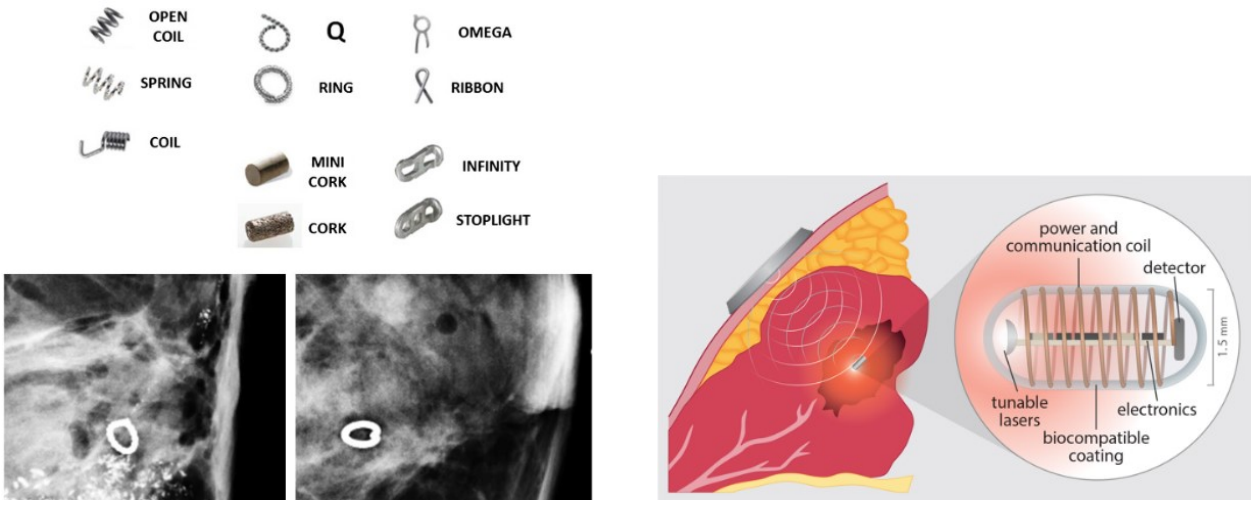

(a) (b)

Figure 6.1: (a)(top)Standard breast radiological markers [8] (b) Early conceptualization of the Smart Breast Clip [9]

fails: in deep tumors and tumors surrounded by dense fibroglandular tissue (e.g. areola) due to limited depth penetration and high optical attenuation. The smart breast clips, introduced using standard breast biopsy and clip placement techniques, could be deployed in primary breast tumors, positive auxiliary lymph nodes, and distant metastases that are biopsy-accessible. They will be interrogated with a skin-worn patch or a wand-based tool to provide local functional monitoring of tumor molecular targets and physiological properties at a frequency and duration not accessible with current imaging or liquid biopsy technologies.

SBCs are wireless optical-based sensors that continuously probe the local tumor microenvironment and report molecular information such as intratumoral hemoglobin oxygen saturation, water composition, and lipid composition. While similar optically-derived signals have been demonstrated to measure chemotherapy response, the proposed smart clip approach will improve optical sensing performance where it currently fails: in deep tumors and tumors surrounded by dense fibroglandular tissue (e.g. areola) due to limited depth penetration and high optical attenuation. The SBCs, introduced using standard breast biopsy and clip placement techniques, could be deployed in primary breast tumors, positive axillary

lymph nodes, and distant metastases that are biopsy-accessible.

The will be interrogated with a wand-based tool containing the wireless transmitter to provide local functional monitoring of tumor molecular targets and physiological properties at a frequency and duration not accessible with current imaging or liquid biopsy technologies.

6.2.1 Continuous Wave Near-infrared Spectroscopy Background

Standard breast radiological markers, Fig. 6.1a, allow for reliable re-identification and accurate localization of biopsied lesions, serve a critical role in correlating findings between imaging modalities, and help avoid larger surgical excisions than necessary [8]. Expanding on this simple, though crucial, function, SBCs, as envisioned in Fig. 6.1b, can provide rich real-time functional information of tumor (primary and metastasis) microenvironment that can be used to optimize treatment and, ultimately, extend survival.

To accomplish this the SBC will contain a ultra-small multiwavelength active optical sensing system that is wirelessly powered and interrogated. The sensing targets for our initial SBC are changes in the concentrations and molecular states of hemoglobin (oxy- and deoxy-) [163] in the tumor microenvironment using hyperspectral continuous-wave near-infrared (NIR) spectroscopy at 680 and 850nm. These optical biomarkers are directly related to tumor composition, metabolism and vascularity, and it has been shown in a multicenter clinical trial that noninvasive measurements of these parameters can predict pCR in women undergoing breast cancer neoadjuvant chemotherapy, which in turn predicts survival [164–168]. Later versions of the system could include a tuneable microchip laser [10], shown in Fig. 6.2b, that would enable methemoglobin [163], water (protein bound or free, temperature) [169–171], and lipid (saturated or unsaturated) [172] interrogation.

Going into more detail, light absorption of biological tissues is relatively low in the NIR domain (650-900nm), so reflected light provides noninvasive physiological information about deeper tissue layers. Continuous Wave NIR Spectroscopy can measure the concentration of tissue chromophores, as shown in Fig. 6.2a. Then changes in detected signal intensity can be related to oxy- and deoxy-hemoglobin concentrations according to the modified Beer-Lambert

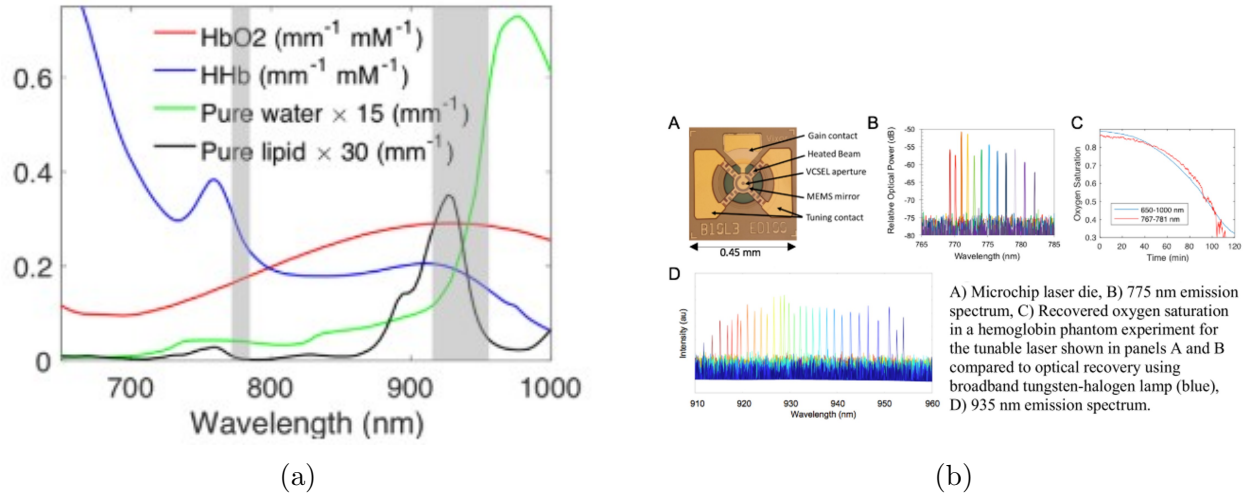

(a) (b)

Figure 6.2: (a)Targeted chromophores with tuneable laser bandwidth overlaid in grey (b) Prior work towards a Tuneable microchip laser [10]

law [173]. Over long periods of monitoring enabled by the SBC, the concentrations of these two chromophores should normalize as the tumor is responding to treatment. The relative fraction of HbO_2 to Hb informs how the tumor oxygen use is changing which allows a clinician to administer chemotherapy or radiation treatment when the tumor is most susceptible, when the concentration of oxygen is high.

6.2.2 Abbreviated Clinical Research Strategy

1. Smart Breast Clip Injectable - Phase 1 - Phantom:

   In the first phase of this project the SBC will be characterized for accuracy, precision, dynamic range, stability and depth range in a liquid tissue-simulating phantom system constructed from intralipid and nigrosin mixtures. This phantom will simulate ranges of tumor optical scattering and absorption with electrolytes that simulate EM attenuation.

2. Smart Breast Clip Injectable - Phase 2 - Murine Model

   In the second phase, 4T1 murine breast cancer cell lines will be injected in the mammary

pad of 40 immunocompetent BALB/cByJ mice and allowed to form tumors of 8-10 mm diameter. A portion of these mice will have an SBC injected to a depth of 1cm, we expect to quantify optical biomarkers of tumor progression in control subjects, including increased vascularity, unstable oxygenation, changes in lipid metabolism, and signs of increased cellularity.

3. Smart Breast Clip Injectable - Phase 3 - Human Model

   In the third phase, the SBC would be evaluated by injecting to a depth of 5cm or less in locally advanced tumors and axillary lymph nodes in neoadjuvant chemotherapy treatment, where it would be removed at surgery. Next, since the National Comprehensive Cancer Network (NCCN) guidelines recommend that tumor ER/PR/HER2 status be obtained via biopsy of a metastatic site [174], the smart clip could be introduced to monitor these biopsy-accessible sites. Since it is not standard to place clips in metastases, safety needs to be demonstrated and the smart clip could be removed via vacuum-assisted biopsy in cases of extraordinary response. Besides locally-advanced and MBC, our approach could also be used in individuals with high-risk benign lesions that would otherwise be monitored with short-interval imaging. This could also help address the challenge of distinguishing indolent from potentially deadly breast lesions.

6.2.3 System Design Requirements

Clinical

The primary constraining factors in this system are the safety and size requirements. The safety of the device will be determined following ISO10993-6:2016. By choosing appropriately biocompatible materials, minimizing the size, and limiting both conductive and radiative heating, we hope to limit tissue damage caused by the SBC. The encapsulated package will be designed to fit in a 12G needle (inner diameter = 2.159mm) and will be minimized in length so as to provide for a less intrusive incorporation into the tissue. An early mock-up of the SBC, with a long-axis helical coil and with populated components is shown in Fig. 6.3. An additional complication to plan for involves the injection depth. While injected depth for

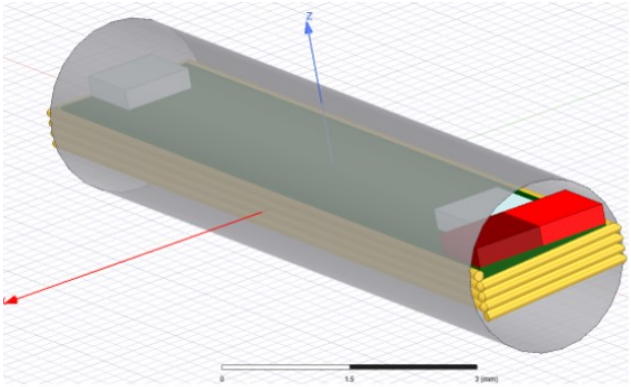

Figure 6.3: An 3D sketch of the proposed unencapsulated SBC with a helical coil along the long-axis within the confines of a 12G needle approximation (grey cylinder) showing the placement of the 680 and 850nm VCSELs as well as near and far GaAs PIN Photodiodes

accomplishing Phase 2 is only 1cm, follow-on projects will attempt to deploy later versions of the SBC in humans where the injection depth could reach 5cm.

An additional unique aspect of this project is the tight feedback loop between our clinical collaborators at the University of Notre Dame and the wireless injectable developers here at the University of Washington. Their expertise in optical design and clinical testing guided the development of the systems used in this project.

Hardware

With respect to the SBC required hardware, an overview of the system is shown in Fig.6.4. A WPT TX transmits a continuous wave sinusoid at 6.78 MHz which is radiated by an impedance matched (IMed) resonant biased-resonator TXC. The signal is monitored by a DAQ in order to log data uplinked from the RX to TX and provides feedback to the TX unit. The CW sinusoid is received by a 50 Ω IMed multi-turn RX Coil with dimensions of 2.1 mm by the length of the injectable PCB and drive the rectification and regulation circuitry. The resulting regulated 3.3V will power the MCU and an AFE4404 Optical Bio-sensor which in turn will drive a 680 and a 850nm VCSELs. The reflected NIR signal will be recorded by a GaAs PIN Photodiode. The AFE4404 measurements are relayed to the MCU, which the modulates the RX based IM network between short and load, in order to uplink data back to

the TX via LSK modulation. Additional uplinking of measurements of the voltage rectified from the HF input received by the coil and temperature measurements via a thermistor are possible via a 2ch MAX19777 ADC.

The TX and RX coil design must be accomplished in tandem. The RXC provides the primary design constraint, set to 50 Ω IMed multi-turn helix with dimensions of 2.1 mm by the length of the injectable PCB. The TXC must be designed such that it most efficiently transfers power to an RX with the above constraints. Firstly, for optimal power transfer efficiency ($max[\,S_{11}\,]$), the Q of the TXC should be maximized. However, the impedance that produces the maximal Q will need to be tempered by the possibility of excessive heating caused by the need for high TX output power. While a TXC design that has a large surface area, and therefore greater heat dissipation capabilities, would mitigate this heating issue an additional constraint revolves around optimizing the coupling coefficient between the TXC and the RXC (k_{21}), which is maximized when the coils are are of the same outer diameter and symmetric [175]. Further restricting the design space, for near-field resonant systems the field strength decreases at $(OD_{TXC}/d_{sep})^3$, where the OD_{TXC} is the outer diameter of the TXC and the d_{sep} is the separation distance between the TXC and RXC. So, for a given d_{sep}, the power transfer efficiency will be improved with a larger TXC, and thereby reducing the k_{21}. Finding an optimal TXC will then need to be that which best balances Q, heating, and k_{21}.

Communications

From a communications point of view, once the system is injected in a clinical setting, uplinked data would consist of measurements from the CW NIRS sensor, measurements of the rectified voltage power supply, RX system temperature, and system state information. The clinical requirements allow for uplinking measurements from the RX to the TX at very low datarates, below even 1 complete data acquisition cycle per hour, or around 5 data packets per hour, with each packet being 64 *b*. While interpacket datarate is extremely low, the intrapacket datarate needs to be significantly higher ($> kpbs$), since during every impedance

toggle to short, the power storage elements on the RX (e.g. tank capacitors) are sourcing power to the reliant components without receiving power from the TX. The upper limit on the datarate is bounded by the MCU, which is operating at reduced oscillator frequencies in order to minimize power consumption, but still capable of datarates ≈ 100 *kbps*.

In contrast, downlink communication from the TX to the RX has no restrictions. Downlink is intended to provide settings and functionality changes to the RX. The interpacket and intrapacket ASK datarate have no, within reason, lower limit below the maximum timer duration achievable by the MCU. The upper limit is restricted to the sampling and signal conditioning rates of the data acquisition system on the RX. Again, due to the reduced operating frequencies of these low-operating-power components, this would limit downlink datarates to less than $100s$ *kbps*, however the designed systems are intended to operate at datarates lower than $100s$ *bps*.

Operation

During start-up, the power delivered to the RX needs to be regulated as fast as possible via closed-loop uplinked feedback to the TX, in order to provide power without continuously overdriving, and thereby breaking, the front-end power conditioning circuitry. In opposition, while the system will run at low power, during start-up the instantaneous power (i.e. energy) requirements can nearly double. Additionally, in the application of wireless power between a TXC and RXC, alignment offset from the shared central axis and orientations deviating from parallel can result in varying power transfer efficiency. These myriad of operating conditions encourage the automation of the operation of full system (Controller-DAQ-TX-RX), in order to remove the likelihood that hard coded settings prohibit the RX functionality. This automation is accomplished via closed-loop feedback from the RX to the TXC to the DAQ and then on-wards to the client controlling both the DAQ and the WPT transmitter (e.g. a client coded for a PC). The client can then incorporate the received data into a real-time dataset, and adjust the TX power output as required.

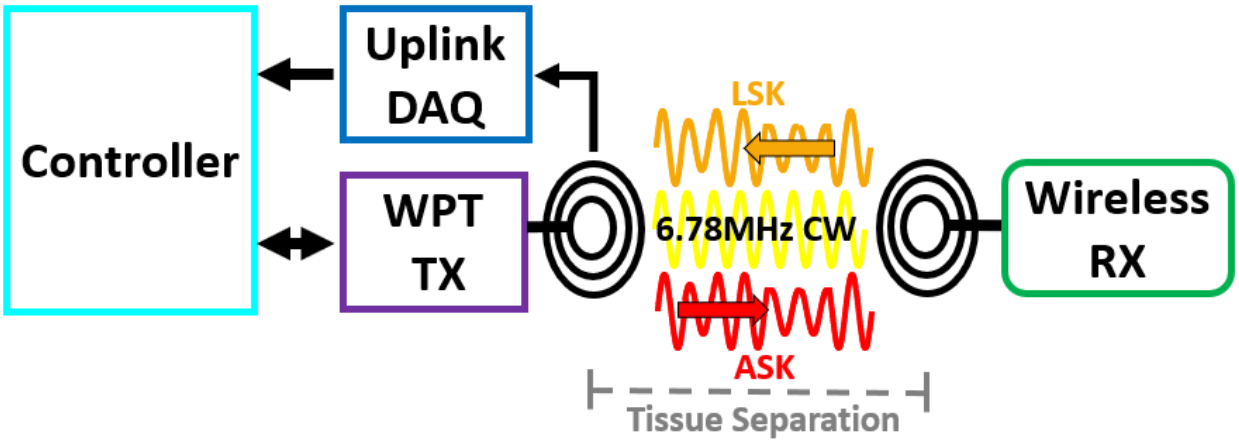

Figure 6.4: A block diagram representation of the TX and RX subsystems of the SBC.

6.3 COTS Injectable Electroceutical Example - General Platform - ElectRX Overview

In order to broaden the research impact of the work towards a COTS Injectable Electroceutical a second format is designed to serve as a generic platform providing wireless power, uplink and downlink communication, in a form-factor package with an outer diameter of $< 2.159\ mm$ for translating research developments in biological sensing and effector to clinical applications, but without requiring the development of application specific designs (e.g. SBC v10 - Mouse). This type of platform would provide immediate benefit to the many researchers who have developed a sensor or effector, demonstrated and reported functionality, but don't yet have the funds or work force to span the gap towards clinical use. With the ElectRX, the WPT and communications front-end operates independently and reliably from the sensor or effector being tested, thus enabling the future work that so many research proposals put forward.

6.3.1 System Design Requirements

The system requirements very closely match those found in Sec.6.2.3, except that where the SBC v10 - Mouse use an AFE4404 sensing system with VCSEL effectors and GaAs PIN Photodiodes, the ElectRX is sensor/effector neutral. As long as the sensor/effector can

interface via one of the externally exposed pads, the ElectRX will provide power and communicate the measurements from the sensor to the controlling client, or will take commands from the controlling client and communicate them to the effector.

To focus further on those areas where the system differs from the SBC v10 - Mouse, the ElectRX electroceutical platform, shown as a block diagram in Fig. 6.34 contains 6-pads to which a generic sensor/effector could be attached, including: 3.3V Supply, Analog Ground, a 12b ADC Input, a GPIO with alternate I/O timer functionality, as well as I2C Data and Clock with required pull-up resistors. The most significant difference though is that the injectable has a 2-turn coil spanning across internal layers 1 and 2 of the PCB, as shown in Fig.6.36a and 6.36b, respectively. The embedding of this coil, will allow the user of the platform to avoid having to develop around an externally mounted coil, and will allow for greater mass production, as the coil would not need to be wound by hand.

6.4 Smart Breast Clip v02 - Sense Board

In order to encourage a successful final product the development of the deliverable Smart Breast Clip was broken into multiple revisions. In each revision, functionality and implementation were confirmed, thus educating and derisking follow-up designs.

The v02 - SBC Sense Board was created as a derisking platform to test the compatibility of integrating the AFE4404, photodiodes, and VCSELs, on a 4-layer form-factor board while employing a wired External Real-time MCU (Arduino Uno Pro Mini 8MHz 3.3V) to control the various AFE4404 functionality via I2C communication, and to eventually record that data for analysis. This additionally allowed us to better approximate the expected performance of the final SBC, begin to develop RX firmware and client-side software, test initial coil designs, test encapsulation, test system heating, and begin to determine optimal AFE gain and DAC Offset settings while avoiding the fragility difficulties that come with designing a system at the edge of the fabricator's capability and using components that prioritize limiting size over user friendly integration.

The system has two modes tested for noise limitations. On the Top-side a single AFE4404 records scattered light from the two actuated VCSELS through switching between two pho-

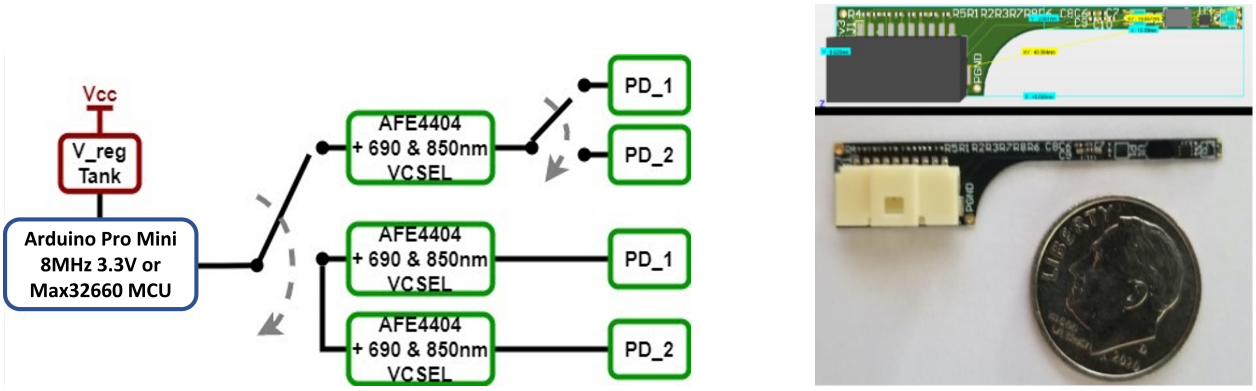

(a) (b)

Figure 6.5: (a) A block diagram demonstrating the form-factor sensor specific operation that can be tested (b) The fabricated and populated v02 - SBC Sense Board

todiodes ($PD_{near} = PD_1$ and $PD_{far} = PD_2$), where near and far are labeled with respect to the the proximity to the VCSELs.

6.4.1 Hardware

The SBC v02 - Sense board has a form-factor prong measuring $2.0x \approx 10\ mm$, which connects toa Molex Header on a large base section. The primary constituent components include 2x AFE4404 integrated optical bio-sensing analog front ends (AFEs), each driving two VCSELS (680nm and 850nm), and recording from either a single photodiode (the low noise condition) or two separated photodiodes switched between by a single-pole-dual-throw switch (the ambient reflectivity normalization test condition).

6.4.2 Coil Design

Coil Axis Orientation at 13.56MHz

Initial illustrations for the SBC had the RXC wrapped cylindrically around the short axis of the SBC, as shown in Fig. 6.2b. While aesthetically pleasing, this coil orientation consumed more headroom that a square helix wrapped around the long axis of the PCB, as can be seen in Fig. 6.7a. More importantly, for a SBC that is 15 mm in length, the surface area normal to the coil for the square helix coil is 36.4x that for the cylindrical coil. As the

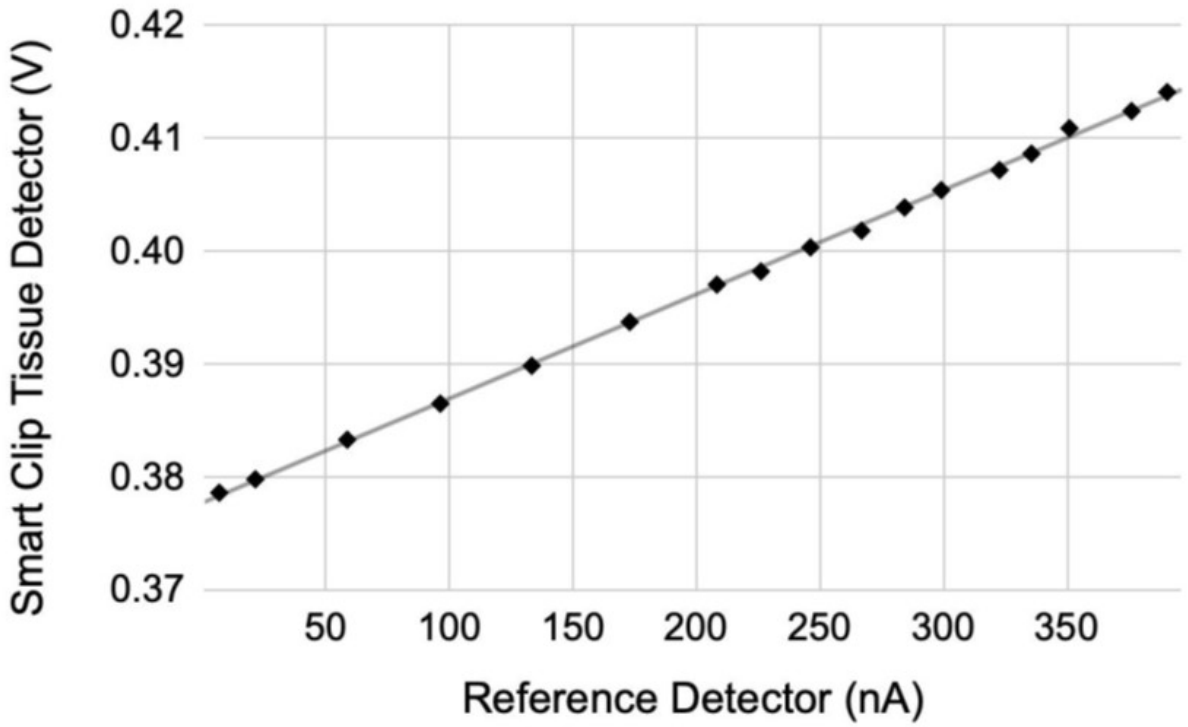

Figure 6.6: Tissue detector response (data points) compared to a reference photodiode for a varying source power. Solid line is a linear fit to the data ($R^2 = 0.999$).

induced EMF in a coil is proportional to the surface area, we hypothesized that the changing the coil orientation to a square helix coil would produce higher S21.

To test this cylindrical and square helix coil matched to 50 Ω to 13.56MHz that could fit within the 2.1 mm diameter opening of a 12G needle were driven by a biased-repeater coil, consisting of a 50 mm spiral coil resonant at 13.56MHz and a 27.5 mm loop matched to 50 Ω at 13.56MHz, at 10 mm steps in separation between 10 and 90 mm coaxial with the TXC. The resulting S21 measurements recorded by a HP 8753ES VNA are then shown in Fig. 6.7b.

As was suspected, the square helix coil demonstrated around 1.8 dB and 4.1 dB improvement at the 1cm and 5cm separations of interest to this project.

While it would be possible to improve the cylindrical coil (and the helix coil) by including a ferrite at the center of the injectable, this inclusion would prohibit the system from being used in MRI machines, which may be necessary according to a given user's needs.

RX Coil Design - S21 and Z11 at 6.78 MHz

With the coil orientation decided, a form-factor square helix coil with 6 turns was created that measured 2 mm by 10 mm and was tuned to 6.78 MHz. A biased-repeater of the same design as above was also tuned for 6.78 MHz. To determine an approximate PTE and expected modulation depth in air the RXC was swept away from the TXC in 1cm steps coaxial with the TXC, for example see Fig. 6.8a for the 5cm separation, and S11, S22, S21, and Z11 were measured by a HP 8753ES VNA, as shown in Fig. 6.8b. Note that the 10cm separation point was essentially the same as if the RXC was completely removed from the field.

As can be seen from the S21 plot in the Upper Right of Fig. 6.8b, at the two separations of special interest to this project, 1 and 5cm (see Sec. **??**), the S21 is -6.5 and -27.4 dB respectively. Relating this back to the approximated power demands of the RX in Sec. **??**, the TXC will only need to output approximately 2.4W during the worst case power demand.

While the power demand from the TXC is readily achievable, the load modulation at

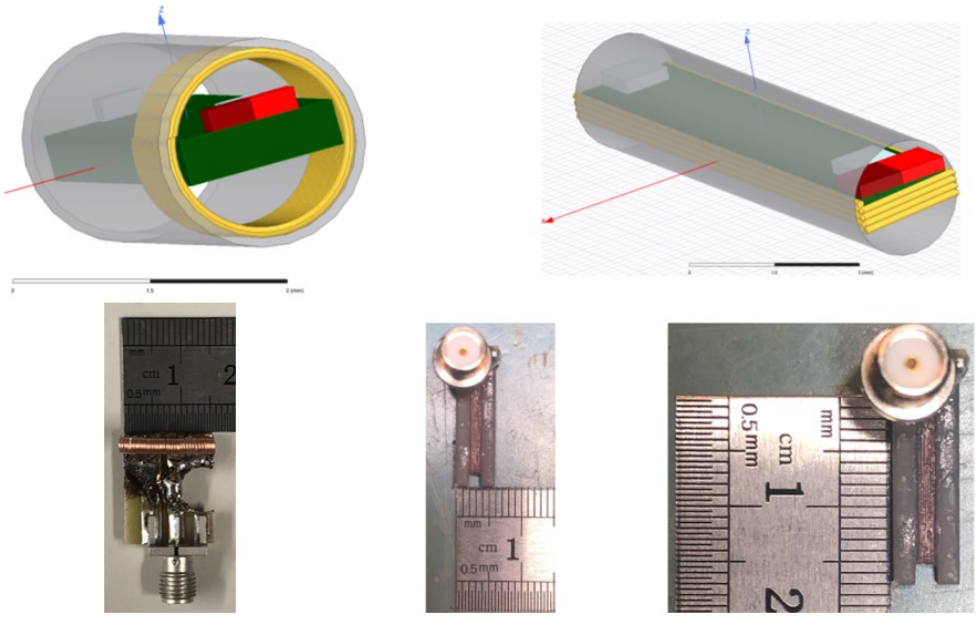

(a)

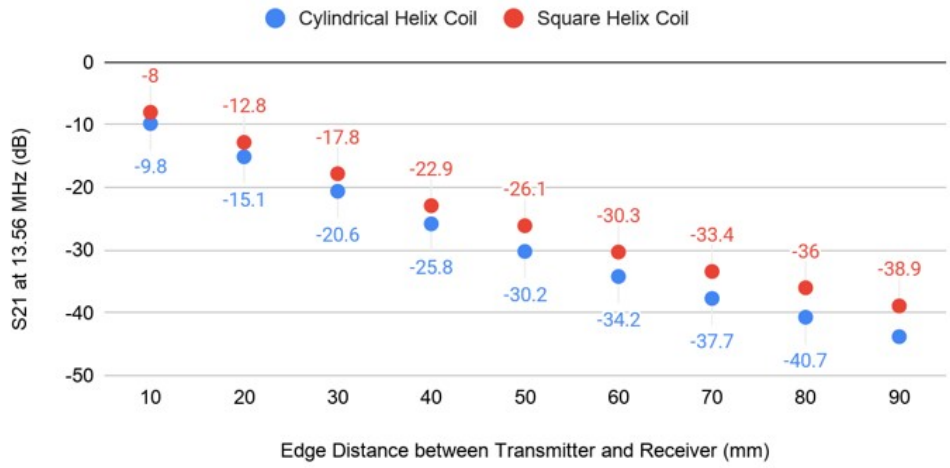

(b)

Figure 6.7: (a) Illustrating the difference between the cylindrical helix RXC (left) and the square helix RXC (right). (b) S21 comparison between the cylindrical helix RXC and a square helix RXC demonstrating a 4 dB improvement in S21 by using the square helix coil

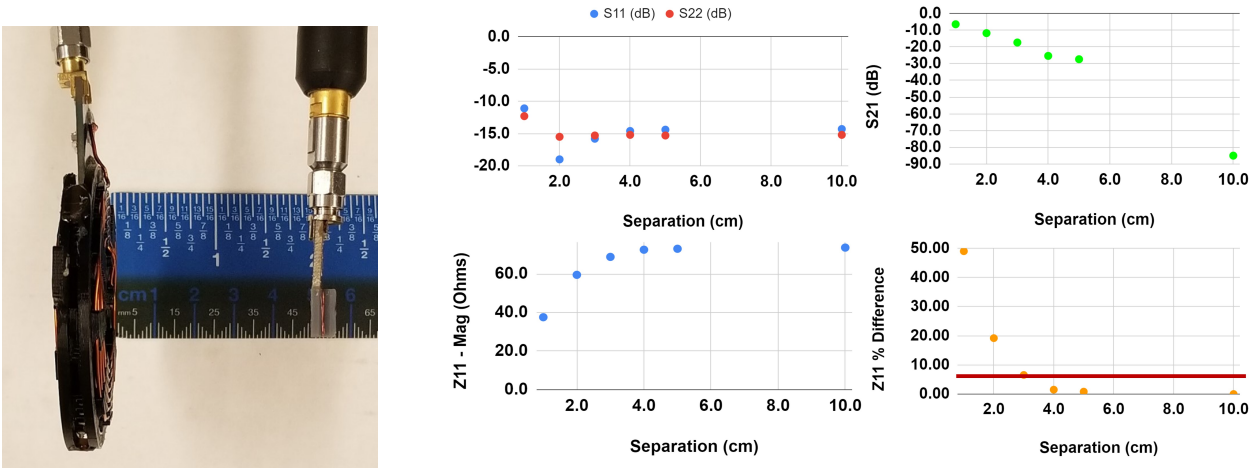

(a) (b)

Figure 6.8: (a) The TXC-RXC separation sweep experimental setup at 5cm separation (b) After sweep the RXC away from the TXC in 1cm steps, the resulting S11 and S22 (Top Left), S21 (Top Right), Z11 (Bottom Left), and Z11 Percent Change (Bottom Right)

5cm separation is nearly indistinguishable from the load modulation at essentially infinite separation (10cm). At this point the coupling coefficient is too small to modulate the TXC. In fact, when using ASK, in order to achieve the bit-error rate (BER) lower than 10^{-3}, a modulation depth of greater than $> 8\%$ is required [176]. While Z11 Percent Change in the lower right of Fig. 6.8b does not equate directly to the modulation depth, we can see that, even in air rather than through biological tissue, achieving low BER at more 2cm separation will be difficult and may require alternative communication setups.

6.4.3 Firmware and Software

Due to the modular nature of the header break-out, we were able to develop two firmware codebases in tandem. The first firmware codebase was developed using the user friendly Arduino interface. The Arduino Pro Mini 3.3V operates at 8MHz an so can drive the AFE4404, which requires at least a 4MHz clock. Through the use of this system we were able to demonstrate the actuation the two VCSELs, record from the photodiodes, log data via a serial connection to the PC, and powerdown the AFE4404 at regular intervals, providing

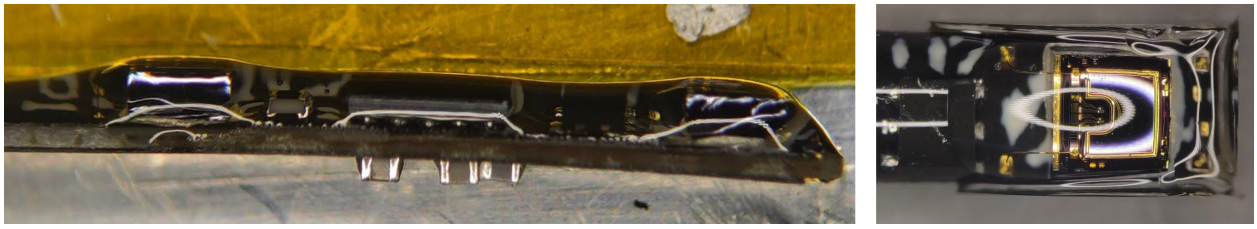

Figure 6.9: v02 - SBC Sense Board with optically clear epoxy encapsulation.

power savings. By rapidly iterating on the firmware design, we were able to get feedback from our clinical collaborators.

Lagging the work completed on the Arduino Pro Mini, a firmware suite was being set up to use the form-factor appropriate MAX32660 MCU. This codebase and IDE were less user friendly, and as such required significantly more

6.4.4 Encapsulation

This board was fully encapsulated in an optically clear, biologically compatible Norland NOA65 epoxy, Fig. 6.9, and demonstrate that the form-factor layout and component operation match closely with reference detectors within an integrating sphere, Fig. 6.6.

6.4.5 Challenges Addressed

Tin Solder Contamination of ENIPIG plated Pads

After the fabrication of the SBC v02 - Sense board was completed, the board was delivered to an assembler. The assembler proceeded to assemble the boards using reflow soldering techniques. Unfortunately, this meant that ENEPIG pads that were meant for wirebonding became contaminated with tin solder. This rendered the boards unusable, as the VCSELs and Photodiodes both required wirebond attachments and the tin/solder prevents the Au wires cannot bond to tin using the equipment we had available. Alternative explored included a replating by the fabricator, and the addition of an Au/Sn alloy. In the end, the fixes were unsuccessful, and a second run with the gold pads explicitly called out ensured that the assemblers knew the intention of the gold plated pads and as such would avoid contaminating them with tin.

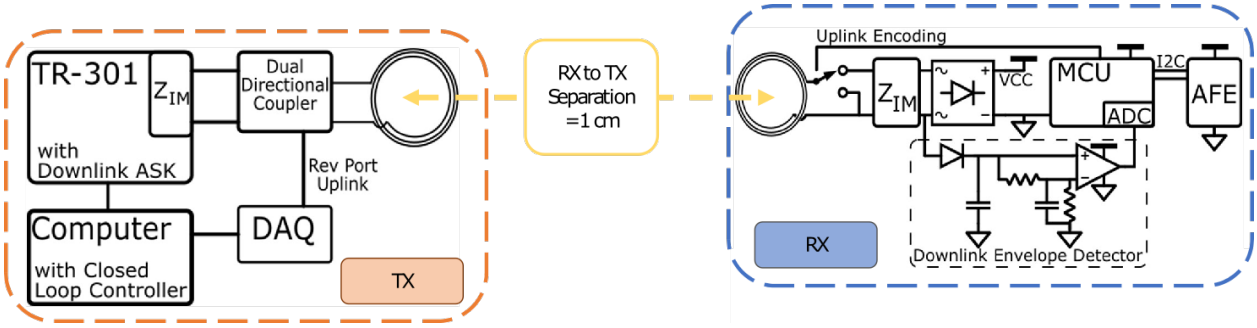

Figure 6.10: The full system overview for the non-form-factor operation of the Smart Breast Clip v03 - Power RX

6.5 Smart Breast Clip v03 - Power Board

The v03 system concentrates all of the implantable electronic components in a central 31.3 x 1.9 x 0.4 mm region which is small enough to fit into a 12G needle. This region is physically separable from the surrounding printed circuit board (PCB) carrier, which then totals 32.3 x 14.5 x 0.4 mm, inclusive of the injectable. This surrounding carrier allows for initial programming of the MCU, debugging, and testing, all accessible using the surrounding breakout pins. The v03 board represents an important derisking step in our integration and development process because it has allowed us to demonstrate full functionality in the final ultra-thin / ultra-small format (e.g., 0.4 mm thick PCB, minimum sized traces, ultra-small components) that will be used in the implant. We anticipate the design is approximately 40% longer than the final implantable version because we conservatively included additional components to increase the robustness of the wireless power and communications links, which are to be pared off to the bare minimum necessary to realize our goals.

Hardware

The essential blocks within SBC v03 board are illustrated in the block diagram shown in Fig. 6.11. In overview, the input to the system is a continuous wave 6.78 MHz sinusoidal high-frequency signal transmitted by the transmit (TX) coil, with the signal generated by the Wibotic TR-301 transmitter and received by the receive (RX) coil. The following impedance matching network (IMN) allows for both an impedance match to the RX coil as well as to the

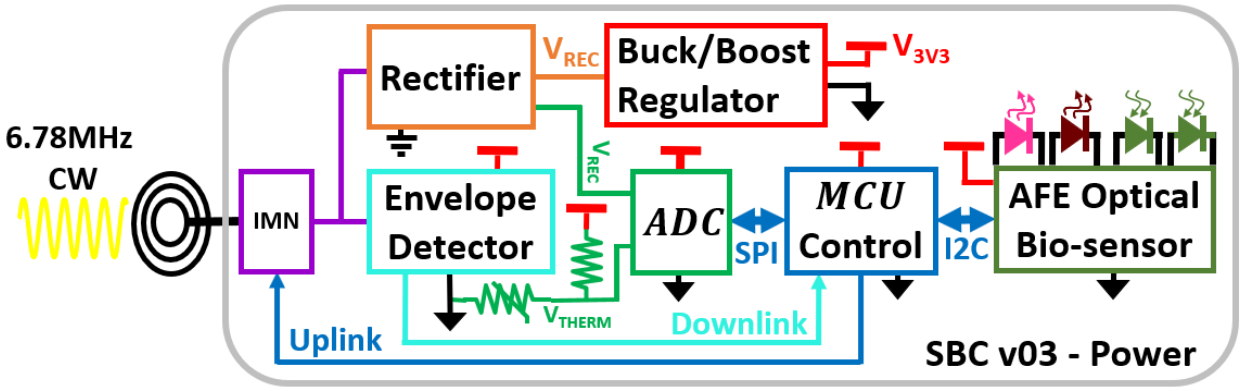

Figure 6.11: SBC v03 - Power Board block diagram.

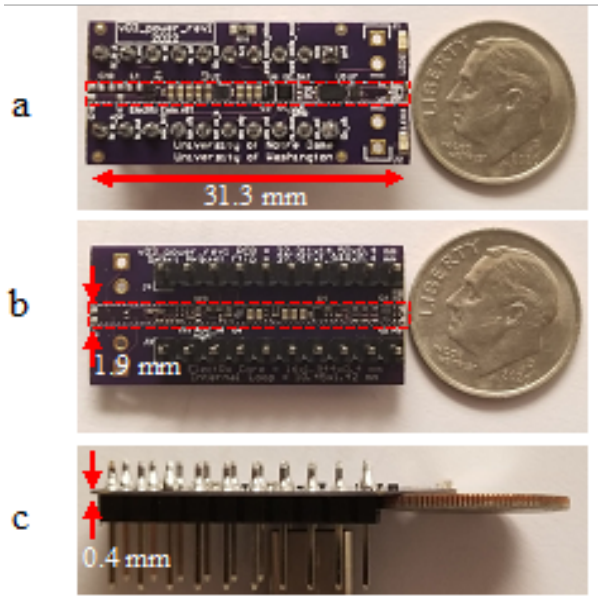

Figure 6.12: SBC v03 - Power system Top (a), Bottom (b), and Side (c) views, with injectable delineated by red dashed line.

electronic load for optimum power coupling efficiency. Proceeding along the power pathway, the bridge rectifier provides maximally efficient conversion from the HF signal driven through the IMN to provide a rectified direct current (DC) source of energy to power the remainder of the system, via storage in the tank capacitors. This V_{rec} is limited to 5.6V to protect downstream dependent components and then a Renasas ISL9120IINZ buck-boost regulator conditions the V_{rec} to a low-noise 3.3V V_{3V3}, upon which the remaining circuits depend. The primary sensor in this system is a Texas Instruments AFE4404 Optical Biosensor configured to record current excited from two Optotech PD-30040-B photodiodes, newly characterized for this system, due to the lasing of either a 850 nm or 680 nm VCSEL (OSRAM Vixar).

The recorded data (24 bits) is transmitted back to a Maxim Integrated MAX36220 MCU via I2C interface. The MCU conditions the data and packages it within a 64 bit Manchester Encoded packet. The IMN matching network is then modulated between shunt open and short according to the binary packet bits (i.e., IMN open = 0, short = 1) along the uplink pathway. Alternatively, the MCU can also uplink data communicated via SPI from the MAX19777 ADC, which in turn records at regular intervals the V_{rec} and board temperature (V_{THERM}), via surface mounted thermistor. Lastly, after the injectable has been separated from the test pin carrier and encapsulated within epoxy, no further programming of the MCU will be possible. To enable the possibility of further register changes, a modified Dickson voltage multiplier based envelope detector was included. The digital output of a Maxim Integrated MAX40009ANT+T comparator that contrasts the present rectified 6.78 MHz modulated envelope voltage to a low-pass filtered version of the envelope can be decoded within the MCU to then in turn set the appropriate register on the AFE4404.

The SBC v03 system contains the following changes and features compared to the previous non-form-factor boards:

- The Maxim Integrated MAX32660 won out over the ATTiny20 as the MCU of choice for our design. The MAX32660 is a newer 32-bit Cortex-M4 processor that has significantly more ($> 100x$) memory and lower power consumption while remaining com-

patible with the desired 12G implantable form factor. The downside is that it does not contain an analog-to-digital converter (ADC), so we also had to include a separate ADC (MAX19777) in order to monitor and regulate the received wireless power, attend to the board temperature, and receive downlink wireless communication from the external controller.

- During the PCB layout, special effort was devoted to minimizing the area of the component footprints, traces, vias and clearances in order to ensure the board would be as small as possible. At the same time, we needed to provide heat dissipation along high current pathways and reduce noise on the 3.3V V_{3V3} rail in order for the AFE4404 to record signals with high fidelity. To accomplish this, large copper pours were used and ground return pathways were carefully constrained.

- The photodiode optical detectors are a thin silicon-based photodiode (Optotech PD-30040-B). In order to save cost and time, we mounted and wire-bonded the photodiodes and the vertical-cavity surface-emitting laser (VCSEL) light sources to the PCB ourselves.

6.5.1 Coil Design

Safe, Efficient TX Coil Development

Initial designs focused on developing a coil highly efficient coil that would cover area of approximately one rodent. This resulted in a coil with a spiral resonator tuned to short and its loop tuned to 56.6 + j-10.8 Ω (2.17 nF) at 6.78 MHz and demonstrating a S11 of -18.494 dB as seen in Fig.6.13a. Unfortunately, this efficiency came at the cost of a poor match with the WPT Transmitter and under high power the coil would rapidly heat up, approaching $70°C$ even with air cooling applied, as seen in Fig.6.13b.

To address the heating concerns, additional coils were designed with resonance impedance approaching short-circuit. The optimally designed coil is shown in Fig.6.14a, the outer spiral with three turns has the dimensions of 30x20 mm and the loop is 20x15mm. The impedance

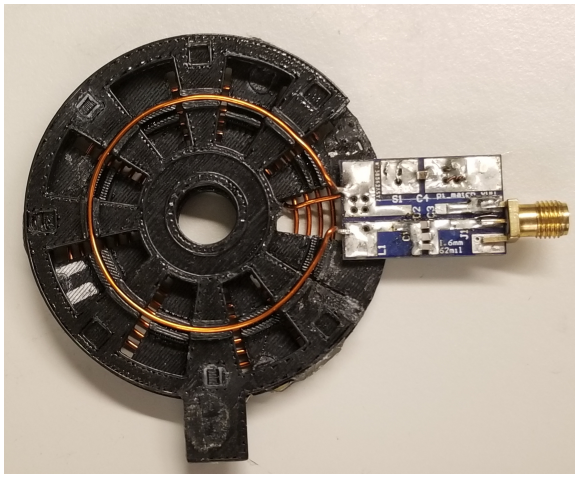

(a)

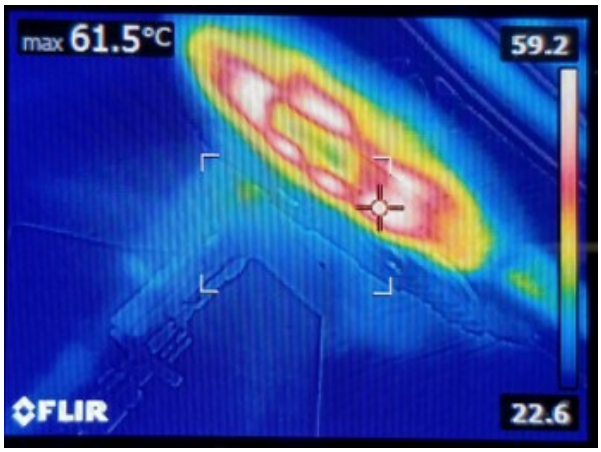

(b)

Figure 6.13: (a) The initial TX coil design with a loop of inner diameter 37 mm and and a spiral of of outer diameter 48 mm (b) Heating resulting from high power applied to the TXC.

of the coil is 2.88 + j2.8 Ω (66.21 nH) and its S11 was -3.162 dB. Despite its paltry efficiency by comparison to the prior coil, even while transmitting watts of power, this coil remained below $40°C$. In general, these two aspects must be traded off: as the S11 decreases the heating decreases, however one must then apply more power to achieve the same field strength at the receiver.

Specific Absorption Ratio Analysis of the TX Coil

An additional concern involving the design of the TX coil is its Specific Absorption Ratio (SAR) effects on tissue. The SAR heating is constrained by governmental health regulating bodies (IEEE, ICNIRP, FCC) for the general public to be 0.08 W/kg for the whole body average and 2-4 W/kg for localized SAR in the head/trunk and limbs, respectively [177]. As this is a biomedical system by relying on the magnetic field to transfer power near or within biological tissue, which has low permeability [31], magnetic resonant WPT induces less SAR heating than methods relying on the electric field to deliver the same amount of power [78]. SAR measurements in-vivo are difficult, however simulations using electrical and

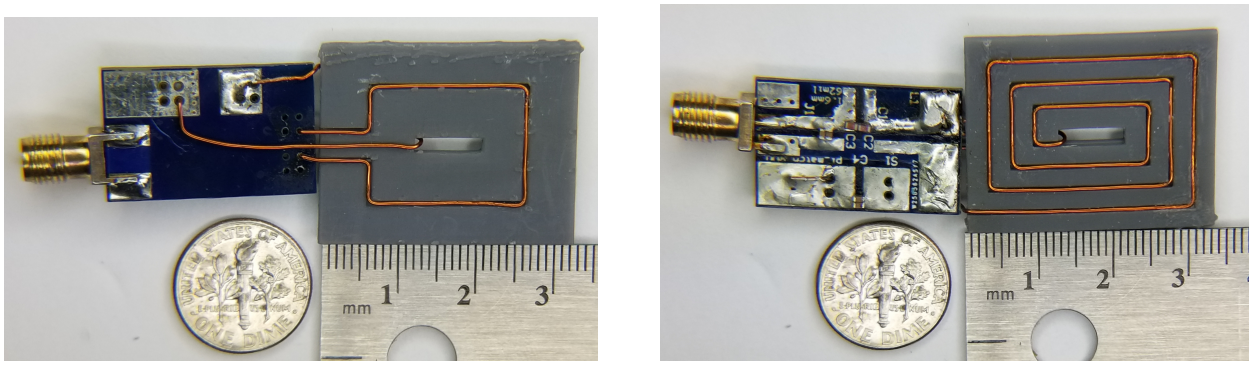

(a) (b)

Figure 6.14: The TX Coil with a 30x20 mm spiral resonator and 20x15 mm loop Top (a) and bottom (b).

thermal modeling software can accomplish the goals. The 30 x 20 mm spiral resonator and 20 x 15 mm loop TXC was simulated using ANSYS HFSS with an air gap of 1.2mm, and materials that mimic the permittivity and permeability of 35 x 35 x 1 mm of skin, 35 x 35 x 3 mm of fat, and 35 x 35 x 16 mm blood. The RXC is sized for the SBC v10 - Mouse board and has the dimensions of 15.6 x 2.2 x 0.423 mm. It is buried 10 mm from the phantom's surface. When 1.75W are applied to the coil, experimentally determined to be required for running the SBC v03 - Power board using the above coil, the resulting SAR maximum came to 0.99 W/kg, and the S21 was determined to be -15.574 dB.

Form-factor RX Coil Development

The primary design concerns for the RXC were that it would be of a form-factor to fit within a 12g needle (2.388 mm in inner diameter) and still have high-enough mutual inductance to efficient enough to power the injectable RX. 45g Litz wire was found to be a good compromise of diameter (0.0447mm) and minimizing skin effect for 6.78 MHz.

Two RXC were designed to wrap around the SBC v03 - Power and the SBC v10 - Mouse boards. The SBC v03 - Power RXC measures 30x2x1mm, has an inductance of 1 μH , was tuned to 50 Ω at resonance, providing S11 of -18.35 dB at 6.78 MHz. The SBC v10 - Mouse RXC is 16 x 2.3 x 0.5 mm, has an inductance of 568.88 nH, and a S11 of -19.1 dB

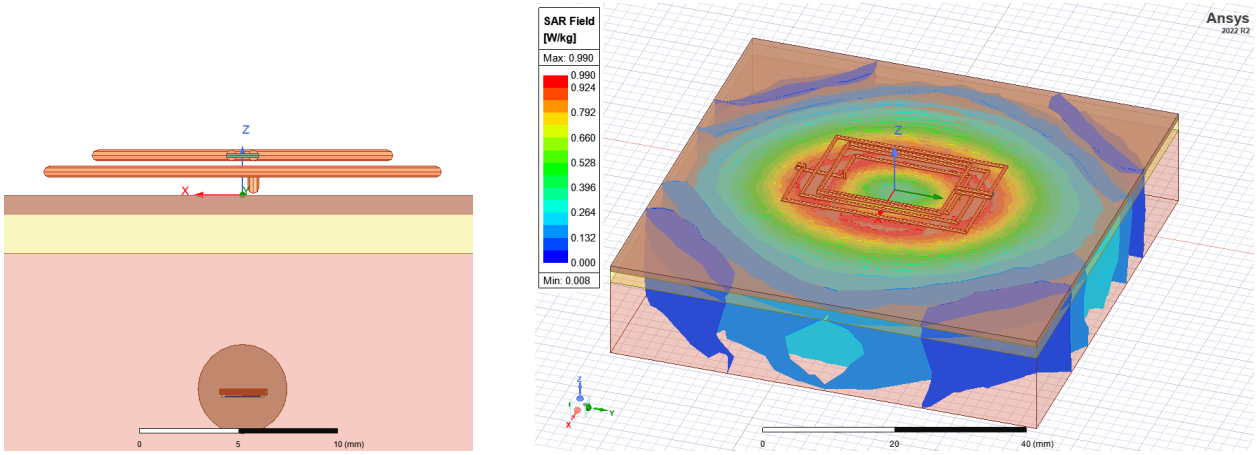

(a) (b)

Figure 6.15: (a) The Ansys HFSS model used for determining SAR Heating, including the TXC, RXC, and phantoms for skin, fat, and blood (b) The results of SAR Heating analysis after applying 1.75W of driving power to the TXC, showing a maximum value of 0.99W/kg.

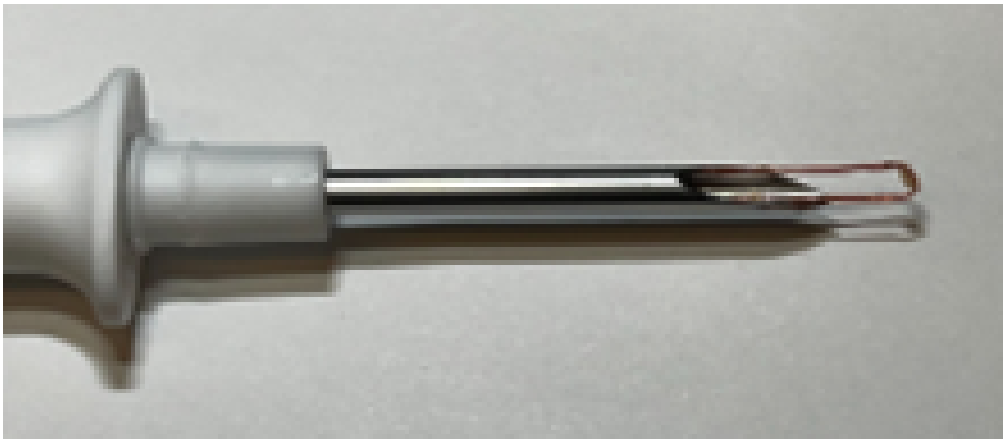

Figure 6.16: The form-factor RX Coil fitting within a 12g Needle

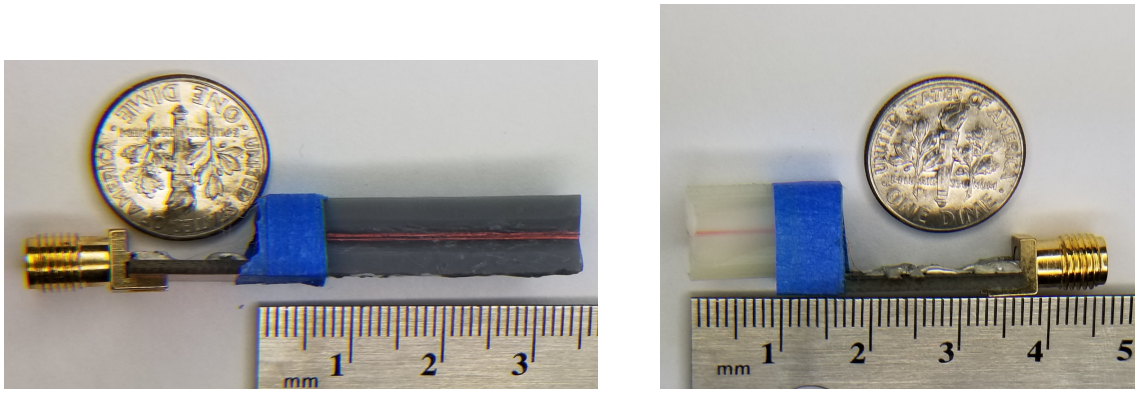

(a) (b)

Figure 6.17: The RX Coils associated with the (a) SBC v03 Power and (b) SBC v10 Mouse boards, measuring 30x2.3x1 mm and 16x2.3x1 mm, respectively

at 6.78 MHz. When paired with the square 20 x 30 mm TXC, the S21 is -13.547 dB and -15.847 dB respectively.

6.5.2 Testing Results

DC Power Consumption via V_{rec} input

The board was initially tested for DC power consumption by driving the rectified voltage with a Keithly 2401 Sourcemeter. In Fig.6.18a we see that during running operation (i.e. while processing, communication, or optical signal acquisition is occurring) the system runs at around 13.5 mW. However, due to the larger intermeasurement periods ($> 3s$), the system would predominantly exist in the sleep mode, consuming an average of 9.60 mW, a 28.8% improvement on power consumption. Towards the high end of the supplied V_{rec}, the power increases dramatically, this results from the protection Zener diode, which was selected to limit V_{rec} to 5.6V, so as to protect the input of the ISL9120 Buck-boost Regulator.

Start-up Current Draw

While in general operation the intention is to keep the rectified voltage well below the Zener limit of 5.6 V, and the ISL9120 regulates V_{rec} to 3.3V most efficiently around 3.6 to 4V, so in this test we target 4V as a running power. This running and sleep power requirements

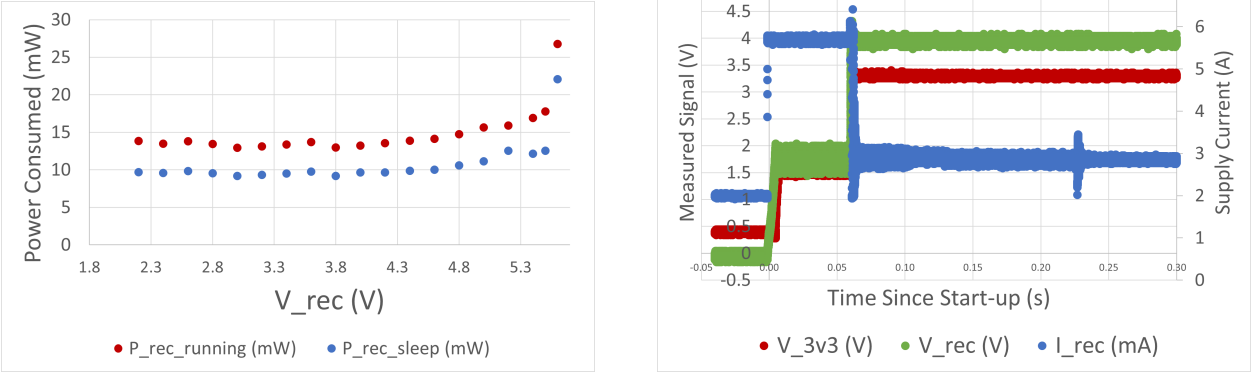

(a) (b)

Figure 6.18: (a) The power consumed by the SBC v03 - Power board during full operation and then during sleep, demonstrating a 28.75% reduction in power consumption while sleeping. (b) An example of the start-up voltage sequence and showing the required current on the right hand axis for the SBC v03 - Power board

are actually quite low, when compared to the instantaneous power required to start-up the system. As shown in Fig. 6.18b, the instantaneous current requirement is nearly 25% higher than the running current during the first tenth of a second after start-up. This presents a problem, as the ISL9120 Buck-boost can begining to supply the 3.3V rail as low as 1.8V, however if not enough energy has been stored in the capacitors, the turn-on current draw will pull the tank capacitors to 0V, thereby shutting off the regulator and shutting down the system as a whole. Without a start-up circuit, which would take up valuable real-estate on this space limited board, the alternative is that the initial transmitted power, must jump this oscillation point in order to deliver energy exceeding that required for start-up. This results in another issue though, as the higher transmitted power can overheat the TXC coil, and it stresses the protection Zener diode. The diode was selected specifically to handle upwards of 250mW (almost 20x the running power), however V_{rec} high enough to engage the Zener is also wasted energy that is just going towards heating up the RX.

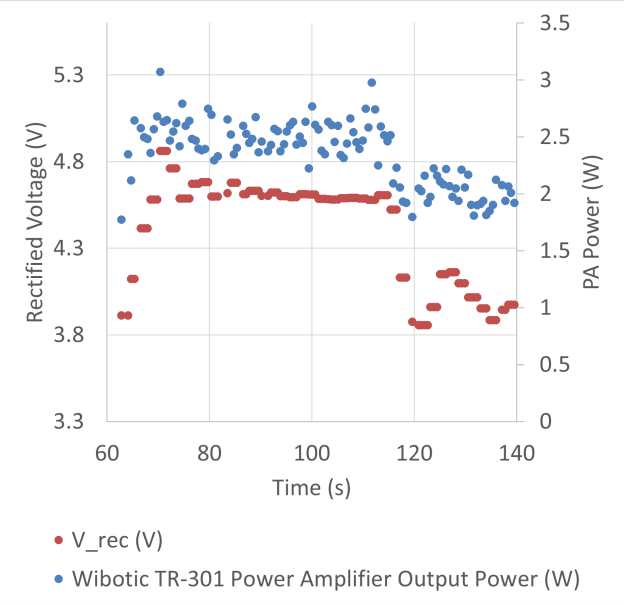

Figure 6.19: An example of the rectified voltage being regulated towards the target voltage of 4V.

V_{rec} Closed-loop Regulation via Uplinked V_{rec} Measurements to the TX Controller

Considering these issues, the rapid regulation of V_{rec} measurements by the RX via uplinked feedback to the WPT transmitter would benefit the operation of the electroceutical immensely. In Fig. 6.19, the transmitted power is stepped up rapidly until the RX unit is capable of turning fully on, in this case at 3.913V and with an WPT Power Amplifier output power of 1.774W. The system is then ramped up to V_{rec} = 4.6V, which serves as a High Power level for our downlink communications, oscillating across the target using lower and lower step sizes until the transmitter can get the V_{rec} no closer, at around 95s in the graph. The setting associated with this power level is saved and then the system descends rapidly towards the target running V_{rec} voltage, 4V. Again the TX system oscillates at lower and lower step-sizes according to the closeness to the target voltage as uplinked by the RX. The target is reached at around 138 s, and the system then shifts to the next state in the state machine.

Bit Error Rate Testing with 5 mm Separation in Air

As a final test of the system, the optimized TXC and the SBC v10 Mouse coil were separated by 5 mm of air, and the system was run in fully automated mode for a total of 23 min. During that time the system regulated the power to the target voltage, and then cycled through 3 states for one minute each. At the target running voltage the power transfer efficiency ($\frac{P_{rec}}{P_{TX}}$) was 0.496%. In the first state, Sensor Report, the AFE4404 reports its readings on at a given frequency (e.g. 0.3Hz), with intermittent reports from the MAX19777 ADC of the V_{rec} voltage as well as the recorded thermistor temperature. In the case of this experiment the AFE4404 data was hard coded for comparison and achieved 100% accuracy the intended "readings".

After the minute of reports has elapsed, the system switches into the Downlink Bit Error Rate testing state, where a 52bit packet is transmitted at 10bps using ASK modulation. The RX buffers the packet, decodes the packet from Manchester encoding, saves the result, and then reverses the process by encoding the packet with Manchester Encoding, then uplinks the data back to the DAQ unit. To mitigate the possibility that poor uplink bit error rate corrupts the originally downlinked packet, the single packet is uplinked multiple times (50x in this case), and then the mode of those packets received by the DAQ is recorded. During this experiment 41 packets were processed of 80 transmitted, for a packet error rate of %51.3. The other packets were either not registered by the RX or the firmware determined that the preamble was did not match the necessary 16b clock, and so threw out the packet in order to be prepared for the next packet. The intrapacket BER had a final running average of $1.68 * 10^{-8}$%, with only a single packet being erroneous by 13 of the 52bits.

The final state of the system is uplink BER testing, as the datarate is high for uplink, in the same span of time, 538 packets were transmitted. In that period, the BER came to 0% without a single mistaken packet.

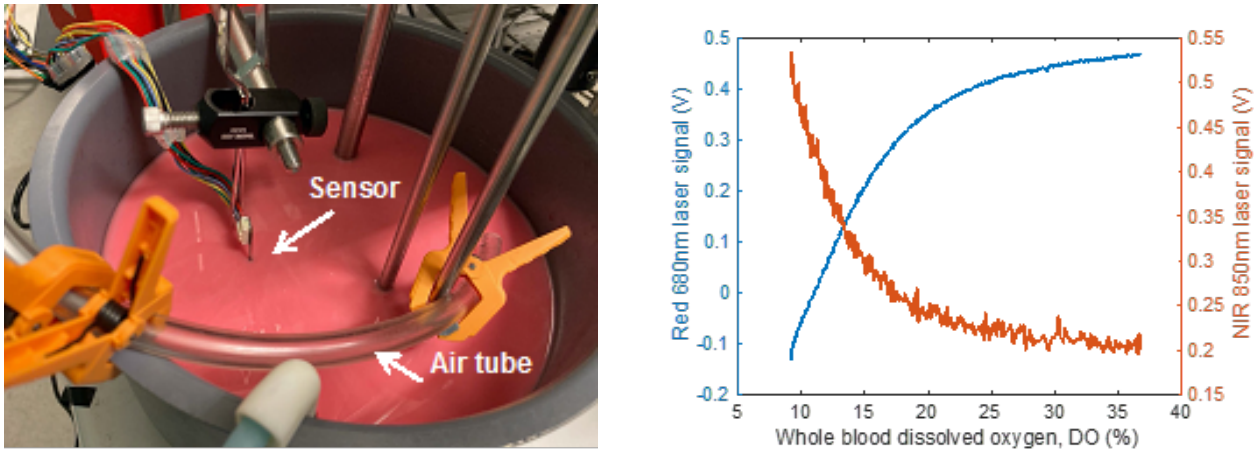

(a) (b)

Figure 6.20: (a) Blood oxygenation phantom used to test the how the prototype sensor responds to changing blood oxygenation (b) SBC v03 - Power data while monitoring whole blood phantom during reoxygenation during wired operation

Blood Oxygenation Phantom Testing using wired Form-factor SBC v03 - Power Board

The SBC v03 - Power was used to monitor the change in blood oxygen saturation in vitro while the partial pressure of oxygen in the blood mixture was altered (Fig.6.20a). After optimizing the laser power, detector gain, and sampling time, we observed clear expected responses at both laser wavelengths to the reoxygenation of the phantom (Fig.6.20b). Specifically, as deoxyhemoglobin becomes oxyhemoglobin with increasing dissolved oxygen (DO), the detected signal increases at 680nm due to decreasing absorption. Similarly, the 850nm signal decreases with increasing optical absorption from the oxyhemoglobin, albeit to a lesser degree. This is because 680nm optical absorption is much more dependent on the oxygen saturation than 850nm.

Blood Oxygenation Intralipid Testing using Wireless Form-factor SBC v03 - Power Board

Lastly, referring to Fig. 6.21, the SBC v03 - Power board was used to measure the optical absorption change through a controlled intralipid tissue-simulating phantom by varying concentration of nigrosine ink within the phantom. The system was operated completely

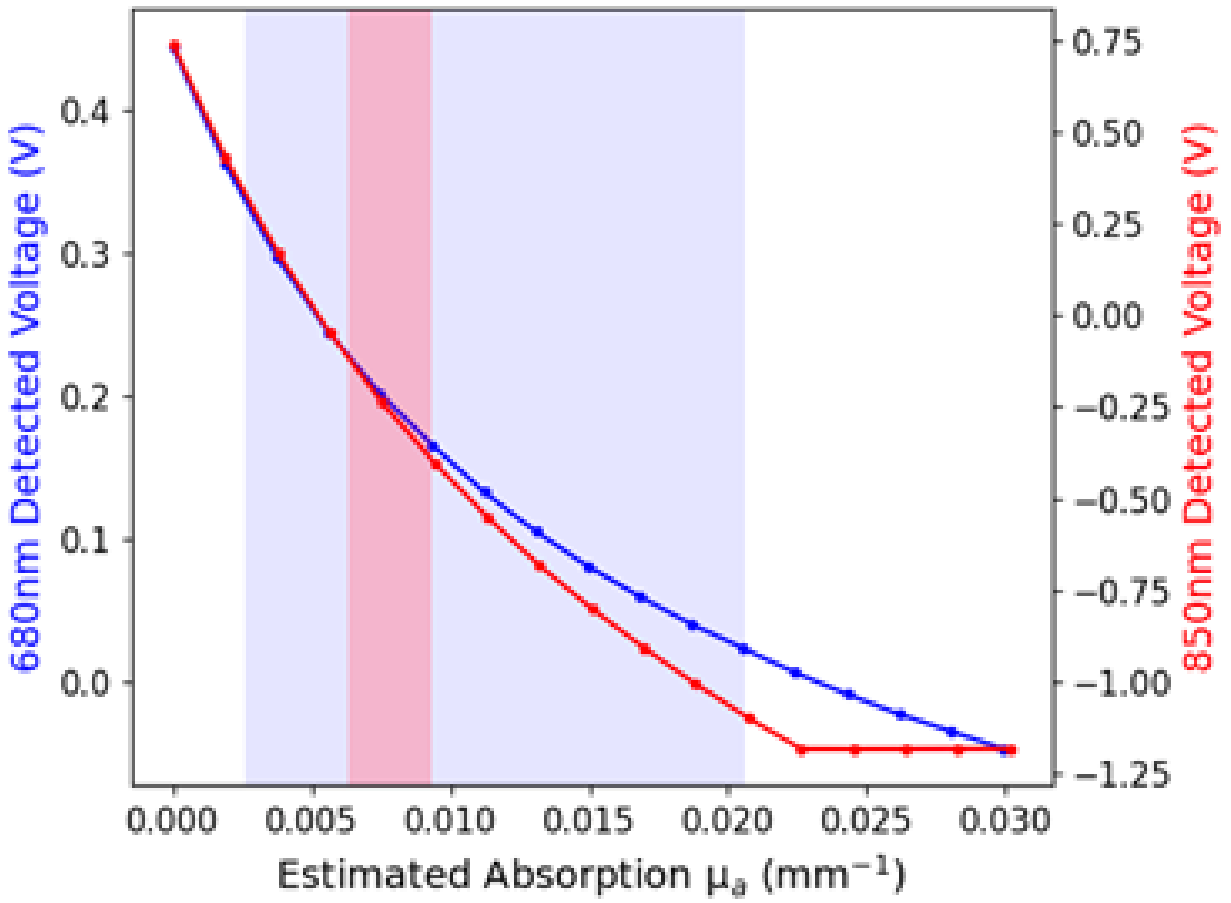

Figure 6.21: The SBC v03 - Power data during fully wireless operation while measuring controlled intralipid solutions with varying optical absorption. The blue and red shaded regions represent the expected optical absorption for 680nm and 850nm, respectively, that will be encountered in tumors in vivo.

wirelessly using non-form-factor coils mounted externally to the phantom in order to demonstrate functionality.

6.5.3 Systems Automation and Communication - Non-form-factor

A block diagram of the wireless power, communication, and data transfer subsystems is shown in Fig.6.10 for the non-form-factor full system design. The TR-301 wireless transmitter drives a continuous wave sinusoid at 6.78 MHz through a dual directional coupler and into the TX coil. The waveform is coupled into the injectable RX across 1 cm separation via

the adjacent RX coil. The RX coil is impedance matched to the load via the Z_{IM} and the resulting HF signal is rectified to provide continuous power for operation of the RX. When the sensors provide data to be wirelessly transmitted (i.e. uplink), the MCU modulates Z_{IM} between short and load, causing the load on the TX coil to change. This change is relayed to a data acquisition (DAQ) unit on the external host computer via the dual directional coupler. The computer connected to the DAQ decodes the signal and operates the TR-301 according to the flow chart shown in Fig. 6.22.

One benefit of this feedback path is that the V_{REC} can be limited programmatically, providing a closed-loop V_{REC} regulation for minimum power transmission and safe operation. For example, if the RX senses the V_{REC} is approaching the 5.6V Zener diode enforced limit, the uplinked data can instruct the TX system to reduce the transmitted power. In an emergency situation, for example if the temperature of the injectable was beyond safe limits, the RX can rapidly uplink to the TX system shutdown instructions, then the RX can detune the IMN so that power received is immediately reduced.

In order to take advantage of the MAX32660 and AFE4404 maximum energy savings, the systems are put to sleep between measurements. Using a programmable inter-measurement period, this results in less than a 2% duty cycle. During start-up and measurement, the state machine of the RX is shown in Fig. 6.23. Essentially, any time the RX is waiting for a result, the RX is put into a low power sleep state. When not asleep, the RX exists in one of two stages during start-up (V_{rec} regulate and polling the downlink for AFE4404 register updates), and then continuously uplinks data after start-up is finished. By maximizing time within these sleep states, reducing the clock frequency, and using low-power flash writes, the average power consumption was reduced from 37.2mW to 9.6mW, a nearly 3.9x power reduction.

Uplink

To record and respond to sensed data on the RX via a DAQ acquired uplinked packet resulting from LSK modulation of the TX Coil, the following uplink algorithm in Alg. 1 was

deployed on the Client Controller. Each packet contains $Nbits$, where the first $kbits$ are a clock signal serving as the preamble (e.g. the first 16 bits) and the remaining bits are the Manchester encoded data. For example, the AFE4404 has a M bit (e.g. 24bit) ADC reading to transmit, Manchester encoding doubles the data packet to 2*M (= 48b), and assuming the packet is 64b, this leaves the preamble length equal to N-2*M, or 16b in this example. The key attributes of the algorithm include:

- The DAQ acquisition transfer rate is significantly slower than the processing rate, so a Producer-Consumer Model to allow for consumer thread processing, while the producer actively acquires the next acquistion frame (e.g. 100 $kSamples$ recorded at 2.5MSPS)

- Any given DAQ acquisition may or may not have a packet within it, so a Packet Detector finds the sequences in the data where power within the enveloped is greater than a user set $UPLINK\_IN\_ACQ\_RATIO$

- Once a packet is detected (one of possibly multiple within a given acquisition), the packet is digitized and the indexes of the zero crossings are determined. The period between the zero crossings is then the bit length of a given bit within the packet.

- The preamble provides a Single Bit Length reference, from which the remainder of the packet can be segmented

- The segmented array is then passed to a Manchester Decoding function and the original M bit data can be processed as necessary

To demonstrate the uplink functionality, the 4.7cm loop + spiral resonator tuned to 50 Ω resonance at 6.78 MHz was separated from the Wibotic RC-100-AP-ST resonator by 1 cm. Once the v03 board stabilizes to V_{3v3} = 3.3V, a 64 bit packet consisting of a Manchester encoded 0x1 was transmitted from the RX to the TX. In Fig. 6.24a, which zooms in on the first 16 bits (i.e., the preamble) of the 64 bit data packet, the signal modulating

Algorithm 1 Manchester Decode - Uplink - Client-side Processed in Python
Result = Manchester Decoded or Null Packet

Require: Single Acquisition Window of of the RX Load Shift Keyed Manchester Encoded data series consisting of N bits, each separated by T seconds, where the Impedance Match network Short, represents a digital 0, and otherwise a digital 1 is assumed.

procedure ACQUISITION PRODUCER THREAD
    $acquisition \leftarrow$ 100 kSamples from the DAQ once every $\approx 580ms$
end procedure

procedure ACQUISITION CONSUMER THREAD($acquisition$)
    $acq\_conditioned \leftarrow acquisition$ centered and butterworth low pass filtered
    $acq\_envelope \leftarrow |envelope(acq\_conditioned)|$
    $acq\_peaks \leftarrow$ Kth Highest Percentile of acq_envelope
    $UPLINK\_IN\_ACQ\_RATIO \leftarrow$ minimum difference in envelope amplitude for a packet to exist within the acquisition
    if $\frac{acq\_peaks}{acq\_envelope} > UPLINK\_IN\_ACQ\_RATIO$ **then**
        Uplinked data in the $acquisition$
        $uplink\_packet \leftarrow$ Centered acq_peaks
    end if
    if Uplinked Packet exists with $acquisition$ **then**
        $uplink\_packet\_dig \leftarrow uplink\_packet > 0$
        $uplink\_bit\_array \leftarrow$ Zero Crossing Indexes of $uplink\_packet\_dig$
        Manchester Decode $uplink\_bit\_array$
    end if
end procedure

the RX IMN ($VIMN_{MOD}$) toggles from 0 to 3.3V. This opens and shorts the N-Ch MOSFETs, respectively, within the IMN. The resulting change in the peak-to-peak voltage on the high frequency negative input line (VHF_{NEG}) can be seen to be an inverted version of the modulating signal as the HF_{NEG} and HF_{POS} lines are toggled between being shorted and disconnected. The resulting change in impedance of the RX coil then modulates the TX coil inductance through the mutual inductance between the two coils. The impedance change of the TX coil can then be seen to change the peak-to-peak voltage of the signal coupled to the reverse coupled port of the dual directional coupler (V_{UPLINK}). The 12% modulation depth provides sufficient fidelity for decoding data and the system was able to transmit at a intrapacket datarate of 109.659 $kbps$, or 9.12$\mu s/bit$. Due to the use of the Tektronix MSO3034, the interpacket duration can be considerably long (as described at the beginning of this section), but by uplinking multiple packets within a single acquisition window (up to 7 at 64b per packet) allows for a total throughput of 10.214 $kbps$.

The recorded V_{UPLINK} is then digitally conditioned and resulting final 64 bit digitized binary output is shown in the bottom-most subplot in Fig. 6.24b. After stripping the signal of its preamble and applying Manchester Decoding, the signal sent matched the input perfectly, demonstrating error-free communication.

Downlink

To downlink information from the TX to the RX, two alternatives have been investigated: using the envelope detector or directly using the recorded VREC. In both cases, the TR-301 drives the TX coil using amplitude modulation (ASK) resulting from a Manchester encoded 64 bit data packet.

First, focusing on the envelope detector downlink alternative, the comparator has direct input to its non-inverting terminal of the enveloped signal (VENV) and then the inverting input senses a (severely) low-pass filtered version of the envelope ($VENV_{LPF}$). This results in the VENV signal at any given moment being compared to a signal that has a very slow rate of change ($1/\tau_{LPF}$). When the input signal to the RX coil changes fast enough and at

the right amplitude, VENF crosses the $VENV_{LPF}$ and the comparator (VCOMP) toggles. In Fig. 6.25a, we see this process in operation. The input signal in this case was a 64 bit packet with 26 bit toggles being displayed in the figure, and shows the downlink operating at 169.4bps. Additionally shown in the figure is the rectified voltage, which maintains an average of 4.62V. This demonstrates that the ASK modulation depth is small enough that the stored energy in the V_{rec} tank capacitors is not diminishing below the target V_{rec}.

While testing the ASK capabilities of the TR-301 transmitter it was found that, depending on the TX ASK modulation depth, the minimum toggle duration for a single bit is around 4.5ms, resulting in a maximum data rate of around 213bps. The rise and fall time of the charging of V_{rec} is around 40% of this, so it was determined that the V_{rec} signal itself could be used as the downlink signal source. In Fig. 6.25b, we see that the V_{rec} signal on the RX, driven by the transmitted power ASK modulation, alternates between 3.88V and 2.64V with a bit duration average of 5.016ms, resulting in a 200bps data rate. Using the ADC that is already measuring the V_{rec} signal, perfect decoding of Manchester encoded packets was possible.

To record and respond to transmitted data from the TX via ASK modulation of the TX Transmitted Power, the following downlink algorithm in Alg. 2 was deployed on the Client Controller. As with the uplinked data, each packet contains $Nbits$, where the first $kbits$ are a clock signal serving as the preamble (e.g. the first 16 bits) and the remaining bits are the Manchester encoded data. The key attributes of the algorithm include:

- This algorithm needs to work at runtime, since the resources for complex math and storage of vast data arrays are not available to a resource restricted MCU

- Any given transition in the amplitude could be an edge at any point within the transmitted packet, so, if the fragility of hardcoding the bit and packet lengths is to be avoided, careful attention must be paid to reset and edge counting. This includes the possibility that a packet padded out to the expected packet size when there is no transition between the before last transition and the end of the packet (for example, if the

4th to last bit in the packet was a high to low transition of the TX output power, and the remaining bits were all low (e.g. if the last for bits of the packet = ...1000), then the downlink algorithm must pad out the packet, knowing the average bit length as discovered from the preamble.

- The preamble provides a Single Bit Length reference, from which the remainder of the packet can be segmented

- If a given preamble does not follow the standard clock signal (e.g. 0101010101010101), then the packet is thrown out

While the data rate achievable by the envelope detector downlink block could be significantly faster than using the ADC to measure the V_{rec} signal, because of the large tank capacitors required for energy storage for the system and therefore large τ_{CTANK}, the envelope detector requires 10x components and significant area on the PCB for the trace distribution. As the ADC measurements of the V_{rec} signal is already required for closed loop operation of the v03 system, and fewer components would reduce both the area usage as well as power consumption, it was decided that future revisions would not include the envelope detector unit.

6.5.4 Systems Automation and Communication - Form-factor

In the process of scaling down the system and paring back safety mechanisms, it was discovered that the modulation index that would be driving the LSK modulation detection became too small for reliable detection, essentially the impedance change of the with respect to the source impedance was resulting in a VSWR that was little different than the non-modulated VSWR.

LSK modulation depends on a change in the impedance of the RX being reflected back to the TX through their mutual inductance, as diagrammed in Fig. 6.26a. The modulation

Algorithm 2 Manchester Decode - Downlink - Runtime in Embedded C
Result = Manchester Decoded Packet

Require: TX Amplitude Shift Keyed output of the Manchester Encoded data series into N bits, each separated by T seconds, where from low to high, represents a digital one, and high to low, represents a digital 0

Signal Input $\leftarrow V_{rec}$ amplitude modulated via the ASK signal transmitted by the TX
$vrec\_sample \leftarrow$ ADC Ch2 sample of the the V_{rec} at a sample rate of ≈ 660 *bps*
$PREAMBLE\_LEN \leftarrow$ User set, e.g. 16bits
$MIN\_LEVEL\_DIFF \leftarrow$ Expected Minimum Amplitude Modulation Level Difference
while downlink_duration < DOWNLINK_DURATION_MAX **do**
    if $|vrec\_sample - v\_rec\_avg| > MIN\_LEVEL\_DIFF$ **then**
        $edge \leftarrow Detected$
        $vrec\_avg \leftarrow vrec\_sample$
    end if
    if *edge* is Detected **then**
        $bit\_len \leftarrow$ Present Time $- transition\_time\_start$
        $bit\_len\_array[++ii] \leftarrow bit\_len$
        $transition\_time\_start \leftarrow$ Present Time
        if preamble_complete == True **then**
            $bit\_len\_avg \leftarrow$ Average of previous K bit lengths
        end if
        if packet_complete == True **then**
            $downlinked\_packet \leftarrow bit\_len\_array$ divided into N equal periods
            Manchester Decode the Packet
        end if
    else
        $vrec\_avg \leftarrow$ Average Previous N Samples
        Increment sample count
    end if
end while

index is expressed as a percentage of the modulation:

$$m = |\frac{V_{L1} - V_{L1Modulated}}{V_{L1} + V_{L1Modulated}}| \tag{6.1}$$

Following similar similar line of analysis as that in [178], we want to determine how the modulation depth is affected by changes in Z_2:

The impedance of the TX and RX circuits can be found as follows:

$$\begin{aligned} Z_1 &= \frac{V_1}{I_1} = R_1 + Z_{r2} + j[\omega L_1 - \frac{1}{\omega C_1}] \\ Z_2 &= \frac{V_2}{I_2} = j\omega L_2 + (j\omega C_2 + \frac{1}{\omega R_2})^{-1} \end{aligned} \tag{6.2}$$

If we assume the two coils to be resonant, then Z_1 and Z_2 are purely resistive, thus:

$$Z_2 = \frac{L_2}{R_2 C_2} \tag{6.3}$$

Z_2 can be related to Z_{r2}, the reflected impedance seen by in series with the TX coil, via M, the mutual inductance between the two systems:

$$\begin{aligned} Z_{r2} &= \frac{(\omega M)^2}{Z_2} \\ M &= k(L_1 L_2)^{1/2} \end{aligned} \tag{6.4}$$

Where k is the coupling coefficent as defined by geometrical parameters. Solving out gives us the impedance and voltages across the TX coil:

$$\begin{aligned} Z_1 &= R_1 + (\omega k)^2 L_1 C_2 R_2 \\ V_{L1} &= \frac{V_1}{\omega C_1 (R_1 + (\omega k)^2 L_1 C_2 R_2} \end{aligned} \tag{6.5}$$

Referring back to Eq. 6.1, we can see that if the coupling coefficient is small then even significant changes in R_2 would result in little ΔV_{L1}. This difficulty with a minimal change

is further compounded by the 30 dB coupling from the output port to the reverse port for the Werlatone C10195-12 4-port Dual Directional Coupler, essentially dropping the VSWR into the noise floor of the DAQ. Were we using large signals such that V_1 could provide some gain, the signal might be saved via appropriate gain, envelope, and filtering. Unfortunately, the TXC power input must be limited to decrease heating, and additionally the RX itself doesn't require more than $\approx 10\ mW$ deliver HF power.

There are multiple ways to address this problem, however, the most accessible was to couple the LSK signal from the TXC to what is referred to as TXA in Fig. 6.26b. Essentially TXA is sized to match TXC, and offset along the TXC axis on the opposite side of TXC from RXC, and contains a loop + resonator structure tuned to around 25 Ω at 6.78 MHz resonance. After feeding the signal coupled into TXA through and envelope detector and measuring the result on the DAQ, the higher coupling coefficient and high Q allowed for around a 10x improvement in modulation index, thus enabling the continued use of all the infrastructure and codebase already in place, but now with form-factor coils.

As an additional check, to confirm that the signal acquired by the TXA was due to electric field coupling between the RX and TXA a biological phantom of 2 mm was place between the RXC and TXC, with the expectation that the E field would deteriorate rapidly in the tissue substrate, but the B Field would be sensed barely impeded. The signal reduced but did not disappear. Additionally, because of the large separation between the TXA and RX coils ($\approx 3cm$), M_{32} would be inconsequential as B field was in near field WPT falls off at $\frac{1}{d^3_{separation}}$.

6.5.5 Challenges Addressed

Low Yield

The initial fabrication of this board resulted in a yield of only 50%. In the design of the board we were pushing the capabilities of the fabricator, so a low yield was expected. However, for future revisions, we made sure to provide buffer around traces that may have caused shorts and used larger vias wherever possible.

Dicing

The initial plan was to have the assemblers dice the boards down after they had been programmed, in order to reshape the board down to the to the 1.811 mm injectable form-factor width. Unfortunately, the minimum dicing tolerance of the assemblers, and minimum cut tolerance of the fabricators,was higher than we could tolerate, since the outermost pads of the BGA devices and outermost traces (already minimized to the minimum fabricator capabilities of 3mil trace width/3mil separation and filling every available planar area), would likely be cut severely reducing the yield. We instead investigated methods of removing the injectable from the carrier by hand. We first attempted to dice with wire cutters and a scalpel, however both of these methods caused significant bend in the 0.4 mm PCB and lacking this rigidity we were concerned that the BGA balls and internal vias could become disconnected in the attempt. We also attempted lasing the board away from the carrier. As can be seen in Fig.6.27 though, this resulted in many of the top and bottom traces delaminating from the surface. In the end, it was decided that the best method to proceed with reducing the a board down would be return to the prong form-factor of the SBC v02 - Sense and to carefully (and safely) file/sand away the area that prevents the system from being encapsulated.

Start-up Consistency

Do to the limited space for traces and the need to minimize both the size and count of components, multiple pins for the various ICs were routed to single pins on the MCU, thereby multiplexing the functionality of a given pin. During the design phase, the contention between the pins was tested for and didn't cause problems. After fabrication though, it was found the pins involved in programming the board could be easily interrupted during the start-up phase of the programming. For example, the SWDIO pin of the MCU was also used to control the MISO pin of the MAX19777 ADC. The reasoning being, after initial programming of the MCU, that pin becomes free and with only 10pins on the package, each pin needs to carry additional tasks. As programming begins though, and while the MCU

proceeds through setup, the MCU will trigger the enabling CS_B pin on the MAX19777, thus causing the ADC_{MISO} output to enter contention with the programmer. We were able to side-step this issue by shorting the CS_B pin during any programming (sinking 10s mA of instantaneous current in the process), but the lesson was valuable. In future revisions, pull-up and pull-down resistors were employed for providing start-up consistency. While these loads offer an additional path for current draw, the benefits of a operational board far outweigh the loss, and if these start-up support components are unnecessary, they can be removed.

Coil Design with 45g wire

An interesting aspect of designing these coils has been determining a method of creating a frame for tuning the coils and testing the coils that can then be removed after the tuning has been completed. To address this issue, the mold was created from water soluble, 3D printed PVA. After wrapping the coil and securing it with glue, the coil is tuned. The PVA is then dissolved allowing for the coil to be placed in position on the injectable.

High Component Count

One of the key purposes of the SBC v03 - Power PCB was to provide redundancy and flexibility in the form-factor shape, before paring away components for the final deliverable SBC v10 - Mouse PCB. As can be seen from Fig. 6.28, 41 components were removed, freeing up significant top and bottom board realestate for component footprints and simplifying the layout. The space savings would enable the SBC v10 Mouse to approach the targeted 1cm in length.

6.6 Smart Breast Clip v10 - Mouse Board

The v10 - SBC Mouse Board design has been educated by our experience with the prior boards. This unit is sized such that it will be able to be injected within a murine model using a 12g needle to demonstrate that wireless smart breast clip microimplants, which are similar in size to standard breast radiological markers, can provide continuous functional sensing within tumors. After reshaping, the injectable portion has planar dimensions of 15.444 mm

x 1.811 mm, and allows for the addition of a 45g wire wound coil surrounding the board to fill out to the diameter of 2.159 mm of a 12g needle. To ease testing, prior to the reshaping the board has planar dimensions of 15.647 x 2.216 mm, allowing for the board and coil to be encapsulated and mounted within an 11g needle (inner diameter = 2.388 mm). Including the carrier the total dimensions are 24.661 x 13.108 x 0.4 mm. Castellated holes at the tip of the prong allow for the attachment of a coil that would be folded over the top of the injectable to be encapsulated as a single unit. The coil can be tuned via a L-Match, with a Pi-match capable of being hacked into the pads if necessary. There is one additional tuning capacitor located at the opposite end of the board for the purposes of tuning a co-encapsulated repeater coil with the PCB and main coil.

Hardware

Starting from the HF Input area and proceeding through to the analog sensing components, the SBC v10 - Mouse was designed with the following constituent components:

- Full-wave Bridge Rectification via CDBZC0130L-HF Schottky Diodes capable of 100mA forward current and with a forward voltage of 370 mV
- 5.6V Protection Zener Diode capable of sinking 250mW of power
- Tank Capacitance for Rectified DC Energy Storage = 110.1 μF (expandable to 235.1μF, if 0402 47μF capacitors are used)
- Uplink Modulation NMOS Transistors capable of 1.5A continuos I_D
- ISL9120 Buck-boost Regulator with an input range of 1.8 to 6.5V and outputting 3.3V
- MAX19777 Low-power 2ch 12bit ADC capable of up to 3Msps sampling rate
- Board mounted thermistor for temperature measurements relayed back through the MAX19777 ADC

- MAX32660 10 ball BGA MCU using a Cortex-M4 processor with FPU-based functionality, 256KB Flash, 96KB SRAM, operating speeds up to 96MHz and $85\mu A/MHz$ execution from Flash

- AFE4404 Optical Biosensing Analog Front End

- 680 and 850nm VCSELs for interstial oxygen saturation interrogation

- A GaAs PIN Photodiodes mounted 10 mm away from the VCSELs

- An unpopulated option for running the AFE4404 via a clock signal provided by the MAX32660, which would lower the power consumption of the AFE4404 by bypassing the AFE4404 internal clock.

- Two Carrier mounted LEDs that can be jumped to the AFE4404 LED Actuation pads for testing purposes prior to the wirebonding of the VCSELs (Note: Soldering to these pins will contaminate the pads and thereby make them unwirebondable.

- Carrier mounted Reset and Programming support circuits

- Start-up and programming protection resistors

Each of these components were carefully selected and the layout carefully attune to the fact that the height of these components must still allow the injectable to be inserted within the needle.

Coil Design

The SBC v10 - Mouse Coil was discussed previously in Sec. 6.5.1, since the Mouse coil was used for testing the SBC v03 - Power board, thereby ensuring that the SBC v10 Mouse PCB would be effectively vetted.

6.6.1 Testing Results

DC Power Consumption via V_{rec} input

The board was initially tested for DC power consumption by driving the rectified voltage with a Keithly 2401 Sourcemeter. In Fig.6.32 we see that during running operation (i.e. while processing, communication, or optical signal acquisition is occurring) the system runs at around 11.791 mW. However, due to the larger intermeasurement periods ($> 3s$), the system would predominantly exist in the sleep mode, consuming an average of 9.318 mW, a 21.27% improvement on power consumption due to putting the microprocessor and all dependent components to sleep. As an interesting point of comparison, using the same codebase, the SBC v10 Mouse running power is 14.5% less, and sleep power consumption is 3% less, than the respective power consumption on the SBC v03 Power board.

6.6.2 Challenges Addressed

Encapsulation for Electromagnetic Testing within Saline

While the professional, optically crystal clear encapsulation capable by collaborators at Notre Dame, will serve for the final deliverable. Iterative testing of the electromagnetic properties of the saline immersed system could be completed more rapidly by developing a form-factor, though non-translucent encapsulation method. To do this we relied on the same soluble PVA as done in the form-factor coil design, but in this case the mold was a cylindrical hole in a PVA block. The electroceutical with attached coil would be inserted in the mold, the mold filled from the bottom with the intended epoxy (Norland NOA65) with a syringe, UV light shined through the thin walls of the PVA mold for 10s of minutes, and then the PVA mold dissolved away in water.

6.6.3 Future Work

Fabrication, assembly and initial testing has been completed with the SBC v10 - Mouse. Via the TXC to RXC separation sweep, the system is demonstrated to be able to power the dependent acquisition components and communicate measurements back to a controlling client. The next steps involve mounting the form-factor SBC v10 - Coil to the SBC v10 -

Mouse PCB and encapsulating the entire package within optically clear epoxy. Once the encapsulation is confirmed to be watertight, the same separation sweep will be performed within a saline solution that serves as a electromagnetic phantom for injection within biological tissue. Following on confirming the WPT and communications capability at separations up to 1 cm within saline, the encapsulated SBC v10 - Mouse system will be immersed in oxygenated blood to a depth of 1 cm for the purposes of confirming oxygen saturation tracking. Finally, the encapsulated SBC v10 - Mouse system will be injected within a mouse tumor for local functional monitoring of tumor molecular targets and demonstration of explant capacity.

With the individual pieces tested and confirmed the risk of proceeding steps failing has been significantly reduced. However, significant future work will need to focus on optimized coil development that balances WPT efficiency with communication fidelity. The current systems demonstrates that WPT is capable within air while avoiding SAR limits. However, as the injectable is buried deeper, the TXC to RXC coil S21 will need to improve to offset the reduction in efficiency resulting from the separation increase. Additional testing could include matching a repeater coil via the onboard matching capacitor (presently unpopulated) to the RXC and TXC. This would provide greater flexibility of the RX system to offset and alignment issues that result from implant with live biological models.

6.7 Commercial off the Shelf Injectable Electroceutical Platform - ElectRX

The ElectRX was designed with the intention of providing a generic 12g needle form-factor platform for translational research on biomedical sensors and effectors. This system will allow a researcher to deploy their sensor or effector rapidly in a clinical setting, derisking and paving the way for the development of an application specific circuit. The system, shown in Fig. 6.34, uses many of the same methods, code base, and hardware for transmitting power, uplinking data, and downlinking settings as those explored in the Smart Breast Clip. The primary difference between the two systems, is that in the SBC the communication between the AFE4404 and the MCU are subsumed within the SBC boards, these pins are instead broken out and accessible to the given outboard mounted sensor or effector. A total of

6 pads are exposed to a user: 3.3V Supply, Analog Ground, a 12b ADC Input, a GPIO with alternate I/O timer functionality, as well as I2C Data and Clock with required pull-up resistors. Each of these pads are processed with ENEPIG finish, so that wirebonding would be possible. Additionally, while not easily accessible, there is a 0201 pad broken out near the MCU which provides a solderable additional GPIO access point.

Unlike the SBC though, this system has a 2-turn coil spanning across internal layers 1 and 2 of the PCB, as shown in Fig.6.36a and 6.36b, respectively. This coil has planar dimensions of 9.606 x 1.62 mm, a trace width of 0.089 mm, a trace thickness of 0.0215 mm (1 oz Cu), and a "vertical" turn separation of 0.11 mm, and footprints for a L Impedance Matching Network is provided for tuning purposes. The embedding of this coil, will allow the user of the platform to avoid having to develop around an externally mounted coil, and will enable greater mass production possibilities, as the coil would not need to be wound by hand. Like the SBC, this board also has an optional location for matching a repeater to the internal coil thereby improving the received power efficiency.

Without the repeater matching capacitor, the injectable dimensions after fabrication come to 10 x 2.216 x 0.4mm, so sized for an 11g needle. Like the SBC v10 - Mouse though, the boards traces, pads and vias are offset from the edge of the board so that the board can be filed down to 10 x 1.811. With the inclusion of the repeater capacitor the boards length extends out to 10.914 mm.

Hardware

Much of the primary hardware on the board has been previously implemented and vetted in prior revisions. The most closely related RX is the SBC v10 - Mouse, Sec. 6.6. Referring back to that hardware listing, the primary component change is the removal of the AFE440, VCSELs, and Photodiode. Beyond that and additional layout changes, the primary differential hardware components on this board include the following:

- Tank Capacitance for Rectified DC Energy Storage = 66 μF (expandable to 141.1μF)

- Carrier mounted LED for initial "blinky" testing purposes

Each of these components were carefully selected and the layout carefully attune to the fact that the height of these components must still allow the injectable to be inserted within the needle. The 4-layer 0.4 mm board was found to suffice for making this cut-off, however thinner boards are possible for significantly greater cost. In the small batch run where we had 50 boards fabricated and 20 boards assembled, the total cost per board came to $76.66 per board.

Coil Design

One of the key design aspects of the ElectRX is the embedded 2-turn coil on internal layers 1 and 2. While it has less area than the SBC v10 - Mouse coil, it benefits from not requiring assembly. The self-inductance of the coil came to 1.1417 + 1.8397 Ω or 43.185 nH, as shown in the Smith chart in Fig. 6.37a and achieved an S11 of -6.932 dB at 6.78 MHz after tuning (Fig. 6.37b).

Future Work

The ElectRX v02 has been designed with the knowledge and experience gained through the multiple revisions of the Smart Breast Clip. This system has been fabricated, assembled, and initial testing has demonstrated functionality. The next steps are to demonstrate efficient operation over distance by completing a TXC to Embedded RXC separation, measuring the achievable power output to a dependent sensor/effector while maintain SAR compatibility, and then immersing an encapsulated version of ElectRX in saline to serve as an electromagnetic phantom of the biological tissue where the system would eventually be injected.

While the embedded 2-turn coil in the ElectRX does not provide opportunity for amendment, additional flexibility and efficiency gains might be engendered by attaching a repeater coil to the available, though presently unpopulated, matching capacitor. A repeater coil has the capability of providing efficiency improvements and ruggedizes the RXC to minuscule variations in angle and offset that would be inherent in any in-vivo implant. Lastly, the TXC

will need to be optimized for the ElectRX coil as the impedance and size characteristics differ from those achieved in the Smart Breast Clip.

For future revisions, it might be useful to investigate the inclusion of a rechargeable solid state battery. While the injectable is capable of continuous operation within the WPT field, by including a bare die battery, like the EnerChip CBC910 (1.75 x 2.66 x 0.2mm, $5\mu Ah$), the system could charge, do actions while away from the charging area, store the results, and then report back once reentering the field.

6.8 Conclusion

In the preceding pages a Commercial Off-the-shelf injectable electroceutical was followed from design through to initial testing. The resulting system balances low-power circuit design with the intricacies of wireless power transfer and communications, all while maintaining the form-factor requirement of fitting within a 12g needle after encapsulation. The initial application specific design of a Smart Breast Clip for Continuous Wave Near-infrared Spectroscopy guided the decisions made in the project and resulted in multiple revisions for the ultimate goal of being implanted within a human subject for cancer tracking purposes. From this specific application to a more general platform, the ElectRX injectable was developed to enable researchers to translate sensor and effector research from bench-top to in-vivo applications, providing a standardized battery-free, wireless power with uplink and downlink communication foundation from which to test and confirm operation in biological environments.

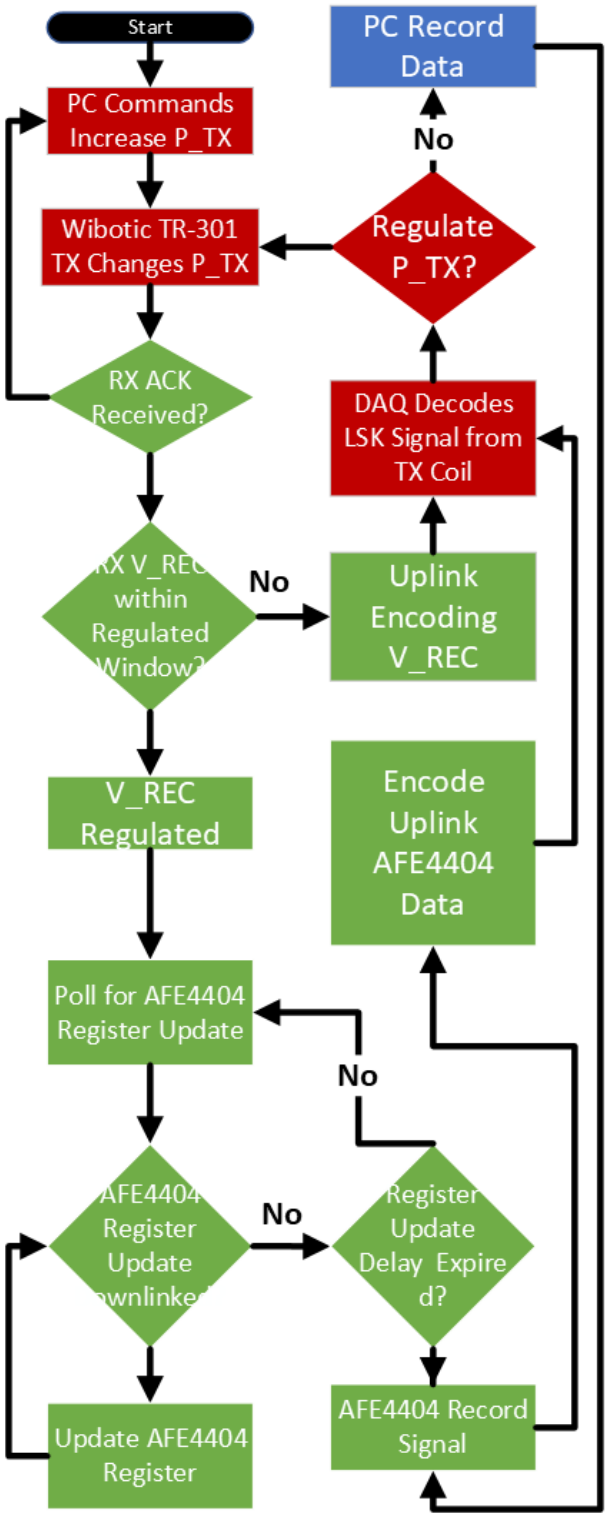

Figure 6.22: The system procedure for closed-loop automated operation.

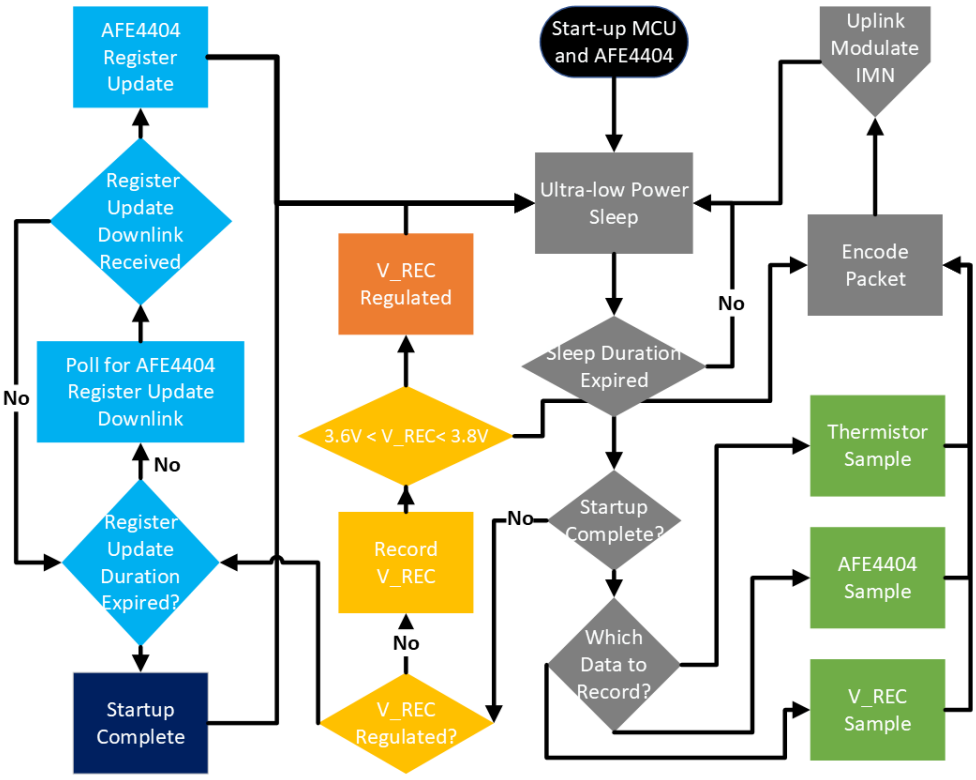

Figure 6.23: The RX automated state machine.

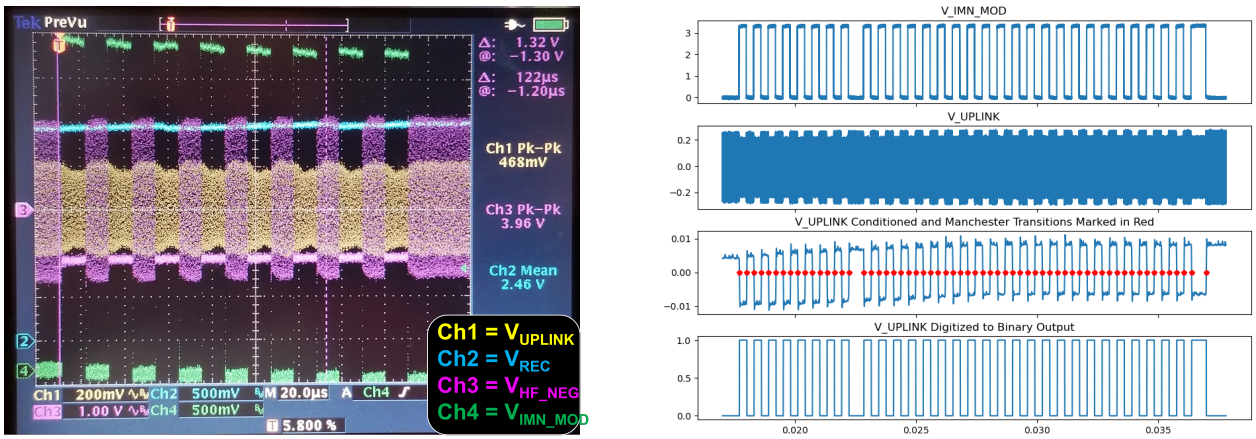

(a) (b)

Figure 6.24: (a)Demonstration of uplink data transmission from the v03 form-factor system. (b) Decoding of the received uplink data transmission

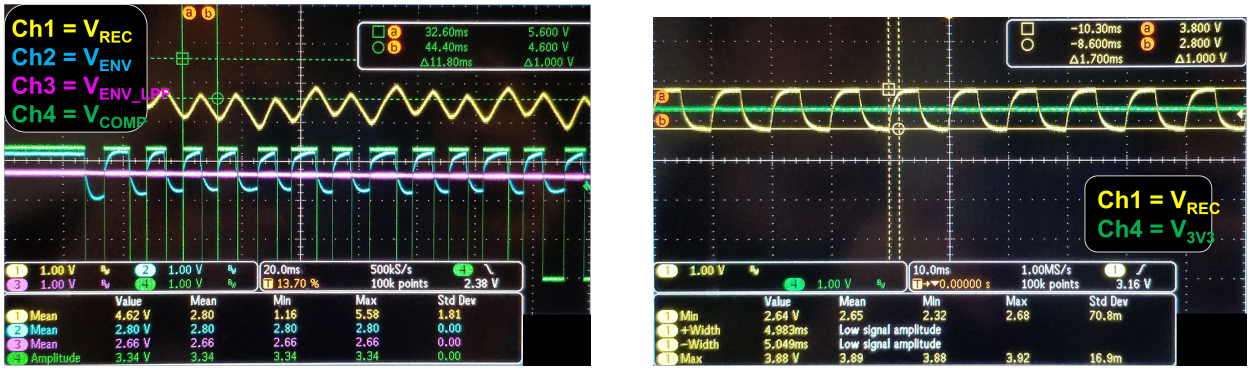

(a) (b)

Figure 6.25: (a)Demonstration of downlink communication using the envelope detector. (b) Demonstration of downlink communication using direct sampling of VREC

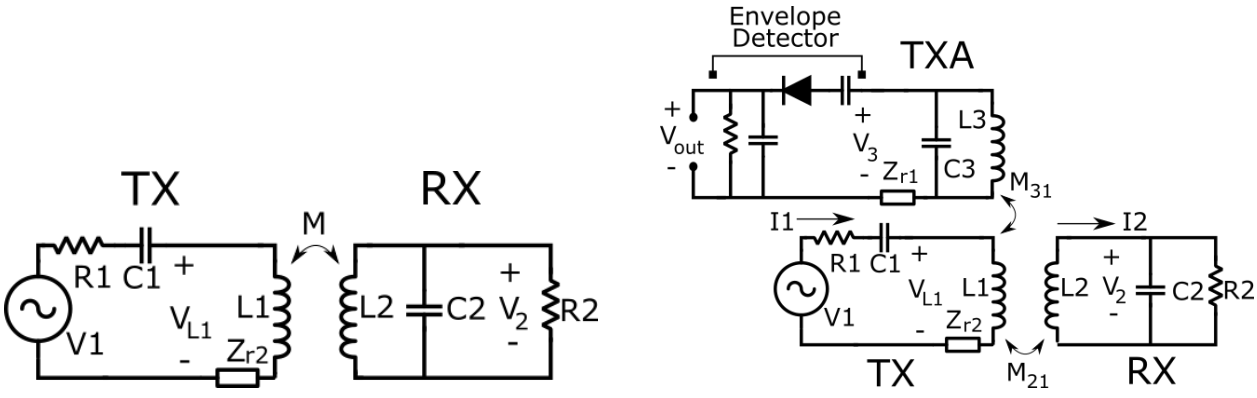

(a) (b)

Figure 6.26: (a) The simplified circuit for analysing Load Shift Keying (b) An alternate detection method using a secondary antenna coil for detecting LSK changes in the primary coil

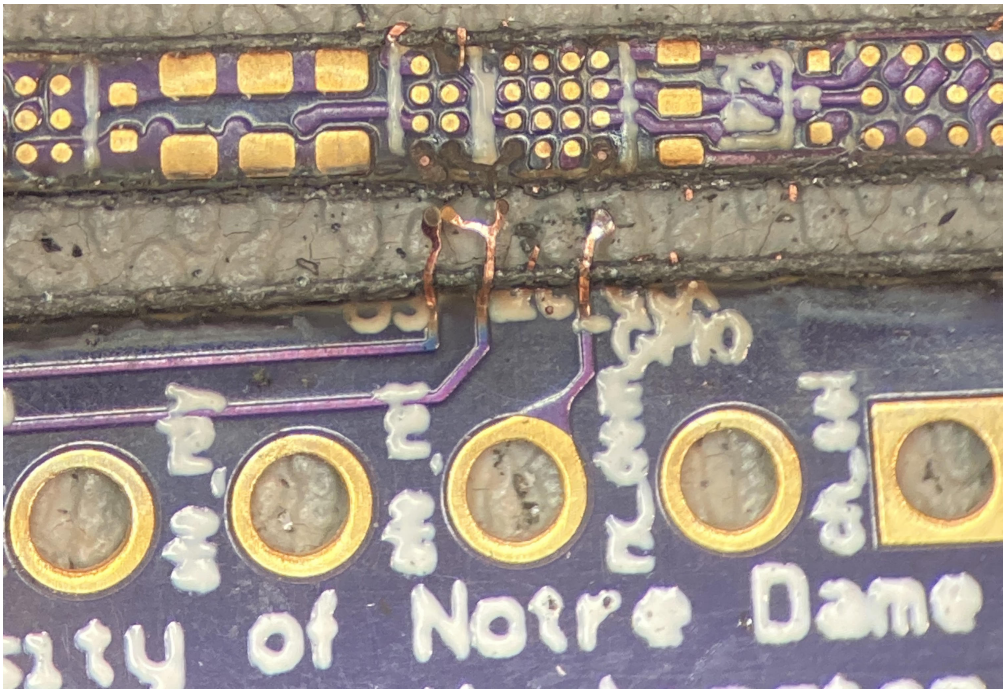

Figure 6.27: An image showing the result of an attempt to laser cut the injectable PCB portion away from the carrier on the SBC v03 - Power board

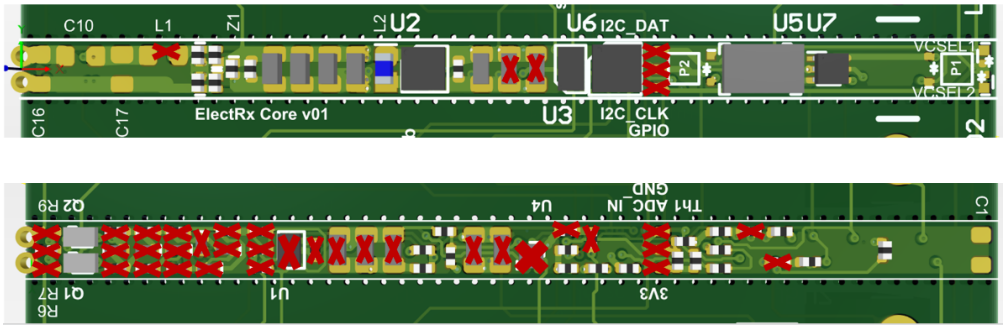

Figure 6.28: An image showing the result of paring away unnecessary components from the SBC v03 - Power board in preparation for the design of the SBC v10 - Mouse

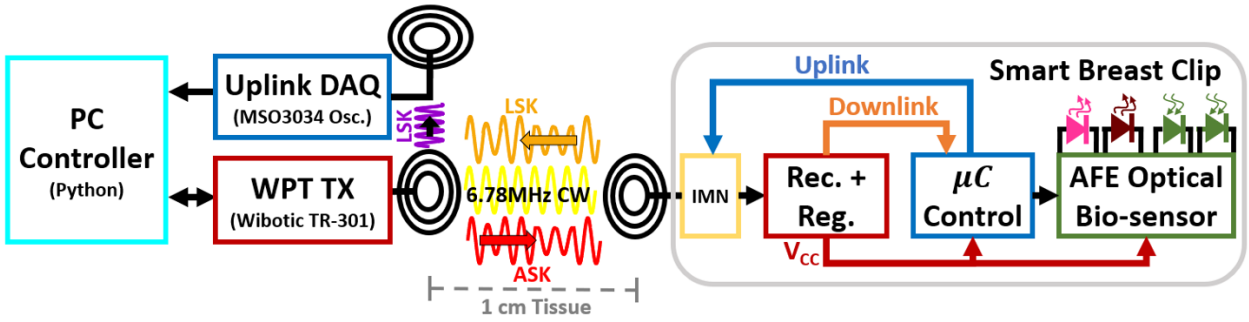

Figure 6.29: A block diagram showing the full system design used for the Smart Breast Clip v10 - Mouse board.

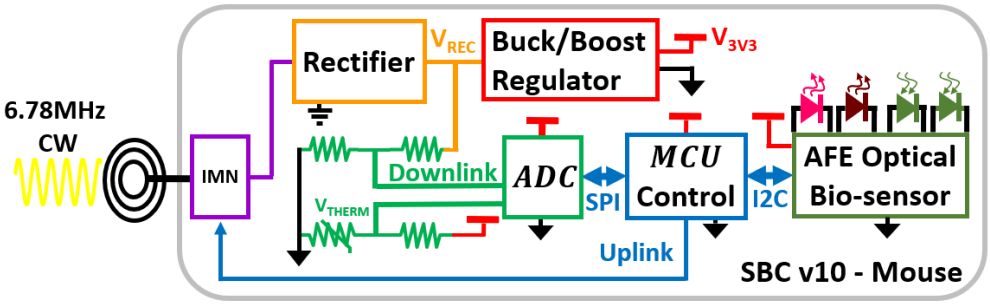

Figure 6.30: A block diagram demonstrating the form-factor RX system, v10 - SBC Mouse Board, that will be tested in a murine model.

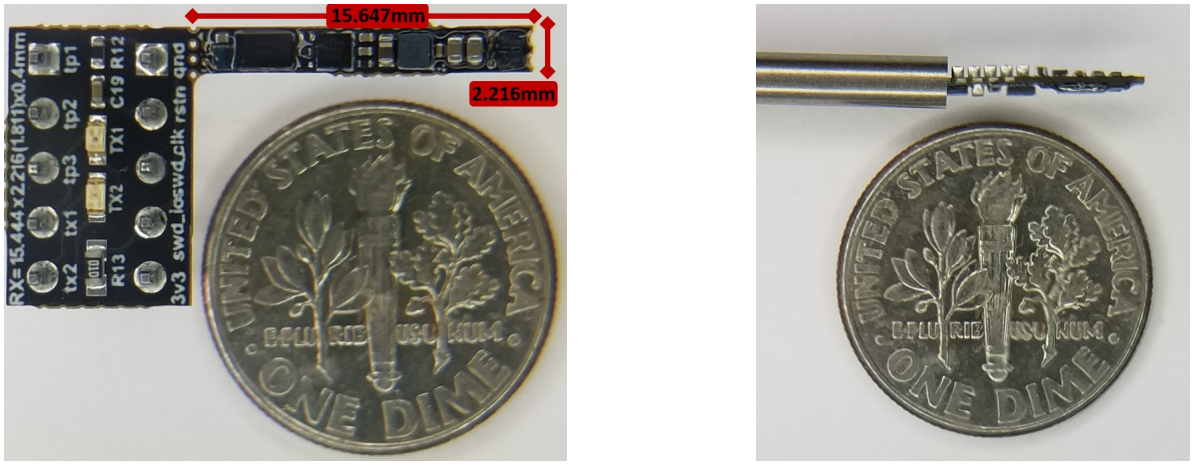

(a) (b)

Figure 6.31: (a) The SBC v10 - Mouse Top (b) The SBC v10 - Mouse within an 11g Needle

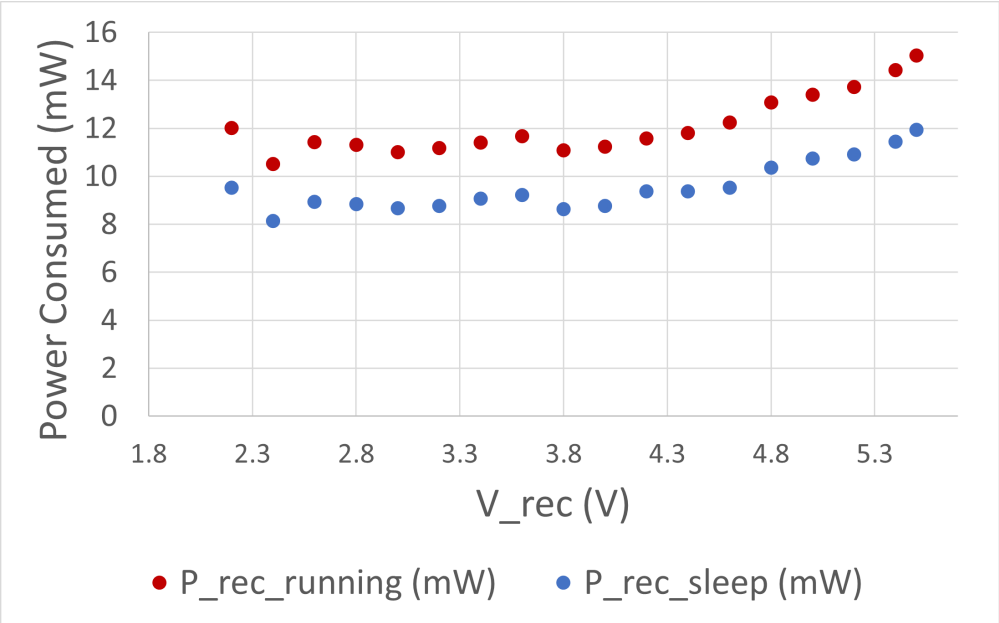

Figure 6.32: The power consumed by the SBC v10 - Mouse board during full operation and then during sleep, demonstrating a 21.27% reduction in power consumption while sleeping.

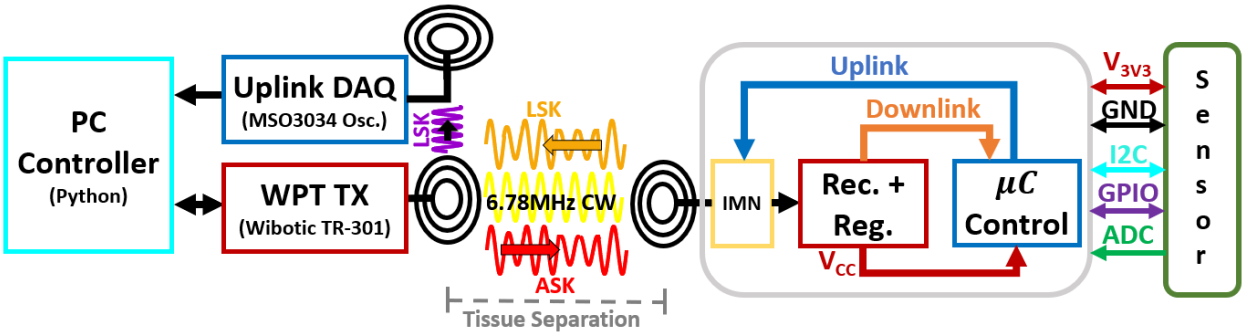

Figure 6.33: System Design for accommodating translational research on biological sensor and effector designs.

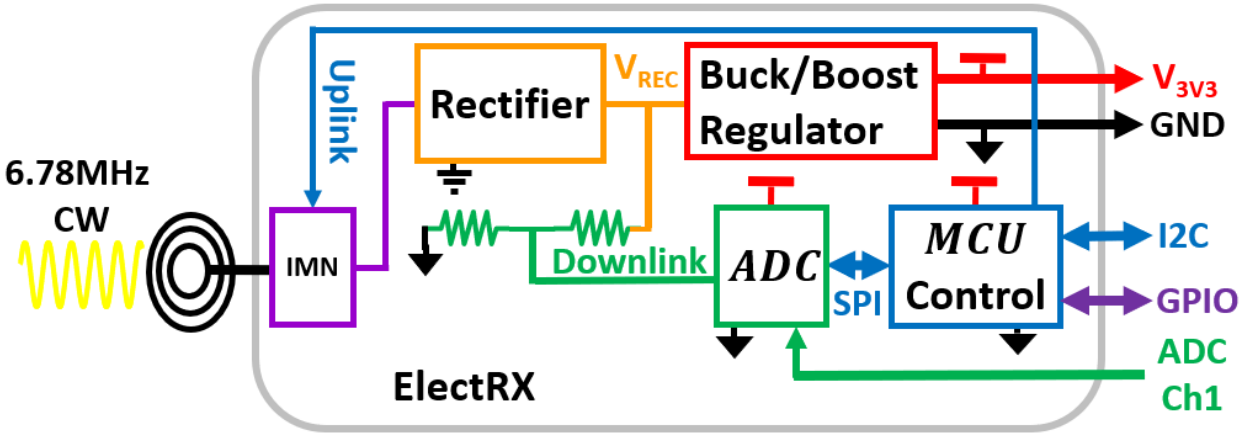

Figure 6.34: The ElectRX v02 board in detail.

(a) (b)

Figure 6.35: (a) ElectRX v02 Top (b) ElectRX within an 11g Needle

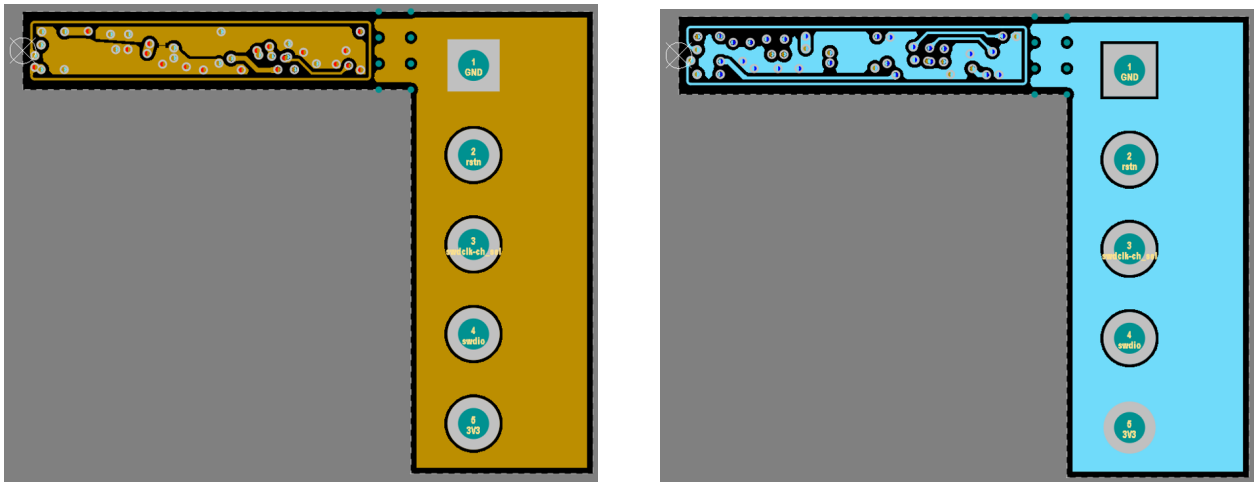

(a) (b)

Figure 6.36: The 2-turn RX Coil is embedded within the Internal Layers 1 (a) and 2 (b) with planar dimensions of 9.606 x 1.62 mm.

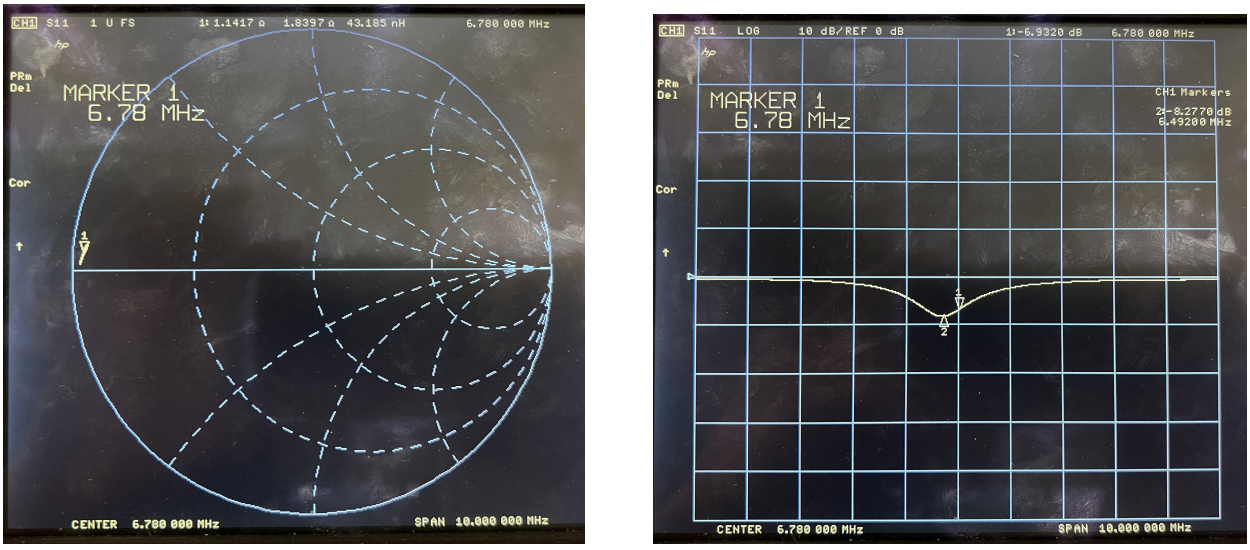

(a) (b)

Figure 6.37: The 2-turn RX Coil is was found to have an (a) inductance of 44 nH and, (b) after tuning, achieved an S11 of -6.932 dB at 6.78 MHz.

Chapter 7

CONCLUSION

In this dissertation a series of enabling technologies surrounding bio-compatible electroceuticals were presented.

The initial work on Packet Assay (PASS), demonstrates how simple, component reduced circuitry combined with the processing power of modern MCUs can allow one to extract discriminating information from the envelope of wireless signals using a sparse NN. The component count compression and power savings possible via this technology will allow for new paradigms of sensing and communication to be explored.

The combination of backscatter communication and coupled resonator WPT demonstrated in the Neurodisc and AIMWPT-RX can provide a attractive foundation for the development of neural signal recording and continuous untethered operation for research and clinical applications. This neurotechnology can demonstrates that functional, high datarate, perpetual neural sensing can be accomplished while controlling for safe in-vivo operation. This includes the investigation of how high-power charging and high datarate communication would be affected within a metallic cage environment, a real-world environment used in present research. While overpowered for the application of most electroceuticals, this system demonstrates an upper limit of capability, from which functionality contraction can be balanced with the size and power constraints experienced by electroceuticals.

As WPT systems enter new environments beyond the practices and sterile benchtop test and the functionally limiting wireless charging capable with commercial WPT transmitters, significant effort will be expended in developing TX and RX coils that can efficiently deliver power over a wide range of orientations, separations, and alignments. While infinitely configurable electromagnetic modeling systems exist, they are interminably slow. The Mostly

Printed Field Characterization System provides a open-source platform for the rapid testing of physical coils for electroceuticals in real-world environments, allowing for the rapid iteration towards optimal coils to fit specific applications.

A significant issue in any WPT to electroceuticals will involve maximizing the efficiency of power transfer between two asymmetric coils. One way of accomplishing this is through the inclusion of a intermediate relay. An optimal intermediate relay would be sized and positioned to provide the best match between a given electroceutical RX coil and TX coil. This enabling technology will allow for deeper placement of electroceuticals within biological tissue.

Incorporating much of the knowledge and experience gained through the preceding research projects, a series of completely wireless and battery-free electroceuticals were developed with commercial off-the-shelf components with form-factor constraints to fit within a 12g needle. The Smart Breast Clip was specifically developed for interrogating the oxygen saturation of tumors for the eventual purpose of tracking tumor progression within humans. The ElectRX was developed to provide a generalized injectable electroceutical platform for translation of sensor and effector bench-top designs to clinical applications.

BIBLIOGRAPHY

[1] John Day, D. Geddis, Jaehwan Kim, Sang H. Choi, H. Yoon, and K. D. Song. Review of radio wave for power transmission in medical applications with safety. In *Smart Structures*, 2015.

[2] Airfuel Alliance. Is wireless power transfer safe?, Jun 2021. Available from: https://airfuel.org/is-wireless-power-transfer-safe/.

[3] M. Karimi, A. Schmid, and C. Dehollain. Wireless power and data transmission for implanted devices via inductive links: A systematic review. *IEEE Sensors Journal*, 21:7145–7161, 2021.

[4] Kush Agarwal, Rangarajan Jegadeesan, Yong-Xin Guo, and Nitish V. Thakor. Wireless power transfer strategies for implantable bioelectronics. *IEEE Reviews in Biomedical Engineering*, 10:136–161, 2017.

[5] Vikram Iyer, R. Nandakumar, Anran Wang, S. Fuller, and Shyamnath Gollakota. Living iot: A flying wireless platform on live insects. *The 25th Annual International Conference on Mobile Computing and Networking*, 2019.

[6] Amir Javan-Khoshkholgh and A. Farajidavar. An implantable inductive near-field communication system with 64 channels for acquisition of gastrointestinal bioelectrical activity. *Sensors (Basel, Switzerland)*, 19, 2019.

[7] Leland McInnes, John Healy, and James Melville. Umap: Uniform manifold approximation and projection for dimension reduction, 2018.

[8] Ami D Shah, A. Mehta, Nishi Talati, R. Brem, and L. Margolies. Breast tissue markers: Why? what's out there? how do i choose? *Clinical imaging*, 52:123–136, 2018.

[9] Thomas O'Sullivan and Joshua R. Smith. Breakthrough level 1 proposal: Smart breast clips for optimizing breast cancer treatment 1, Nov 2019.

[10] Vincent J. Kitsmiller, M. Dummer, K. Johnson, G. Cole, and T. O'Sullivan. Frequency domain diffuse optical spectroscopy with a near-infrared tunable vertical cavity surface emitting laser. *Optics express*, 26 16:21033–21043, 2018.

[11] Y. Joung. Development of implantable medical devices: From an engineering perspective. *International Neurourology Journal*, 17:98 – 106, 2013.

[12] F. Okada, Runa Izutsu, K. Goto, and M. Osaki. Inflammation-related carcinogenesis: Lessons from animal models to clinical aspects. *Cancers*, 13, 2021.

[13] A. Greenspon, Jasmine D. Patel, E. Lau, J. Ochoa, D. Frisch, R. Ho, B. Pavri, and S. Kurtz. Trends in permanent pacemaker implantation in the united states from 1993 to 2009: increasing complexity of patients and procedures. *Journal of the American College of Cardiology*, 60 16:1540–5, 2012.

[14] Ashley M Nassiri, Donna L. Sorkin, and Matthew L. Carlson. Current estimates of cochlear implant utilization in the united states. *Otology & Neurotology*, 43:e558 – e562, 2022.

[15] Robert Bowen, T. Graetz, D. Emmert, and M. Avidan. Statistics of heart failure and mechanical circulatory support in 2020. *Annals of translational medicine*, 8 13:827, 2020.

[16] A. Kiourti and K. Nikita. A review of in-body biotelemetry devices: Implantables, ingestibles, and injectables. *IEEE Transactions on Biomedical Engineering*, 64:1422–1430, 2017.

[17] Rikky Muller, Hanh-Phuc Le, Wen Li, Peter Ledochowitsch, Simone Gambini, Toni Bjorninen, Aaron Koralek, Jose M. Carmena, Michel M. Maharbiz, Elad Alon, and Jan M. Rabaey. A minimally invasive 64-channel wireless μecog implant. *IEEE Journal of Solid-State Circuits*, 50(1):344–359, 2015.

[18] D. Seo, R. Neely, Konlin Shen, Utkarsh Singhal, E. Alon, J. Rabaey, J. Carmena, and M. Maharbiz. Wireless recording in the peripheral nervous system with ultrasonic neural dust. *Neuron*, 91:529–539, 2016.

[19] John Uehlin, William Anthony Smith, Venkata Rajesh Pamula, Steve Perlmutter, Visvesh Sathe, and Jacques Christophe Rudell. A bidirectional brain computer interface with 64-channel recording, resonant stimulation and artifact suppression in standard 65nm cmos. In *ESSCIRC 2019 - IEEE 45th European Solid State Circuits Conference (ESSCIRC)*, pages 77–80, 2019.

[20] H. Ando, K. Takizawa, Takeshi Yoshida, K. Matsushita, M. Hirata, and T. Suzuki. Wireless multichannel neural recording with a 128-mbps uwb transmitter for an implantable brain-machine interfaces. *IEEE Transactions on Biomedical Circuits and Systems*, 10:1068–1078, 2016.

[21] M. Yuce and T. Dissanayake. Easy-to-swallow wireless telemetry. *IEEE Microwave Magazine*, 13:90–101, 2012.

[22] J. Thoné, S. Radiom, D. Turgis, R. Carta, G. Gielen, and R. Puers. Design of a 2 mbps fsk near-field transmitter for wireless capsule endoscopy. *Sensors and Actuators A-physical*, 156:43–48, 2009.

[23] P. J. van der Schaar, J. F. Dijksman, Henny Broekhuizen de Gast, J. Shimizu, N. van Lelyveld, H. Zou, V. Iordanov, C. Wanke, and P. Siersema. A novel ingestible electronic drug delivery and monitoring device. *Gastrointestinal endoscopy*, 78 3:520–8, 2013.

[24] A. Alipour, Stephen Gabrielson, and P. B. Patel. Ingestible sensors and medication adherence: Focus on use in serious mental illness. *Pharmacy: Journal of Pharmacy Education and Practice*, 8, 2020.

[25] Yei Hwan Jung, Jong Uk Kim, Ju Seung Lee, Joo Hwan Shin, Woojin Jung, Jehyung Ok, and Tae il Kim. Injectable biomedical devices for sensing and stimulating internal body organs. *Advanced materials*, page e1907478, 2020.

[26] Dangerous Things. xnt nfc chip: Rfid; nfc chip implants and biohacking products, Jul 2021. Available from: https://dangerousthings.com/product/xnt/.

[27] Senseonics. Fda approves world's first long-term implantable continuous glucose monitoring system for marketing in united states. Available from: https://www.senseonics.com/investor-relations/news-releases/2018/06-21-2018-201353063.

[28] Ascensia Diabetes. Eversense sensor. Available from: https://www.ascensiadiabetes.com/eversense/eversense-cgm-system/sensor/.

[29] Shane M Regnier, Jeffrey L Chen, R. Gabriel, and Krishnan V Chakravarthy. A review of the stimrouter® peripheral neuromodulation system for chronic pain management. *Pain management*, 2020.

[30] T. Whitehurst, J. Schulman, K. Jaax, and R. Carbunaru. The bion® microstimulator and its clinical applications. In *Implantable Neural Prostheses 1*, 2009.

[31] A. Hennig and G. V. Bögel. Analysis of power absorption by human tissue in deeply implantable medical sensor transponders. *Advanced Microwave Circuits and Systems*, 2010.

[32] G. Lazzi. Thermal effects of bioimplants. *IEEE Engineering in Medicine and Biology Magazine*, 24:75–81, 2005.

[33] M. Grandolfo. Worldwide standards on exposure to electromagnetic fields: an overview. *The Environmentalist*, 29:109–117, 2009.

[34] INC. PCTEST ENGINEERING LABORATORY. Sar evaluation report, Jan 2017. Available From: https://fccid.io/EMJCPM30W17/RF-Exposure-Info/RF-Exposure-Information-SAR-PDF-3323147.pdf.

[35] AirFuel Alliance. Frequency choice, Jun 2021. Available from: https://airfuel.org/frequency-choice/.

[36] A. Sharma, S. Yadav, Sandeep N. Dandu, Joydeep Sengupta, S. Dhok, and Sudhir Kumar. Magnetic induction-based non-conventional media communications: A review. *IEEE Sensors Journal*, 17:926–940, 2017.

[37] Han-Joon Kim, H. Hirayama, Sanghoek Kim, K. J. Han, Rui Zhang, and Ji-Woong Choi. Review of near-field wireless power and communication for biomedical applications. *IEEE Access*, 5:21264–21285, 2017.

[38] Chen Gong, Dake Liu, Zhidong Miao, W. Wang, and M. Li. An nfc on two-coil wpt link for implantable biomedical sensors under ultra-weak coupling. *Sensors (Basel, Switzerland)*, 17, 2017.

[39] J. Agbinya, Nithya Selvaraj, A.-L. Ollett, Stephane Ibos, Yasmin Ooi-Sanchez, Mark Brennan, and Z. Chaczko. Size and characteristics of the 'cone of silence' in near field magnetic induction communications. *Proc. MiLCIS*, 2009.

[40] C. Jiang, H. Zhang, Y. Ren, Z. Han, K. Chen, and L. Hanzo. Machine learning paradigms for next-generation wireless networks. *IEEE Wireless Communications*, 24(2):98–105, 2017.

[41] H. Feng, Y. Shu, S. Wang, and M. Ma. Svm-based models for predicting wlan traffic. In *2006 IEEE International Conference on Communications*, volume 2, pages 597–602, 2006.

[42] Y. Lecun, L. Bottou, Y. Bengio, and P. Haffner. Gradient-based learning applied to document recognition. *Proceedings of the IEEE*, 86(11):2278–2324, 1998.

[43] Alex Krizhevsky. Learning multiple layers of features from tiny images. Technical report, University of Toronto, 2009.

[44] CRAWDAD. A community resource for archiving wireless data at dartmouth. https://crawdad.org/index.html.

[45] Ljubica Pajevic, Gunnar Karlsson, and Viktoria Fodor. CRAWDAD dataset kth campus (v. 2019-07-01). Downloaded from https://crawdad.org/kth/campus/20190701, July 2019.

[46] Michael Haus, Aaron Yi Ding, and Jorg Ott. CRAWDAD dataset tum/proximityness (v. 2020-02-18). Downloaded from https://crawdad.org/tum/proximityness/20200218, February 2020.

[47] Sergej Grunau, Dimitri Block, and Uwe Meier. Multi-label wireless interference identification with convolutional neural networks. *CoRR*, abs/1804.04395, 2018.

[48] S. Riyaz, K. Sankhe, S. Ioannidis, and K. Chowdhury. Deep learning convolutional neural networks for radio identification. *IEEE Communications Magazine*, 56(9):146–152, Sep. 2018.

[49] Timothy J. O'Shea and Johnathan Corgan. Convolutional radio modulation recognition networks. *CoRR*, abs/1602.04105, 2016.

[50] Mohammad Lotfollahi, Ramin Shirali Hossein Zade, Mahdi Jafari Siavoshani, and Mohammdsadegh Saberian. Deep packet: A novel approach for encrypted traffic classification using deep learning. *CoRR*, abs/1709.02656, 2017.

[51] MATLAB. Wlan toolbox. https://www.mathworks.com/products/wlan.html.

[52] Igor Fedorov, Ryan P. Adams, Matthew Mattina, and Paul N. Whatmough. Sparse: Sparse architecture search for cnns on resource-constrained microcontrollers. *CoRR*, abs/1905.12107, 2019.

[53] Martín Abadi, Ashish Agarwal, Paul Barham, Eugene Brevdo, Zhifeng Chen, Craig Citro, Greg S. Corrado, and et al. TensorFlow: Large-scale machine learning on heterogeneous systems. Software available from tensorflow.org, 2015. Available from: http://tensorflow.org/.

[54] J. Bergstra, D. Yamins, and D. D. Cox. Making a science of model search: Hyperparameter optimization in hundreds of dimensions for vision architectures. In *Proceedings of the 30th International Conference on International Conference on Machine Learning - Volume 28*, ICML'13, pages I–115–I–123. JMLR.org, 2013.

[55] Diederik P. Kingma and Jimmy Ba. Adam: A method for stochastic optimization. cite arxiv:1412.6980Comment: Published as a conference paper at the 3rd International Conference for Learning Representations, San Diego, 2015, 2014.

[56] Suhua Tang and Sadao Obana. Reducing false wake-up in contention-based wake-up control of wireless lans. *Wireless Networks*, 25(5):2333–2349, Jul 2019.

[57] Ashish Kumar, Saurabh Goyal, and Manik Varma. Resource-efficient machine learning in 2 KB RAM for the internet of things. In Doina Precup and Yee Whye Teh, editors, *Proceedings of the 34th International Conference on Machine Learning*, volume 70 of *Proceedings of Machine Learning Research*, pages 1935–1944, International Convention Centre, Sydney, Australia, 06–11 Aug 2017. PMLR.

[58] Chirag Gupta, Arun Sai Suggala, Ankit Goyal, Harsha Vardhan Simhadri, Bhargavi Paranjape, Ashish Kumar, Saurabh Goyal, Raghavendra Udupa, Manik Varma, and Prateek Jain. ProtoNN: Compressed and accurate kNN for resource-scarce devices. In Doina Precup and Yee Whye Teh, editors, *Proceedings of the 34th International Conference on Machine Learning*, volume 70 of *Proceedings of Machine Learning Research*, pages 1331–1340, International Convention Centre, Sydney, Australia, 06–11 Aug 2017. PMLR.

[59] American Institute for Medical and Biological Engineering. Medical and biological engineering in the next 20 years: The promise and the challenges. *IEEE Transactions on Biomedical Engineering*, 60(7):1767–1775, 2013.

[60] J. C. Kao, S. D. Stavisky, D. Sussillo, P. Nuyujukian, and K. V. Shenoy. Information systems opportunities in brain–machine interface decoders. *Proceedings of the IEEE*, 102(5):666–682, 2014.

[61] G. Anumanchipalli, J. Chartier, and E. Chang. Speech synthesis from neural decoding of spoken sentences. *Nature*, 568:493–498, 04 2019.

[62] F. B. Wagner et al. Targeted neurotechnology restores walking in humans with spinal cord injury. *Nature*, 563(7729):65–71, 2018.

[63] F. Inanici, S. Samejima, P. Gad, V. R. Edgerton, C. P. Hofstetter, and C. T. Moritz. Transcutaneous electrical spinal stimulation promotes long-term recovery of upper extremity function in chronic tetraplegia. *IEEE Transactions on Neural Systems and Rehabilitation Engineering*, 26(6):1272–1278, 2018.

[64] J.L. Abelson, G.C. Curtis, O Sagher, R.C. Albucher, M. Harrigan, S.F. Taylor, B. Martis, and B. Giordani. Deep brain stimulation for refractory obsessive-compulsive disorder. *Biological Psychiatry*, 57(5):510–6, 2005.

[65] European Research Council. EU brain research. *EU support for research and innovation in the area of the brain*, Jul 2020. Available from: https://ec.europa.eu/info/research-and-innovation/research-area/health-research-and-innovation/brain-research.

[66] Defense Advanced Research Projects Agency (DARPA). DARPA awards contracts for work on spinal cord injury treatment. *DARPA News*, Nov 2020. Available from: https://www.darpa.mil/news-events/2020-11-09.

[67] T. Bjorninen, R. Muller, P. Ledochowitsch, L. Sydanheimo, L. Ukkonen, M. M. Maharbiz, and J. M. Rabaey. Design of wireless links to implanted brain–machine interface microelectronic systems. *IEEE Antennas and Wireless Propagation Letters*, 11:1663–1666, 2012.

[68] A. Sharma, E. Kampianakis, and M. S. Reynolds. A dual-band HF and UHF antenna system for implanted neural recording and stimulation devices. *IEEE Antennas and Wireless Propagation Letters*, 16:493–496, 2017.

[69] C. Pandarinath et al. High performance communication by people with paralysis using an intracortical brain-computer interface. *eLife*, 6:e18554, Feb 2017.

[70] A. Jackson, J. Mavoori, and E. E. Fetz. Correlations between the same motor cortex cells and arm muscles during a trained task, free behavior, and natural sleep in the macaque monkey. *Physiology*, 97(1):360–374, Jan. 2007.

[71] A. Burton, S. N. Obaid, A. Vázquez-Guardado, M. B. Schmit, T. Stuart, L. Cai, Z. Chen, I. Kandela, C. R. Haney, E. A. Waters, H. Cai, J. A. Rogers, L. Lu, and P. Gutruf. Wireless, battery-free subdermally implantable photometry systems for chronic recording of neural dynamics. *Proceedings of the National Academy of Sciences of the United States of America*, 117(6):2835–2845, 2020.

[72] T. Ibrahim, D. Abraham, and R. Rennaker. Electromagnetic power absorption and temperature changes due to brain machine interface operation. *Annals of Biomedical Engineering*, 35:825–834, 2007.

[73] P. D. Wolf. *Indwelling Neural Implants: Strategies for Contending with the In Vivo Environment*. CRC Press/Taylor & Francis, Boca Raton, FL, 2008.

[74] Wireless Power Consortium. The qi wireless power transfer system power class 0 specification parts 1 and 2: Interface definitions, ver. 1.2.4, 2018.

[75] J. Rosenthal, A. Sharma, E. Kampianakis, and M. S. Reynolds. A 25 Mbps, 12.4 pJ/b DQPSK backscatter data uplink for the NeuroDisc brain-computer interface. *IEEE Transactions on Biomedical Circuits and Systems*, 13(5):858–867, Oct. 2019.

[76] S. J. Thomas, R. R. Harrison, A. Leonardo, and M. S. Reynolds. A battery-free multichannel digital neural/EMG telemetry system for flying insects. *IEEE Transactions on Biomedical Circuits and Systems*, 6(5):424–436, Oct 2012.

[77] S. Naderiparizi, A. N. Parks, Z. Kapetanovic, B. Ransford, and J. R. Smith. Wispcam: A battery-free RFID camera. In *Proceedings of the 2015 IEEE International Conference on RFID*, pages 166–173, 2015.

[78] Hao Jiang, Junmin Zhang, Di Lan, K. K. Chao, S. Liou, H. Shahnasser, R. Fechter, S. Hirose, M. Harrison, and Shuvo Roy. A low-frequency versatile wireless power transfer technology for biomedical implants. *IEEE Transactions on Biomedical Circuits and Systems*, 7:526–535, 2013.

[79] E. V. Evarts. Temporal patterns of discharge of pyramidal tract neurons during sleep and waking in the monkey. *Physiology*, 27(2):152–171, Mar. 1964.

[80] G. Corder, B. Ahanonu, B. F. Grewe, D. Wang, M. J. Schnitzer, and G. Scherrer. An amygdalar neural ensemble that encodes the unpleasantness of pain. *Science*, 363(6424):276–281, 2019.

[81] W. Taube, M. Mouthon, C. Leukel, H. Hoogewoud, J. Annoni, and M. Keller. Brain activity during observation and motor imagery of different balance tasks: An fMRI study. *Cortex*, 64:102–114, 2015.

[82] T. Deffieux, C. Demene, M. Pernot, and M. Tanter. Functional ultrasound neuroimaging: a review of the preclinical and clinical state of the art. *Current Opinion in Neurobiology*, 50:128–135, 2018. Neurotechnologies.

[83] A. P. Georgopoulos, J. F. Kalaska, R. Caminiti, and J. T. Massey. On the relations between the direction of two-dimensional arm movements and cell discharge in primate motor cortex. *Journal of Neuroscience*, 2(11):1527–1537, 1982.

[84] P. D. Cheney and E. E. Fetz. Functional classes of primate corticomotorneuronal cells and their relation to active force. *Journal of Neurophysiology*, 44(4):773–791, 1980.

[85] T. N. Aflalo and M. S. A. Graziano. Partial tuning of motor cortex neurons to final posture in a free-moving paradigm. *Proceedings of the National Academy of Sciences of the United States of America*, 103(8):2909–2914, Feb. 2006.

[86] L. R. Hochberg et al. Reach and grasp by people with tetraplegia using a neurally controlled robotic arm. *Nature*, 485:372–375, May 2012.

[87] J. L. Collinger et al. High-performance neuroprosthetic control by an individual with tetraplegia. *The Lancet*, 381(9866):557–564, 2013.

[88] N. C. Swann et al. Adaptive deep brain stimulation for Parkinson's disease using motor cortex sensing. *Journal of Neural Engineering*, 15(4), 2018.

[89] Defense Advanced Research Projects Agency. DARPA and the Brain Initiative, 2019. https://www.darpa.mil/program/our-research/darpa-and-the-brain-initiative.

[90] C. A. Chestek, V. Gilja, P. Nuyujukian, R. J. Kier, F. Solzbacher, S. I. Ryu, R. R. Harrison, and K. V. Shenoy. Hermesc: Low-power wireless neural recording system for freely moving primates. *IEEE Transactions on Neural Systems and Rehabilitation Engineering*, 17(4):330–338, 2009.

[91] S. Zanos, A. G. Richardson, L. Shupe, F. P. Miles, and E. E. Fetz. The Neurochip-2: An autonomous head-fixed computer for recording and stimulating in freely behaving monkeys. *IEEE Transactions on Neural Systems and Rehabilitation Engineering*, 19(4):427–435, 2011.

[92] M. Yin et al. Wireless neurosensor for full-spectrum electrophysiology recordings during free behavior. *Neuron*, 84(6):1170–1182, Dec 2014.

[93] R. Muller et al. A minimally invasive 64-channel wireless μECoG implant. *IEEE Journal of Solid-State Circuits*, 50(1):344–359, 2015.

[94] X. Liu, M. Zhang, A. G. Richardson, T. H. Lucas, and J. Van der Spiegel. Design of a closed-loop, bidirectional brain machine interface system with energy efficient neural feature extraction and PID control. *IEEE Transactions on Biomedical Circuits and Systems*, 11(4):729–742, Aug 2017.

[95] San Disk Corporation. San disk microSD: OEM Product Manual, Section 2.1.1 Typical Card Power Requirements, 2010. https://www.alliedelec.com/m/d/04db416b291011446889dbd6129e2644.pdf.

[96] J. A. Fernandez-Leon et al. A wireless transmission neural interface system for unconstrained non-human primates. *Journal of Neural Engineering*, 12(5):056005, Oct 2015.

[97] R. Matthes. ICNIRP Guidelines for limiting exposure to time-varying electric, magnetic and electromagnetic fields (up to 300 GHz). *Health Physics*, 4:494–522, 1998.

[98] P.J. Dimbylow and S.M. Mann. SAR calculations in an anatomically realistic model of the head for mobile communication transceivers at 900 MHz and 1.8 GHz. *Physics in Medicine and Biology*, 39(10):1537, 1994.

[99] Uei-Ming Jow, Peter McMenamin, Mehdi Kiani, Joseph R. Manns, and Maysam Ghovanloo. Enercage: A smart experimental arena with scalable architecture for behavioral experiments. *IEEE Transactions on Biomedical Engineering*, 61(1):139–148, 2014.

[100] Byunghun Lee, Mehdi Kiani, and Maysam Ghovanloo. A smart wirelessly powered homecage for long-term high-throughput behavioral experiments. *IEEE Sensors Journal*, 15(9):4905–4916, 2015.

[101] S. Abdollah Mirbozorgi, Yaoyao Jia, Daniel Canales, and Maysam Ghovanloo. A wirelessly-powered homecage with segmented copper foils and closed-loop power control. *IEEE Transactions on Biomedical Circuits and Systems*, 10(5):979–989, 2016.

[102] S. Abdollah Mirbozorgi, Hadi Bahrami, Mohamad Sawan, and Benoit Gosselin. A smart cage with uniform wireless power distribution in 3d for enabling long-term experiments with freely moving animals. *IEEE Transactions on Biomedical Circuits and Systems*, 10(2):424–434, 2016.

[103] E. Maghsoudloo, G. Gagnon-Turcotte, Z. Rezaei, and B. Gosselin. A smart neuroscience platform with wireless power transmission for simultaneous optogenetics and electrophysiological recording. In *2018 IEEE International Symposium on Circuits and Systems (ISCAS)*, pages 1–5, 2018.

[104] Henry Mei, Kyle A. Thackston, Rebecca A. Bercich, John G.R. Jefferys, and Pedro P. Irazoqui. Cavity resonator wireless power transfer system for freely moving animal experiments. *IEEE Transactions on Biomedical Engineering*, 64(4):775–785, 2017.

[105] S. Sriram, Shitij Avlani, M. Ward, and S. Sen. Electro-quasistatic animal body communication for untethered rodent biopotential recording. *Scientific Reports*, 11, 2021.

[106] A. Sharma, E. Kampianakis, J. Rosenthal, A. Pike, A. Dadkhah, and M. S. Reynolds. Wideband UHF DQPSK backscatter communication in reverberant cavity animal cage environments. *IEEE Transaction on Antennas and Propagation*, 67(8):5002–5011, Feb. 2019.

[107] Marco Piangerelli, Marco Ciavarro, A. Paris, S. Marchetti, P. Cristiani, Cosimo Puttilli, N. Torres, A. Benabid, and P. Romanelli. A fully integrated wireless system for intracranial direct cortical stimulation, real-time electrocorticography data transmission, and smart cage for wireless battery recharge. *Frontiers in Neurology*, 5, 2014.

[108] M. Powell, William R. Britz, James Harper, and D. Borton. An engineered home environment for untethered data telemetry from nonhuman primates. *Journal of Neuroscience Methods*, 288:72–81, 2017.

[109] S. J. Thomas and M. S. Reynolds. A 96 Mbit/sec, 15.5 pJ/bit 16-QAM modulator for UHF backscatter communication. In *Proceedings of the 2012 IEEE International Conference on RFID*, pages 185–190, Apr. 2012.

[110] J. F. Ensworth and M. S. Reynolds. Every smart phone is a backscatter reader: Modulated backscatter compatibility with Bluetooth 4.0 Low Energy (BLE) devices. In *Proceedings of the 2015 IEEE International Conference on RFID*, 2015.

[111] A. Ebrazeh and P. Mohseni. 30 pJ/b, 67 Mbps, centimeter-to-meter range data telemetry with an IR-UWB wireless link. *IEEE Transactions on Biomedical Circuits and Systems*, 9(3):362–369, June 2015.

[112] D. Kim, M. A. Ingram, and W. W. Smith. Measurements of small-scale fading and path loss for long range RF tags. *IEEE Transactions on Antennas and Propagation*, 51(8):1740–1749, 2003.

[113] J. D. Griffin and G. D. Durgin. Complete link budgets for backscatter-radio and RFID systems. *IEEE Antennas and Propagation Magazine*, 51(2):11–25, April 2009.

[114] J. Rosenthal and M. S. Reynolds. A 158 pJ/bit 1.0 Mbps Bluetooth Low Energy (BLE) compatible backscatter communication system for wireless sensing. In *Proceedings of the 2019 IEEE Topical Conference on Wireless Sensors and Sensor Networks (WiSNet)*, pages 1–3, Jan 2019.

[115] J. Rosenthal and M. S. Reynolds. A 1.0-Mb/s 198-pJ/bit Bluetooth Low-Energy compatible single sideband backscatter uplink for the NeuroDisc brain–computer interface. *IEEE Transactions on Microwave Theory and Techniques*, 67(10):4015–4022, Oct. 2019.

[116] J. Rosenthal and M. S. Reynolds. Hardware-efficient all-digital architectures for OFDM backscatter modulators. *IEEE Transactions on Microwave Theory and Techniques*, 69(1):803–811, Dec. 2020.

[117] Intan Technologies, LLC. RHS2000 series digital stimulator and amplifier chips, 2019. http://intantech.com/.

[118] D.A. Schwarz et al. Chronic, wireless recordings of large-scale brain activity in freely moving rhesus monkeys. *Nature Methods*, 11(6):670, 2014.

[119] H. Ando, K. Takizawa, T. Yoshida, K. Matsushita, M. Hirata, and T. Suzuki. Wireless multichannel neural recording with a 128-Mbps UWB transmitter for an implantable brain-machine interfaces. *IEEE Transactions on Biomedical Circuits and Systems*, 10(6):1068–1078, Dec 2016.

[120] K. Teng, T. Wu, X. Liu, Z. Yang, and C. Heng. A 400 MHz wireless neural signal processing IC with 625 × on-chip data reduction and reconfigurable BFSK/QPSK transmitter based on sequential injection locking. *IEEE Transaction on Biomedical Circuits and Systems*, 11(3):547–557, June 2017.

[121] J. Xu et al. A low-noise, wireless, frequency-shaping neural recorder. *IEEE Transactions on Emerging and Selected Topics in Circuits and Systems*, 8(2):187–200, June 2018.

[122] Alanson P. Sample, David T. Meyer, and Joshua R. Smith. Analysis, experimental results, and range adaptation of magnetically coupled resonators for wireless power transfer. *IEEE Transactions on Industrial Electronics*, 58(2):544–554, 2011.

[123] M. Kesler. Highly resonant wireless power transfer: Safe, efficient, and over distance. 2013.

[124] David L. Means and Kwok W. Chan. Evaluating compliance with fcc guidelines for human exposure to radiofrequency electromagnetic fields. *Federal Communications Commission Office of Engineering and Technology*, OET Bulletin 65(Supplement C), 2001.

[125] Nam-Yun Kim, Kyung seob Kim, J. Choi, and C. Kim. Adaptive frequency with power-level tracking system for efficient magnetic resonance wireless power transfer. *Electronics Letters*, 48:452–454, 2012.

[126] B. Waters, A. Sample, and Joshua R. Smith. Adaptive impedance matching for magnetically coupled resonators. 2012.

[127] Yongseok Lim, Hoyoung Tang, Seung ok Lim, and J. Park. An adaptive impedance-matching network based on a novel capacitor matrix for wireless power transfer. *IEEE Transactions on Power Electronics*, 29:4403–4413, 2014.

[128] Patrick D. Wolf and William M. Reichert. Thermal considerations for the design of an implanted cortical brain–machine interface (bmi). *Indwelling Neural Implants*, page 81–104, 2007.

[129] Hardware, May 2021. Available from: https://www.wibotic.com/products/hardware/.

[130] A. Sharma. *Dual-band power and communication antennas for wireless brain-computer interfaces*. PhD thesis, University of Washington, 2019.

[131] Modular primate cage units: Lab animal housing & equipment. Available from: https://labproductsinc.com/product/modular-primate-cage-units/.

[132] The mostly printed cnc, 2019. Available from: https://docs.v1engineering.com/mpcnc/intro/.

[133] Haopeng Han, Raphael Moritz, Eva Oberacker, Helmar Waiczies, Thoralf Niendorf, and Lukas Winter. Open source 3d multipurpose measurement system with submillimetre fidelity and first application in magnetic resonance. *Scientific Reports*, 7(1):13452, 2017.

[134] Reem Shadid and Sima Noghanian. A literature survey on wireless power transfer for biomedical devices. *International Journal of Antennas and Propagation*, 2018, 2018.

[135] 100 series emc probes, 2020. Available from: https://www.beehive-electronics.com/datasheets/100SeriesDatasheetCurrent.pdf.

[136] Marlin firmware, 2020. Available from: https://marlinfw.org/.

[137] Dukju Ahn and Songcheol Hong. A study on magnetic field repeater in wireless power transfer. *IEEE Transactions on Industrial Electronics*, 60(1):360–371, 2012.

[138] X. Shi and J. R. Smith. Reconfigurable and adaptive coupled relay resonator platform for a moving receiver. In *2019 International Workshop on Antenna Technology (iWAT)*, pages 182–185, 2019.

[139] J. T. Boys, G. A. Covic, and A. W. Green. Stability and control of inductively coupled power transfer systems. *IEE Proceedings - Electric Power Applications*, 147(1):37–43, 2000.

[140] Byungcho Choi, Jaehyun Nho, Honnyong Cha, Taeyoung Ahn, and Seungwon Choi. Design and implementation of low-profile contactless battery charger using planar printed circuit board windings as energy transfer device. *IEEE Transactions on Industrial Electronics*, 51(1):140–147, 2004.

[141] M. Eghtesadi. Inductive power transfer to an electric vehicle-analytical model. In *40th IEEE Conference on Vehicular Technology*, pages 100–104, 1990.

[142] D. van Wageningen and T. Staring. The qi wireless power standard. In *Proceedings of 14th International Power Electronics and Motion Control Conference EPE-PEMC 2010*, pages S15–25–S15–32, 2010.

[143] Andre Kurs, Aristeidis Karalis, Robert Moffatt, John D Joannopoulos, Peter Fisher, and Marin Soljačić. Wireless power transfer via strongly coupled magnetic resonances. *science*, 317(5834):83–86, 2007.

[144] Aristeidis Karalis, John D Joannopoulos, and Marin Soljačić. Efficient wireless non-radiative mid-range energy transfer. *Annals of physics*, 323(1):34–48, 2008.

[145] Alanson P Sample, David T Meyer, and Joshua R Smith. Analysis, experimental results, and range adaptation of magnetically coupled resonators for wireless power transfer. *IEEE Transactions on industrial electronics*, 58(2):544–554, 2010.

[146] SD Delichte, YJ Lu, and JS Bobowski. Non-radiative mid-range wireless power transfer: An experiment for senior physics undergraduates. *American Journal of Physics*, 86(8):623–632, 2018.

[147] Benjamin L Cannon, James F Hoburg, Daniel D Stancil, and Seth Copen Goldstein. Magnetic resonant coupling as a potential means for wireless power transfer to multiple small receivers. *IEEE transactions on power electronics*, 24(7):1819–1825, 2009.

[148] Sid Assawaworrarit, Xiaofang Yu, and Shanhui Fan. Robust wireless power transfer using a nonlinear parity–time-symmetric circuit. *Nature*, 546(7658):387–390, 2017.

[149] Y. D. Ko and Y. J. Jang. The optimal system design of the online electric vehicle utilizing wireless power transmission technology. *IEEE Transactions on Intelligent Transportation Systems*, 14(3):1255–1265, 2013.

[150] David A Borton, Ming Yin, Juan Aceros, and Arto Nurmikko. An implantable wireless neural interface for recording cortical circuit dynamics in moving primates. *Journal of Neural Engineering*, 10(2):026010, feb 2013.

[151] T. M. Hayslett, T. Orekan, and P. Zhang. Underwater wireless power transfer for ocean system applications. In *OCEANS 2016 MTS/IEEE Monterey*, pages 1–6, 2016.

[152] Chunhua Liu, K. T. Chau, Zhen Zhang, Chun Qiu, Fei Lin, and T. W. Ching. Multiple-receptor wireless power transfer for magnetic sensors charging on mars via magnetic resonant coupling. *Journal of Applied Physics*, 117(17):17A743, 2015.

[153] Reem Shadid and Sima Noghanian. A literature survey on wireless power transfer for biomedical devices. *International Journal of Antennas and Propagation*, 2018, 2018.

[154] Fei Zhang, Steven A Hackworth, Weinong Fu, Chengliu Li, Zhihong Mao, and Mingui Sun. Relay effect of wireless power transfer using strongly coupled magnetic resonances. *IEEE Transactions on Magnetics*, 47(5):1478–1481, 2011.

[155] Dukju Ahn and Songcheol Hong. A study on magnetic field repeater in wireless power transfer. *IEEE Transactions on Industrial Electronics*, 60(1):360–371, 2012.

[156] Xiu Zhang, SL Ho, and WN Fu. Quantitative design and analysis of relay resonators in wireless power transfer system. *IEEE transactions on magnetics*, 48(11):4026–4029, 2012.

[157] Bin Luo, Shichuang Wu, and Nanrun Zhou. Flexible design method for multi-repeater wireless power transfer system based on coupled resonator bandpass filter model. *IEEE Transactions on Circuits and Systems I: Regular Papers*, 61(11):3288–3297, 2014.

[158] Benjamin H Waters, Brody J Mahoney, Gunbok Lee, and Joshua R Smith. Optimal coil size ratios for wireless power transfer applications. In *2014 IEEE international symposium on circuits and systems (ISCAS)*, pages 2045–2048. IEEE, 2014.

[159] Edward Bennett Rosa and Frederick Warren Grover. *Formulas and tables for the calculation of mutual and self-inductance*, volume 8, chapter 5, page 110. US Government Printing Office, 1948.

[160] JA Ferreira. Appropriate modelling of conductive losses in the design of magnetic components. In *21st Annual IEEE Conference on Power Electronics Specialists*, pages 780–785. IEEE, 1990.

[161] Shu Yuen Ron Hui, Wenxing Zhong, and Chi Kwan Lee. A critical review of recent progress in mid-range wireless power transfer. *IEEE Transactions on Power Electronics*, 29(9):4500–4511, 2013.

[162] Konstantinos A Polyzos, Athanasios A Konstantelias, and Matthew E. Falagas. Risk factors for cardiac implantable electronic device infection: a systematic review and meta-analysis. *Europace : European pacing, arrhythmias, and cardiac electrophysiology : journal of the working groups on cardiac pacing, arrhythmias, and cardiac cellular electrophysiology of the European Society of Cardiology*, 17 5:767–77, 2015.

[163] Jangwoen Lee, Naglaa El-Abaddi, A. Duke, A. Cerussi, M. Brenner, and B. Tromberg. Noninvasive in vivo monitoring of methemoglobin formation and reduction with broadband diffuse optical spectroscopy. *Journal of applied physiology*, 100 2:615–22, 2006.

[164] B. Tromberg, Z. Zhang, A. Leproux, T. O'Sullivan, A. Cerussi, P. Carpenter, R. Mehta, D. Roblyer, W. Yang, K. Paulsen, B. Pogue, Shudong Jiang, P. Kaufman, A. Yodh, S. Chung, M. Schnall, B. S. Snyder, N. Hylton, D. Boas, S. Carp, S. Isakoff, and D. Mankoff. Predicting responses to neoadjuvant chemotherapy in breast cancer: Acrin 6691 trial of diffuse optical spectroscopic imaging. *Cancer research*, 76 20:5933–5944, 2016.

[165] D. Busch, R. Choe, T. Durduran, and A. Yodh. Towards non-invasive characterization of breast cancer and cancer metabolism with diffuse optics. *PET clinics*, 8 3, 2013.

[166] S. Ueda, D. Roblyer, A. Cerussi, Amanda Durkin, A. Leproux, Ylenia Santoro, Shanshan Xu, T. O'Sullivan, D. Hsiang, R. Mehta, J. Butler, and B. Tromberg. Baseline tumor oxygen saturation correlates with a pathologic complete response in breast cancer patients undergoing neoadjuvant chemotherapy. *Cancer research*, 72 17:4318–28, 2012.

[167] T. O'Sullivan, A. Leproux, J. Chen, S. Bahri, Alex Matlock, D. Roblyer, C. McLaren, Wen-Pin Chen, A. Cerussi, M. Su, and B. Tromberg. Optical imaging correlates with magnetic resonance imaging breast density and reveals composition changes during neoadjuvant chemotherapy. *Breast Cancer Research : BCR*, 15:R14 – R14, 2012.

[168] T. O'Sullivan, A. Cerussi, D. Cuccia, and B. Tromberg. Diffuse optical imaging using spatially and temporally modulated light. *Journal of biomedical optics*, 17 7:071311, 2012.

[169] S. Chung, A. Cerussi, C. Klifa, H. Baek, O. Birgul, G. Gulsen, S. Merritt, D. Hsiang, and B. Tromberg. In vivo water state measurements in breast cancer using broadband diffuse optical spectroscopy. *Physics in medicine and biology*, 53 23:6713–27, 2008.

[170] S. Chung, A. Cerussi, S. Merritt, J. Ruth, and B. Tromberg. Non-invasive tissue temperature measurements based on quantitative diffuse optical spectroscopy (dos) of water. *Physics in medicine and biology*, 55 13:3753–65, 2010.

[171] S. Chung, R. Mehta, B. Tromberg, and A. Yodh. Non-invasive measurement of deep tissue temperature changes caused by apoptosis during breast cancer neoadjuvant chemotherapy: A case study. *Journal of innovative optical health sciences*, 4 4:361–372, 2011.

[172] R. Nachabe, B. Hendriks, A. Desjardins, M. van der Voort, M. B. van der Mark, and H. Sterenborg. Estimation of lipid and water concentrations in scattering media with diffuse optical spectroscopy from 900 to 1,600 nm. *Journal of biomedical optics*, 15 3:037015, 2010.

[173] L. Kocsis, P. Herman, and A. Eke. The modified beer-lambert law revisited. *Physics in medicine and biology*, 51 5:N91–8, 2006.

[174] Gradishar WJ;Moran MS;Abraham J;Aft R;Agnese D;Allison KH;Anderson B;Burstein HJ;Chew H;Dang C;Elias AD;Giordano SH;Goetz MP;Goldstein LJ;Hurvitz SA;Isakoff SJ;Jankowitz RC;Javid SH;Krishnamurthy J;Leitch M;Lyons J;Mortimer J;Patel SA;Pierce LJ;Rosenberge. Breast cancer, version 3.2022, nccn clinical practice guidelines in oncology.

[175] Benjamin H. Waters, Brody J. Mahoney, Gunbok Lee, and Joshua R. Smith. Optimal coil size ratios for wireless power transfer applications. *2014 IEEE International Symposium on Circuits and Systems (ISCAS)*, pages 2045–2048, 2014.

[176] Y. Wang, D. Ye, Liangjian Lyu, Yingfei Xiang, Hao Min, and C. R. Shi. A 13.56mhz wireless power and data transfer receiver achieving 75.4% effective-power-conversion efficiency with 0.1% ask modulation depth and 9.2mw output power. *2018 IEEE International Solid - State Circuits Conference - (ISSCC)*, pages 142–144, 2018.

[177] Martino Grandolfo. Worldwide standards on exposure to electromagnetic fields: an overview. *The Environmentalist*, 29:109–117, 2009.

[178] Zhigang Tang, Brian Smith, John H. Schild, and P. Hunter Peckham. Data transmission from an implantable biotelemeter by load-shift keying using circuit configuration modulator. *IEEE Transactions on Biomedical Engineering*, 42:524–528, 1995.